Design and Testing of a Bubble Generator for Molten Salt Surrogate Fluid

Courts Breeden

Thesis submitted to the faculty of the Virginia Polytechnic Institute and State University in partial fulfillment of the requirements for the degree of

Master of Science
in
Nuclear Engineering

Yang Liu (Chair)
Alireza Haghighat
David Freeman

October 9, 2024

Arlington, Virginia

Keywords: bubble, molten salt, surrogate fluid

Design and Testing of a Bubble Generator for Molten Salt Surrogate Fluid

Courts Breeden

ABSTRACT

This study explores the design, testing, and modeling of a bubble injector intended for use in studying bubble dynamics in molten salt reactors using a room temperature surrogate fluid by matching the Reynolds number, Eötvös number, and Morton number defined by the properties of the helium bubbles in the pump bowl of the Molten Salt Reactor Experiment (MSRE). The injector, constructed from polydimethylsiloxane (PDMS) and acrylic, was tested to generate bubbles within a precise size range suitable for simulating conditions in molten salt reactors. Experimental data showed that the equivalent bubble diameter is directly proportional to gas flow rate and inversely proportional to liquid flow rate, with clear trends emerging when data were subdivided into constant flow rate plots. The study applied and adapted the bubble size control model proposed by Lu et al. (2014), revealing limitations in existing models under modified conditions such as an elongated two-phase channel. A novel model was developed to better predict bubble size, incorporating dependencies on both flow rate ratios and the capillary number of the microchannels. The injector's design facilitates convenient modifications in channel geometry to achieve target bubble sizes, and future improvements in pressure monitoring and imaging are recommended. This work contributes to the advancement of microfluidic bubble injection technology.

Design and Testing of a Bubble Generator for Molten Salt Surrogate Fluid

Courts Breeden

GENERAL AUDIENCE ABSTRACT

This study focuses on developing and testing a device that creates tiny bubbles to help us better understand bubble behavior in advanced nuclear reactors, specifically molten salt reactors. These reactors use a special type of liquid fuel, and understanding how bubbles move within them is important for improving their efficiency and safety. To simulate the conditions inside these reactors without using the actual molten salt, we used a substitute fluid that has similar properties to the molten salt and built a bubble injector made from clear, flexible materials.

Our experiments showed that the size of the bubbles depends on the flow rates of the gas and liquid: larger bubbles are formed when more gas is injected, and smaller bubbles are created when the liquid flow is increased. We tested existing models that predict bubble size and found that they didn't always work well under the conditions we used, like longer channels where the gas and liquid mix. As a result, we developed a new model that better predicts bubble size by considering both flow rates and the Capillary number of the microchannels.

The design of our injector allows for easy adjustments to make bubbles of different sizes, and we suggest future improvements in pressure measurement and camera equipment to enhance data accuracy.

Dedication

To my parents,

Lori and Lucius Breeden

Acknowledgments

I would like to thank my advisor, Dr. Yang Liu, for the guidance and encouragement he has shown me in my graduate school experience. I have been intellectually enriched by him challenging me to be the best researcher I can be.

I would also like to thank the other students from my lab: Multi-phase Flow and Thermal-hydraulics Lab (MFTL) for their advice and input. In addition, I would like to thank the students from other laboratories who helped me with fabrication. In particular, I would like to thank Henry Claesson from Dr. Christopher Williams' lab as well as Wenge Huang and Mohammed Shamsodini Lori form Dr. Jiangtao Cheng's lab

Lastly, I would like to thank my family. I thank my brother, Gates Breeden for being a fantastic role model for me and for guiding my way to Virginia Tech. I thank my parents, Lori and Lucius Breeden for their continuous support and inspiration for me to have high aspirations and to become the best version of myself. Without them, I would have no passion for education and hence, I owe all success (especially academic) I have found or will find to them.

Table of Contents

Dedication iv
Acknowledgments v

List of Figures viii

List of Tables x

1. Introduction 1
1.1. The Need for Nuclear Power 1
1.2. The Utility of Nuclear Power 5
1.3. Molten Salt Reactors 9

2. Background 12
2.1. Surrogate Fluid 12
2.2. Analysis Background 19
2.3. Dimensionless analysis 25
2.4. Microfluidics 33

3. Injector Design 38
3.1. PDMS Chip Design and Fabrication 38
3.2. Acrylic Sandwich Design and Fabrication 46
3.3. Injection 57
3.4. Test Section Loop 60

4. Injector Testing 72
4.1. Outside Loop Experimental Setup and Procedure 72
4.2. Image Processing Outside Loop 76
4.3. Experimental Setup Inside Loop 88
4.4. Image Processing Inside Loop 93

5. Results and Discussion 109

5.1. Injector Test Results Outside The Test Loop 109

5.2. Injector Test Results Inside The Test Loop 117

5.3. Model Evaluation and Development 122

6. Conclusion and Future Work 134

6.1. Conclusion 134

6.2. Future Work 135

References 138

Appendix 141

A. Outside of The Loop Supplementary Material 141

B. Inside of The Loop Supplementary Material 148

List of Figures

Figure 1.1: Comparison of the power densities of various energy types (van Zalk 2018 and Behrens, 2018). 4
Figure 2.1: Graph showing fit of density model with experimental data 14
Figure 2.2: Graph showing fit of surface tension model with experimental data 15
Figure 2.3: Graph showing interpolated experimental surface tension data 16
Figure 2.4: Graph showing fit of the viscosity model with experimental data 18
Figure 2.5: Graph showing fit of the interpolated viscosity model with experimental data 19
Figure 2.6: Shape regimes of bubbles defined by Reynolds, Eötvös, and Morton numbers courtesy of (Clift et al., 1978) 24
Figure 2.7: Region of acceptable dimensionless numbers on shape regime graph courtesy of (Clift et al., 1978) 27
Figure 2.8: Plot to visualize the acceptable range of the Morton Number 29
Figure 2.9: Surface plot to visualize the acceptable range of the Reynolds Number 31
Figure 2.10: Surface plot to visualize the acceptable range of the Eötvös Number 32
Figure 2.11: Visualization of (A) T-junction structure. (B) Flow-focusing structure. (C) Coaxial focusing structure for microfluidic devices (Liu et al., 2022) 35
Figure 3.1:Visualization of the T-junction geometry 39
Figure 3.2: Final geometry of the PDMS chip 40
Figure 3.3: CAD model of the PDMS mold 41
Figure 3.4: 3D printed PDMS mold 42
Figure 3.5: PDMS mixture in vacuum chamber 43
Figure 3.6: PDMS mold and curing setup 45
Figure 3.7: Exploded view of acrylic-PDMS sandwich 47
Figure 3.8: Assembled acrylic-PDMS sandwich 48
Figure 3.9: CAD model with fittings 49
Figure 3.10: CAD model of injector for outside test loop testing 50
Figure 3.11: CAD model for injector flange 51
Figure 3.12: Unpolished flange 53
Figure 3.13: Polished flange 54
Figure 3.14: CAD model of the complete injector assembly 55
Figure 3.15: Exploded view of the complete injector assembly 56
Figure 3.16: Picture of complete injector assembly 57
Figure 3.17: NE-300 InfusionONE Syringe Pump 58
Figure 3.18: Injection setup 60
Figure 3.19: CAD model of the injector assembly fitting into the test section. 61
Figure 3.20: Test loop structure and tank 62
Figure 3.21: Circulation pump fastened to the tank structure 64
Figure 3.22: Flow directing device for flow meters 65
Figure 3.23: Flow meter used for tests inside loop 67
Figure 3.24: T-joint uniting flow from both flow meters 68
Figure 3.25: Drain for emptying the tank 69
Figure 3.26: Drain for emptying the test section 70
Figure 4.1: Test setup for outside loop tests 74

Figure 4.2: Example of raw image captured in outside loop testing 77
Figure 4.3: Cropped image of microfluidic region of interest 78
Figure 4.4: Inverted image of microfluidic region of interest 78
Figure 4.5: Saturated image of microfluidic region of interest 79
Figure 4.6: Mediad-filtered image of microfluidic region of interest 79
Figure 4.7: Binarized image of microfluidic region of interest 80
Figure 4.8: Final image used for calculations. 80
Figure 4.9: Second region of interest 81
Figure 4.10: Plot of pixel count within the second region of interest 82
Figure 4.11: Frequency domain graph of periodic data 83
Figure 4.12: Frequency domain graph of nonperiodic data 84
Figure 4.13: Close-up example of an individual bubble analyzed by the program 86
Figure 4.14: Picture of inside test loop experimental setup 91
Figure 4.15: Raw image of inside test loop bubbles 94
Figure 4.16: Calibration image for inside loop tests 95
Figure 4.17: Background image 96
Figure 4.18: Cropped image of inside test loop bubbles 97
Figure 4.19:Inverted image of inside test loop bubbles 98
Figure 4.20: Saturated image of inside test loop bubbles 99
Figure 4.21: Filtered image of inside test loop bubbles 100
Figure 4.22: Binarized image of inside test loop bubbles 101
Figure 4.23: Binarized image of inside test loop bubbles with the bubbles filled in 102
Figure 4.24: Binarized image of inside test loop bubbles with big and small bubbles removed 103
Figure 4.25: Final image used to calculate the size of the bubbles 104
Figure 4.26: Histogram showing distribution of bubble volume 106
Figure 4.27: Smoothed distribution of bubble diameter 107
Figure 4.28: Histogram of normalized bubble volume 108
Figure 5.1: Surface plot showing the relation between the injection rates and equivalent diameter 110
Figure 5.2: Grid plot displaying relationship between liquid flow rate and equivalent diameter 111
Figure 5.3: Grid plot displaying relationship between gas flow rate and equivalent diameter 112
Figure 5.4: Grid plot displaying relationship between liquid flow rate and Bubble generation frequency 114
Figure 5.5: Grid plot displaying relationship between gas flow rate and Bubble generation frequency .. 115
Figure 5.6: Flow regime map (Mishima and Ishii, 1984) 117
Figure 5.7: Histogram distribution of bubble diameter 118
Figure 5.8: Smoothed distribution of bubble diameter. 119
Figure 5.9: Surface plot showing the bubble diameter data from the inside loop tests 121
Figure 5.10: Diagonal plot comparing the predictions of Lu et al. (2014) model with experimental data. 123
Figure 5.11: Diagonal plot showing the fit of the corrected Lu et al. (2014) model with the data 125
Figure 5.12: Diagonal plot showing the fit of predicted pressure drop to observed pressure drop 126
Figure 5.13: Diagonal plot showing the goodness of fit of the developed model 128
Figure 5.14: Grid plot showing the model's response accuracy to liquid flow rate fluctuations 129
Figure 5.15: Grid plot showing the model's response accuracy to gas flow rate fluctuations 130
Figure 5.16: Surface plot showing the shape of the model 131
Figure 5.17: Diagonal plot showing the fit of the model with the data from the inside test loop tests 132

List of Tables

Table 1.1: Summary of Total Costs for Producing 469 bkWhrs from New Builds over the next 60 years (Conca and Wright, 2010) 7
Table 1.2: Mortality rates of each energy source (Brook et al., 2015) 8
Table 2.1 Summary of relations to calculate properties of FLiBe as a function of temperature. 13
Table 2.2 Summary of relevant dimensionless numbers. 20
Table 2.3: Appropriate values of constants a and b 23
Table 2.4: Target values of dimensionless numbers 26
Table 4.1: Injection volumetric flow rates 75
Table 4.2: Injection flow rates 92
Table 5.1: Flow condition naming convention 120
Table A.1:Outside of the loop condition naming convention 142
Table A.2: Outside of the loop measured gauge pressure (psig) 144
Table A.3: Outside of the loop measured bubble generation frequency (Hz) 145
Table A.4: Outside of the loop measured bubble equivalent diameter (mm) 146
Table A.5: Outside of the loop measured average slug velocity (m/s) 147
Table A.6: Outside of the loop mass correction factor 148
Table B.1: Inside of the loop condition naming convention 150
Table B.2: Inside of the loop measured gauge pressure (psig) 151
Table B.3: Inside of the loop measured equivalent diameter (mm) 151

Chapter 1

1. Introduction

1.1. The Need for Nuclear Power

The demand for clean energy grows every year. As the world becomes more developed, those benefiting from this progress are increasingly concerned about its environmental impact. Rising energy demands are closely linked to the side effects of energy production, especially the burning of fossil fuels. This process has come under intense scrutiny due to the byproducts released into the environment, particularly carbon dioxide. Many argue that the release of carbon dioxide into the atmosphere will have irreversible detrimental effects on the global climate. Consequently, a popular movement for carbon neutrality has emerged.

Carbon neutrality aims to balance the amount of carbon dioxide released into the atmosphere with an equivalent amount sequestered or offset, ultimately achieving net-zero carbon emissions. To reduce carbon emissions, alternatives to fossil fuels have emerged that release no carbon into the environment, known as clean energy sources. The most notable clean energy sources are wind, solar, and nuclear power.

Wind energy is produced by converting the kinetic energy of wind into electrical energy. As the wind blows, it turns the blades of turbines, which spin a generator to produce electricity. Solar energy is produced by converting sunlight directly into electricity through the photovoltaic

effect. These methods have become vastly more efficient over the years, but they cannot be relied upon as the sole sources of energy to meet the needs of modern society.

An important concept in evaluating the viability of a power source is its capacity factor. The capacity factor compares the actual power output of the power source to its maximum possible output. It is calculated by dividing the actual power output by its maximum possible output over a period of time. This measure indicates the percentage of time that a power source is producing power (Tyra et al., 2020). For example, the capacity factor of a solar farm is greatly affected by how sunny it is on a particular day and the fact that the sun does not shine for the entirety of the day. Solar farms do not provide any power at night, resulting in an average capacity factor of 24.5% (Tyra et al., 2020). Similarly, wind power's average capacity factor, 34.6% (Tyra et al., 2020), depends heavily on how often the wind blows. There are times when the sun isn't shining, and the wind isn't blowing, leading to potential power outages if society relies solely on these sources. There is also a significant amount of variation in the power producing potential of solar and wind with the time of year e.g. the sun doesn’t shine as brightly or for as long in the winter as in the summer. It is worth noting that there are energy storage methods to make these systems more resilient to such an occurrence. For example, the energy can be stored in a battery which can be loaded at night when there is no power output of the solar farms. The utility of any of these energy storage devices will result in energy losses because of the conversion of one form of energy to another (Brook et al., 2015).

Power density is another very important concept to take into consideration when studying the viability of a power source. It is defined as the amount of power that the source is producing per unit area of land that it occupies. The common unit for this is W/m^2. As land is one of

humanity's most precious resources, minimizing the amount of land required to meet our energy demands is of utmost importance. In a 2018 meta-analysis, van Zalk and Behrens (2018) compared the power densities of various power sources taking into consideration the infrastructure requirement ratio (additional land needed for the power source i.e. mines), efficiency (the ratio of the energy input to the energy output), and capacity factor. The results of the study are summarized in Figure 1.1.

The figure depicts box plots of the power densities on a log scale. The annotation "n" represents the number of values studied of power density, and "mdn" represents the median value found. The green boxes show the data of the energy types the paper defines as "renewable energy types", and the blue boxes show the data of the energy types the paper defines as "non-renewable".

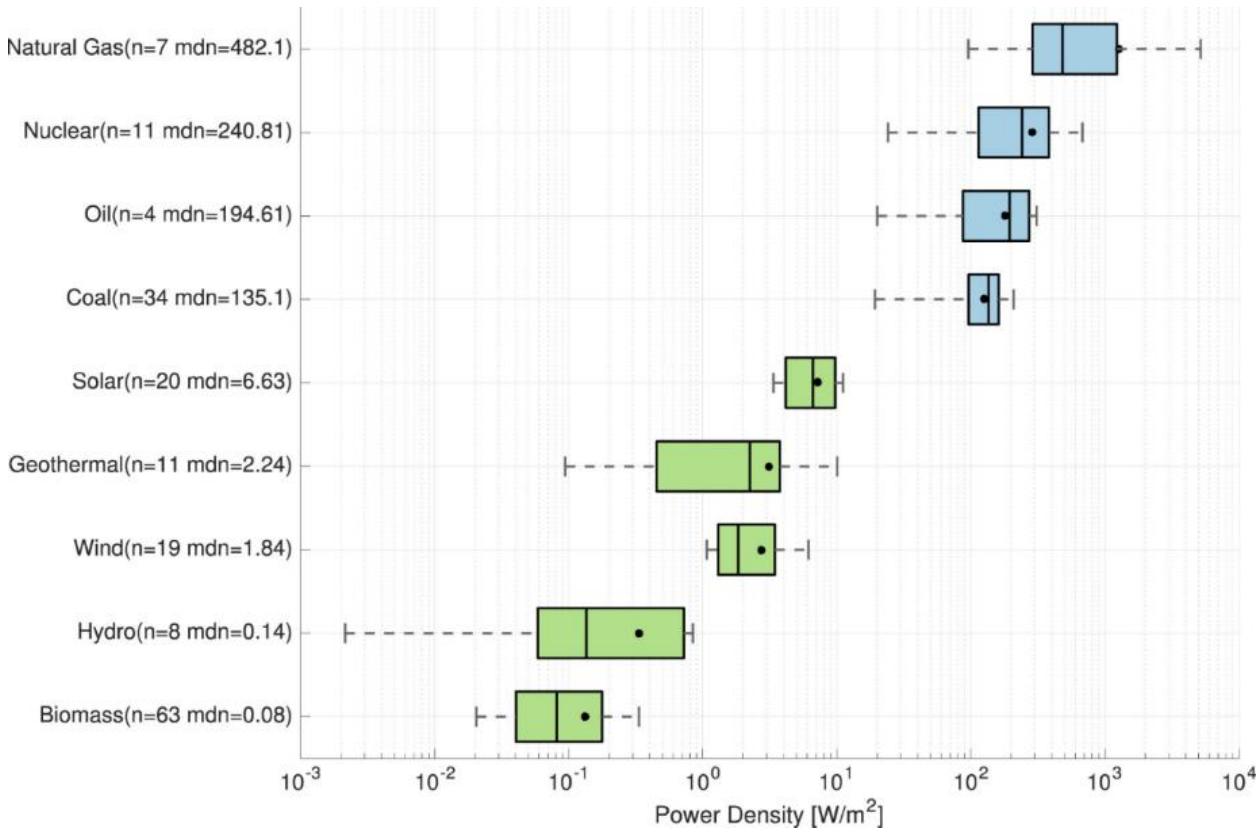

Figure 1.1: Comparison of the power densities of various energy types (van Zalk 2018 and Behrens, 2018).

It is clear to see the drawbacks of the energy types presented in the green boxes. Even though van Zalk and Behrens do not include nuclear power in the list of renewable energy types, this is not a widely accepted fact. A more in-depth discussion of the renewability of nuclear power can be found in Section 1.2. As shown in Figure 1.1, the median nuclear power plant outperforms the median solar farm by a factor of over 36 and the median wind farm by over 2 orders of magnitude as presented in the paper. It is also worth noting that the paper shows that nuclear power is comparable in performance to the fossil fuels that must be largely phased out to achieve

carbon neutrality (Tyra et al., 2020). This indicates that the energy sources labeled in that paper as “renewable” are very difficult to scale to the magnitude of the world’s current and future energy needs and that nuclear power plants are a much better option to replace fossil fuels.

1.2. The Utility of Nuclear Power

The evidence presented thus far indicates that nuclear power is the clear solution to the problems that the world faces with respect to carbon emissions and energy needs. It is fitting to now discuss the reasons nuclear power is not more abundantly utilized in modern society. Common cited reservations from the public about nuclear are as follows: the emissions, the waste, the economic viability, the safety, and the sustainability (Brook et al., 2015).

Nuclear power plants do not emit carbon or other harmful chemicals into the atmosphere during normal operation. Emissions only occur when emergency diesel generators are utilized, which is rare enough that their impact is negligible. This is not the case for intermittent renewable energy sources like solar and wind. Backup power for these sources is often provided by burning fossil fuels to supply power to the grid when the sun isn’t shining, and the wind isn’t blowing sufficiently to meet demand. An example of a flourishing use of nuclear power is France. In France, where approximately 75% of the electricity market is powered by nuclear fission, its per capita greenhouse gas emissions are among the lowest of all industrialized nations. These emissions are significantly lower compared to similar countries that do not use nuclear power and instead depend on a combination of fossil fuels and renewable energy sources (Brook et al., 2015). However, the reservations people have with nuclear energy with respect to

its environmental impact are not carbon emissions.

As of the end of 2019, 84,445 metric tons of spent fuel from commercial reactors were stored in 79 different locations 65 of which were operating reactor sites in 35 states (Carter, 2020). This increasing buildup of waste concerns people especially because of its radioactive nature. The current setup for disposal of nuclear waste works for the time being as it is mostly isolated to active reactor sites with much attention. However, as the volume of the waste continues to increase, this solution isn't permanent. A potential solution to this problem as outlined in Section 1.3, is the use of advanced fuel cycles. With reprocessing and fast neutron reactors, it is possible to reduce the volume of nuclear waste, as well as significantly reduce the need for long term repositories (Zohuri et al., 2023).

As mentioned earlier, 75% of France's electricity market is powered by nuclear fission. France's unit price of electricity is also among the lowest worldwide (Brook et al. 2015). Since France has put so much faith in nuclear power, they have figured out how to effectively utilize it so that it is economically viable. In a paper analyzing the viability of different energy sources, Conca and Wright (2010) found the cost per kilowatt-hour of every major energy source taking into consideration the construction, fuel, operation and maintenance (O&M), and decommissioning. The results are summarized in Table 1.1

Table 1.1: Summary of Total Costs for Producing 469 bkWhrs from New Builds over the next 60 years (Conca and Wright, 2010)

Source/Cost ($billions)	*Construction*	*Fuel*	*O&M*	*Decomm*	*Total*	*normalized*	*w/$15/ton$CO_2$ emitted carbon tax*
Coal	6.2	9.4	2.8	0.98	19.4	4.1 ¢/kWhr	5.6 ¢/kWhr
Natural Gas	3.2	18.8	2.3	0.01	24.3	5.2 ¢/kWhr	6.1 ¢/kWhr
Nuclear	7.0	2.8	6.1	0.52	16.4	3.5 ¢/kWhr	3.5 ¢/kWhr
Wind	15.0	0	4.7	0.61	20.3	4.3 ¢/kWhr	4.3 ¢/kWhr
Solar	35.1	0	0.5	0.37	36.0	7.7 ¢/kWhr	7.8 ¢/kWhr
Hydro	7.5	0	3.8	4.03	15.3	3.3 ¢/kWhr	3.5 ¢/kWhr

The last column of Table 1.1 shows the application of the carbon emission tax. This is a tax that charges $15 per ton of CO_2 emitted into the atmosphere. It is used to incentivize cleaner energy (Brook et al., 2015). A great economic strength of nuclear is that it is resilient to fluctuations in fuel prices. A 50% increase in fuel price in nuclear would result in a 3% increase in per unit energy output compared to a 20% to 40% increase as observed in fossil fuel energy production (IEA, 2006).

Perhaps the largest reservation the public has with nuclear power stems from the three commercial power plant accidents that have occurred: Three Mile Island (TMI) in 1979, Chernobyl in 1986, and Fukushima Daiichi in 2011. These accidents are often exaggerated in the public's mind. The public's perception of them is that each had many more fatalities and adverse health effects than the actual numbers indicate. The accident at TMI was contained well and there was no land contamination. There was also an evacuation put in place as a cautionary measure (Brook et al. 2015). However, it is worth noting the effects of the Chernobyl and Fukushima

accidents. In Conca's paper, there is also a comparison of the mortality rates per billion kilowatt-hours produced by major energy sources as shown in Table 1.2 which takes into consideration Chernobyl and Fukushima. From the table, it is clear to see that nuclear power is the safest energy source available.

Table 1.2: Mortality rates of each energy source (Brook et al., 2015)

Energy Source	Mortality Rate (deaths per billion kWh)	
Coal – global average	161	(50% of global electricity)
Coal – China	278	(75% of China's electricity)
Coal – U.S.	15	(44% of U.S. electricity)
Oil	36	(36% of global energy, 8% of global electricity, none in the U.S.)
Natural Gas	4	(20% of global electricity)
Biofuel/Biomass	24	(21% of global energy)
Solar (rooftop)	0.44	(< 1% of global electricity)
Wind	0.15	(~ 1% of global electricity)
Hydro – global average	1.4	(15% of global electricity, 171,000 Banqiao dead)
Nuclear – global average	0.04	(17% of global electricity w/Chernobyl&Fukushima - none in the U.S.)

Lund claims "sustainable energy can be defined as energy sources that are not expected to be depleted in a time frame relevant to the human race; therefore, they contribute to the sustainability of all species." Following this definition, he claims that nuclear power does not fit under this definition because of its reliance on uranium which he claims to be "a scarce resource within the relevant time frame" (Lund, 2014). As mentioned earlier, this claim is not widely accepted. Alonso et al. (2015) argue for the renewability of nuclear power stating that the

available uranium deposits, combined with the use of fast fission reactors, make nuclear power an “inexhaustible energy source.” Alonso et al. further explain that there is an abundance of depleted uranium that is stored at enrichment plants and used fuel elements. With the use of fast fission reactors, they claim the energy recoverable from this uranium can power the world for several hundred years (Alonso et al., 2015).

1.3. Molten Salt Reactors

The fast fission reactors referenced in Alonso’s paper are a type of breeder reactor. Breeder reactors produce more fissile material than they consume. Fissile material refers to nuclides that can undergo fission and produce power when interacting with a neutron. Breeder reactors achieve this by bombarding fertile nuclides with neutrons. Fertile nuclides are isotopes that can be converted into fissile nuclides, which can then split and release thermal energy. There are two main types of breeder reactors: fast breeder reactors and thermal breeder reactors.

Fast breeder reactors use fast neutrons to breed fissile plutonium-239. Fast neutrons, which have high energy, are less likely to interact with nuclei. However, they are more likely to be captured by fertile uranium-238 than by fissile uranium-235. When a neutron is captured by uranium-238, the nuclide becomes uranium-239, which is unstable and undergoes beta minus decay to become neptunium-239, which also undergoes beta minus decay to become plutonium-239, a stable fissile nuclide. Beta minus decay is a process where a neutron within a nucleus is converted into a proton, releasing an electron and increasing the nucleus's atomic number by one. Fast reactors are particularly useful because uranium-238, which has a natural abundance of

99.27%, is far more common than uranium-235, which has an abundance of 0.711%. Conventional nuclear reactors use uranium-235, which must be refined to around 5% to be useful. Utilizing uranium-238 to produce energy makes nuclear power an inexhaustible energy source by recycling spent fuel and extracting more energy from mined uranium. Fast molten salt reactors are among the most popular types of fast breeder reactors.

Thermal breeder reactors, on the other hand, breed fissile uranium-233 using thermal neutrons. Thermal neutrons, which have low energy, are more likely to interact with nuclei. Nuclear reactors rely on these thermal neutrons to fission uranium-235. Since the neutrons produced by nuclear fission are fast neutrons, thermal reactors need to thermalize these neutrons with a moderator. Moderators are materials with high scattering cross sections, meaning they are likely to scatter neutrons and reduce their energy. Lower energy neutrons have a higher probability of interacting with fissile nuclei, causing fission and releasing thermal energy. Thermal breeder reactors use fertile thorium-232 to produce fissile uranium-233 similarly to how fast breeder reactors use fertile uranium-238 to produce fissile plutonium-239. Thorium-232 has a high thermal absorption cross section, making it likely to capture neutrons and transform into thorium-233, which is unstable and undergoes beta minus decay to become protactinium-233, which also undergoes beta minus decay to become fissile uranium-233. A notable type of thermal breeder reactor is the thermal molten salt reactor, as studied in the Oak Ridge National Laboratory (ORNL) Molten-Salt Reactor Experiment (MSRE).

Breeder reactors are crucial in advanced fuel cycles because they can utilize the surplus of spent fuel from conventional reactors. By recycling, the uranium from spent fuel can be used in breeder reactors to produce more fissile material, thereby utilizing more of the uranium for power

production, not just the rare uranium-235. Molten salt reactors are a viable option for breeder reactors due to their safety, efficiency, and continuous operation. These reactors can operate at very high temperatures (1200°F), increasing thermal efficiency, and at relatively low pressures (5 psig), reducing the risk of explosions. Molten salt serves as both the fuel and the coolant, eliminating the risk of hydrogen explosions that can occur in conventional reactors. Additionally, molten salt reactors use more of the fissile material and can be refueled online, allowing continuous operation and higher capacity factors.

To effectively commercialize molten salt breeder reactors on a large scale, it is essential to understand all processes necessary for their operation. One challenge unique to these reactors, due to the liquid form of the fuel, is the removal of poisonous fission products. Neutron poisons are nuclides with large absorption cross-sections, leading to neutron absorption and reduced neutron economy. When a fissile nucleus undergoes fission, it produces fission products, such as xenon-135, a significant neutron poison due to its gaseous nature. Removing these gaseous fission products is crucial for the operation of a molten salt reactor. The MSRE removed these gases in a pump bowl, where the molten salt was vigorously sprayed into itself through a helium gas medium, entraining small helium bubbles. This process allowed the diffusion of gaseous fission products like xenon-135 into the helium, from which they could be separated. However, little research has been done on the properties of these bubbles, such as the diffusion rate of gaseous fission products and bubble movement. This paper focuses on developing a better understanding of bubble movement, as their behavior could affect reactor reactivity.

Chapter 2

2. Background

2.1. Surrogate Fluid

To accurately study the movement of helium bubbles, it is crucial to replicate the conditions in which they are found. These conditions can be characterized by dimensionless numbers, as discussed in Section 2.2. The aim of this study is to design and test a bubble injector that can be used in a system that mirrors the dimensionless numbers present in molten salt reactors. Instead of using molten salt to achieve this, this study uses a water-glycerin mixture as a surrogate fluid due to its properties at room temperature. Before conducting a dimensionless analysis, the properties of the molten salt reactor and the glycerin-water mixtures must be defined.

The MSRE used FLiBe as the salt, a mixture of lithium fluoride and beryllium fluoride. Extensive data on FLiBe's properties is available from the tests conducted by ORNL during the five years of the MSRE's operation. These properties are detailed in Table 2.1 from relations defined by Compre et al. (1975) as a function of temperature. Additionally, understanding the size of the bubbles present is essential; this is specified as 0.4 mm in the same paper (Compre et al., 1975). The helium densities used in this study are provided in tables from (Peterson 1970).

Table 2.1 Summary of relations to calculate properties of FLiBe as a function of temperature.

Property	**Relation with temperature T (ºC)**
Density (kg/m^3)	$\rho = 1000(2.575 - 5.13 * 10^{-4} * T)$
Viscosity (Pa-s)	$\mu = 1.16 * 10^{-4} \exp\left(\frac{3755}{T + 273.15}\right)$
Surface Tension (kg/s^2)	$\sigma = \frac{260 - .12T}{1000}$

The properties of the substances used in the experimental setup for this study must be clearly defined. Tamakura et al. (2012) define the properties for glycerin-water mixtures at room temperature as a function of weight percent.

In this paper, the density of a glycerin-water mixture, ρ_{mix}, is defined with

$$\rho_{mix} = w_w \rho_w + w_{gl} \rho_{gl}, \tag{1}$$

where $w_w$is the weight ratio of water, w_{gl} is the weight ratio of glycerin, ρ_w is the density of pure water, and $\rho_{gl}$is the density of pure glycerin. Additionally, it is established that:

$$w_w + w_{gl} = 1, \tag{2}$$

since the mixture only contains glycerin and water. These equations can be rearranged to form:

$$\rho_{mix} = (1 - w_{gl})\rho_w + w_{gl} \rho_{gl}, \tag{3}$$

which is advantageous as it simplifies the dependency for density to a single variable. As shown in Figure 2.1, this model aligns well with the experimental data found by Tamakura et al. (2012) at room temperature.

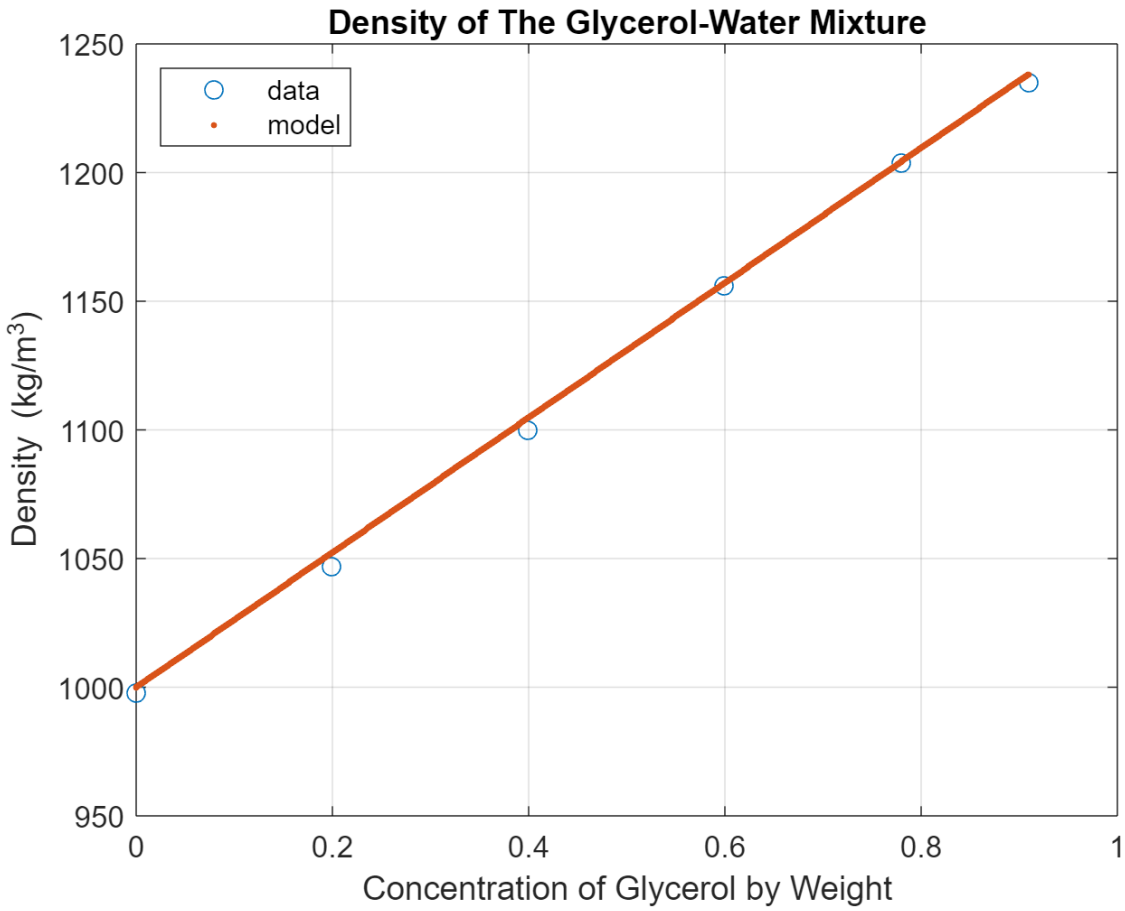

Figure 2.1: Graph showing fit of density model with experimental data

Next, it is necessary to define the surface tension as a function of weight ratio of glycerin. (Takamura et al., 2012) gives the following relation:

$$\sigma_{mix} = w_w \sigma_w + w_{gl} \sigma_{gl}, \tag{4}$$

where σ_w represents the surface tension of pure water, and σ_{gl} represents the surface tension of pure glycerin. Like Equation (3), this can be modified to

$$\sigma_{mix} = (1 - w_{gl})\sigma_w + w_{gl}\sigma_{gl}, \tag{5}$$

resulting in an equation with only one dependency. However, as shown in Figure 2.2, this model fits the data from Tamakura et al. (2012) poorly.

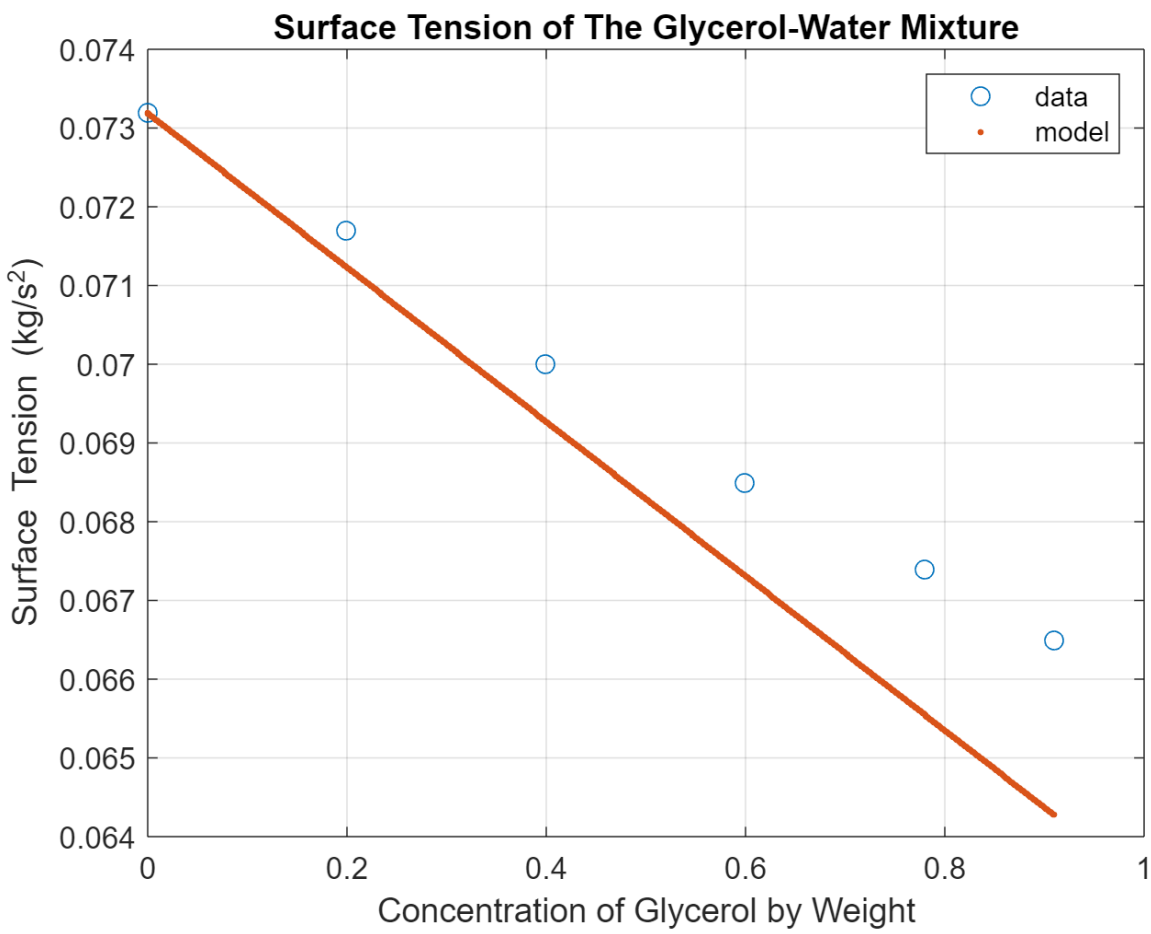

Figure 2.2: Graph showing fit of surface tension model with experimental data

The method used to define the surface tension as it varies with the weight ratio of glycerin in the mixture is interpolation. Conceptually, this involves drawing lines on a graph between each experimental data point and determining the property at each value in the domain based on the

quantities that fall along those lines. Figure 2.3 illustrates the result of interpolating the surface tension data.

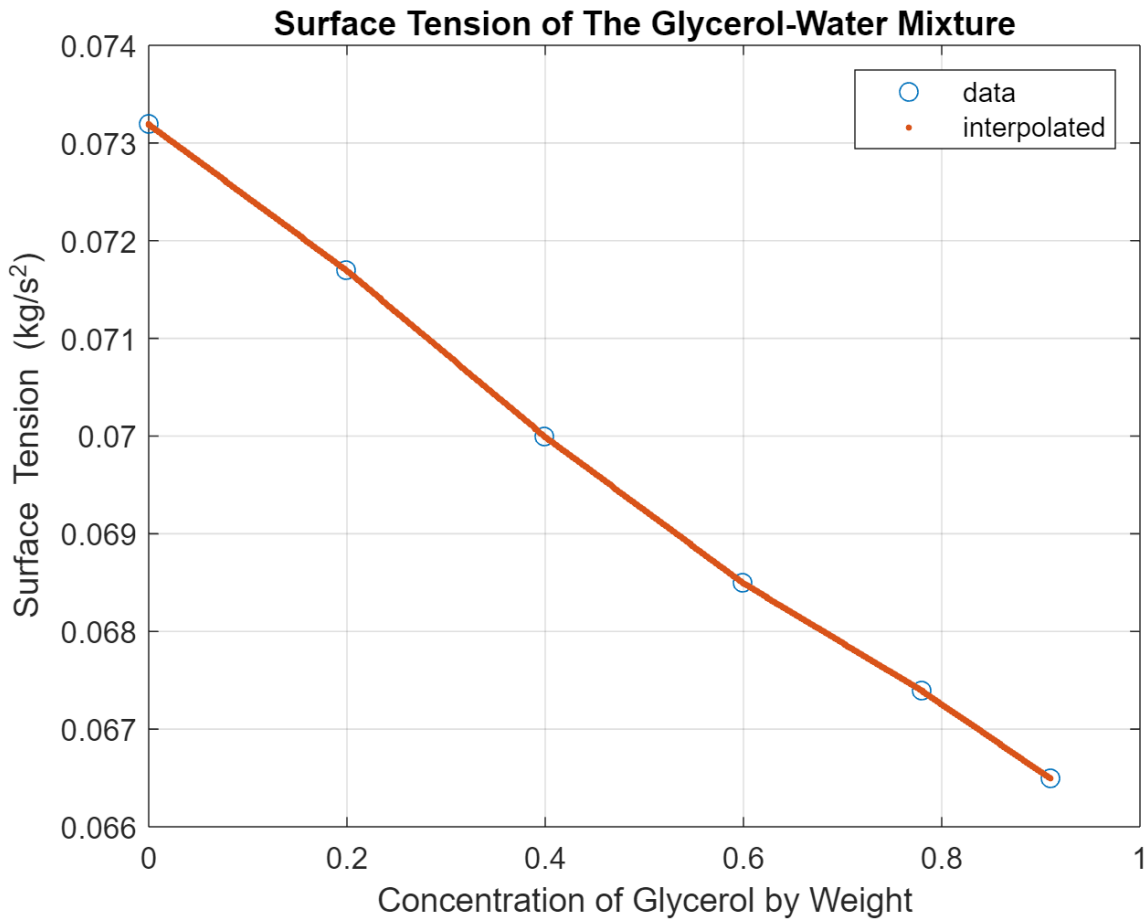

Figure 2.3: Graph showing interpolated experimental surface tension data

The final property of glycerin-water mixtures that needs to be modeled for this study is viscosity. The relationship between the weight ratio and viscosity is highly nonlinear, requiring a more complex model. The model for the viscosity of the mixture, μ_{mix} proposed by Takamura is as follows:

$$\mu_{mix} = \mu_w \left(\frac{1 - \frac{C}{C_m}}{1 - \frac{(k_0 C_m - 1)C}{C_m}} \right), \tag{6}$$

where μ_w represents the viscosity of pure water, C represents the volume ratio of the glycerin-water mixture, and k_0 and C_m are constants that vary with temperature to fit the data accurately. In this study, the values for k_0 and C_m that best fit the experimental data are 1.007 and 1.006, respectively. To apply this model, the volume ratio must be related to the weight ratio. To convert the weight ratio into the volume ratio, the relation

$$C = \frac{w_{gl}/\rho_{gl}}{w_{gl}/\rho_{gl} + (1 - w_{gl})/\rho_w}, \tag{7}$$

is used. The accuracy of the model can be visualized in Figure 2.4 on a log plot.

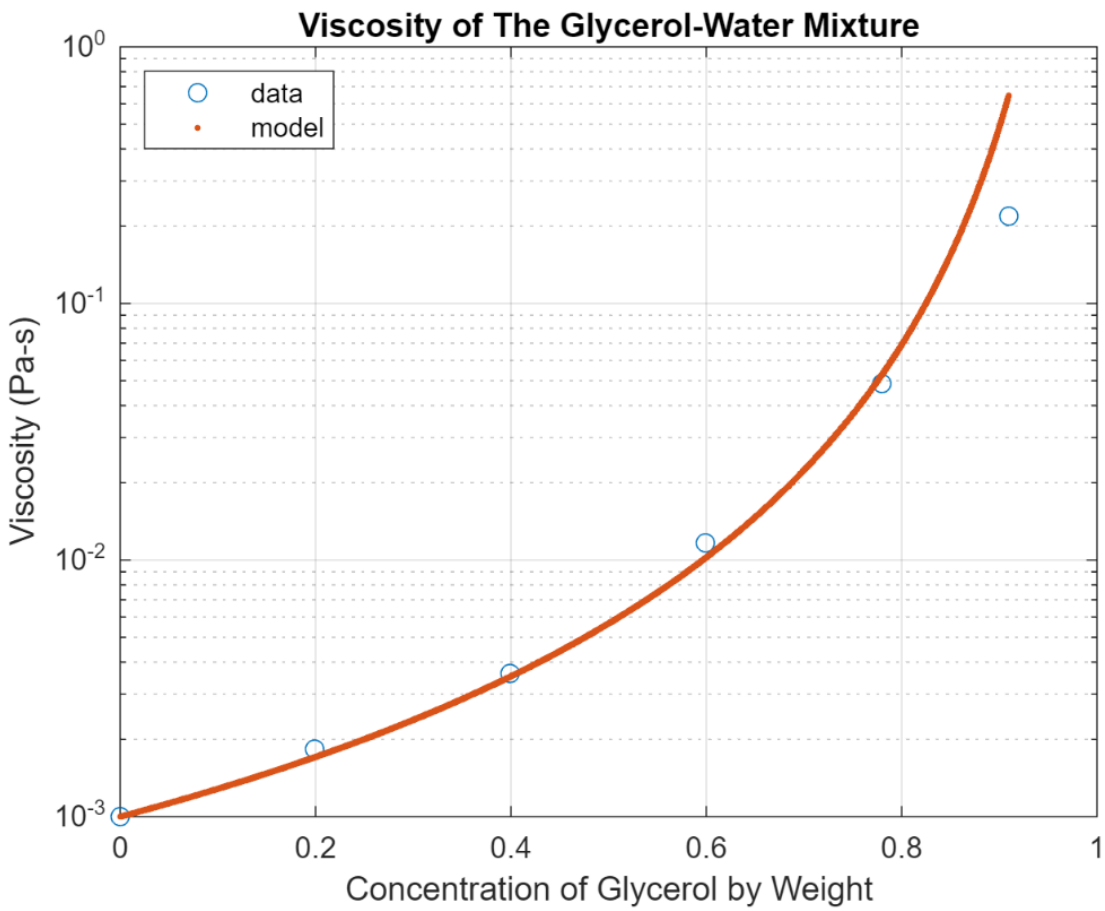

Figure 2.4: Graph showing fit of the viscosity model with experimental data

At first glance, the model appears to fit the data from Tamakura et al. (2012) quite well; however, because the graph is plotted on a logarithmic scale, small discrepancies between the plotted points and the model line may indicate significant errors in the magnitude of the data points compared to the viscosity predicted by the model. A logarithmic interpolation model, as visualized in Figure 2.5, can help address this issue. It is important to note that both the interpolated and theoretical models were found to be fairly accurate and were tested for experimental design. The outputs of the two models were compared, and no differences in design decisions were made based

on the differing outputs.

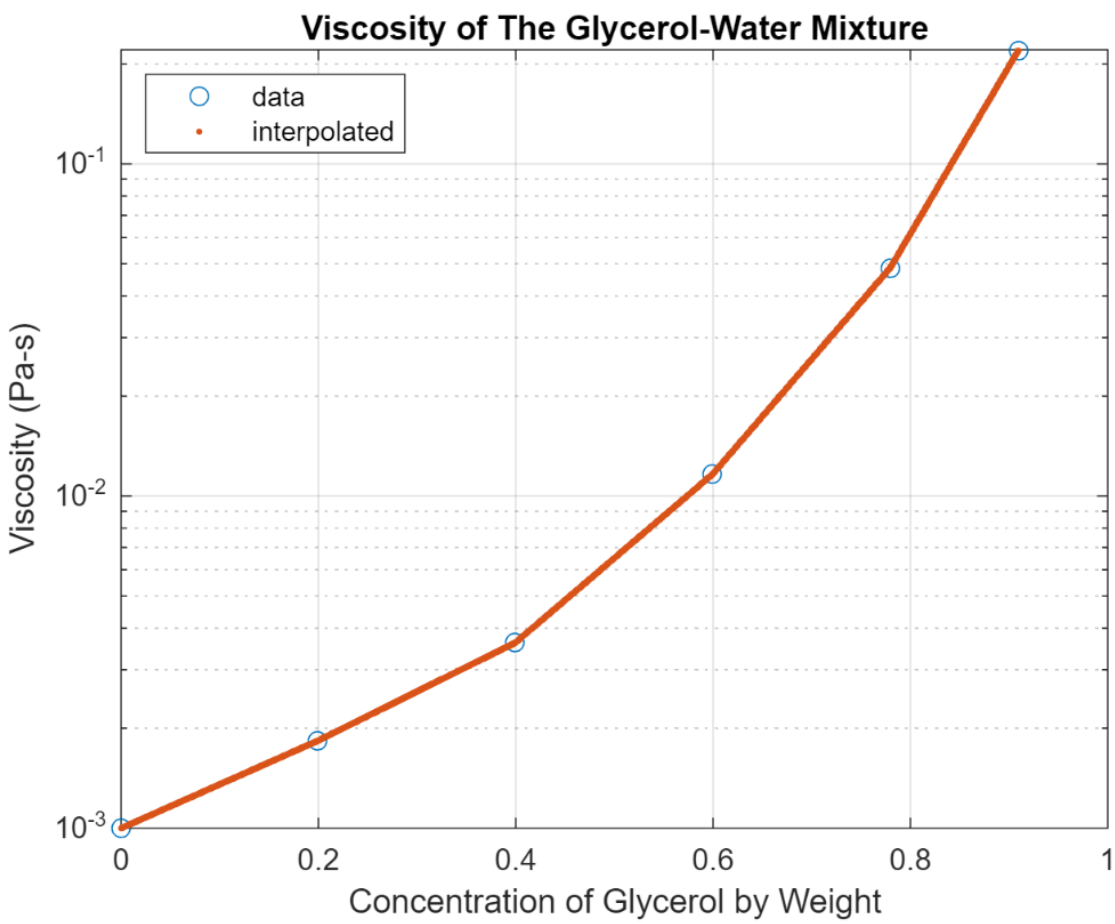

Figure 2.5: Graph showing fit of the interpolated viscosity model with experimental data

2.2. Analysis Background

Dimensionless numbers are commonly used to characterize specific conditions within a fluid system. In this study, five dimensionless numbers are particularly relevant: the Reynolds number, the Eötvös number, the Morton number, the Archimedes number, and the Capillary

number. Each of these is summarized in Table 2.2.

Table 2.2 Summary of relevant dimensionless numbers.

Name	Definition	Intuition
Reynolds Number	$Re = \frac{\rho U L}{\mu}$	$\frac{Inertial\ Forces}{Viscous\ Forces}$
Eötvös Number	$E_o = \frac{\Delta\rho g d_{eq}^2}{\sigma_L}$	$\frac{Gravitational\ Forces}{Surface\ Tension\ Forces}$
Morton Number	$M_o = \frac{\Delta\rho g \mu_L^4}{\rho_L^2 \sigma_L^3}$	$\frac{Gravitational\ Forces}{Surface\ Tension\ Forces}$
Archimedes Number	$Ar = \frac{d_{eq}^3 \rho_L^2 g}{\mu_L^2}$	$\frac{Gravitational\ Forces}{Viscous\ Forces}$
Capillary Number	$Ca = \frac{\mu U}{\sigma}$	$\frac{Viscous\ Forces}{Surface\ Tension\ Forces}$

The Reynolds Number has numerous applications, several of which are relevant to this study. Its significance lies in its ability to quantify the level of turbulence within a specific region of interest. Turbulence can be described as the variation in speed and direction of flow within that region. Generally, a higher Reynolds Number indicates more turbulent flow. The Reynolds Number is defined as:

$$Re = \frac{\rho U L}{\mu}, \tag{8}$$

where ρ represents the density of the medium, U represents the speed of the medium, L represents the characteristic length, and μ represents the dynamic viscosity of the medium.

The definition of characteristic length depends on the system being studied; for the purposes of this study, it can be the bubble equivalent diameter (d_{eq}) or the hydraulic diameter (d_h). The hydraulic diameter can be defined as

$$d_h = \frac{4A}{P_W}, \tag{9}$$

where A represents the cross-sectional area of the flow, and P_W is the wetted perimeter of the flow. The wetted perimeter is the portion of the perimeter of the cross section that is in contact with the flow. For example, for a square pipe, the wetted perimeter would be $4w$ where w represents the width of the pipe. However, for an open square channel, the wetted perimeter would be $3w$.

The bubble equivalent diameter is defined as

$$d_{eq} = \sqrt[3]{\frac{6V_b}{\pi}}, \tag{10}$$

where V_b represents the volume of the bubble. When applying the Reynolds number to two phase flow with bubbles, the following equation is used:

$$Re = \frac{\rho_L v_r d_{eq}}{\mu_L}, \tag{11}$$

where ρ_L represents the density of the liquid phase, v_r represents the relative velocity of the bubble, and μ_L represents the dynamic viscosity of the liquid phase. There are a variety of methods for calculating the terminal velocity of a bubble. In the case of a single bubble rising in an infinite

medium, v_r becomes the terminal velocity v_t.

A rough approximation of the terminal velocity of a bubble can be made with Stoke's law, defined as:

$$U_{st} = \frac{d_{eq}^2 g \rho_L}{18\mu_L}, \tag{12}$$

where U_{st} represents the terminal velocity of the bubble. While this approximation is useful, more accurate models have been developed for predicting bubble terminal velocity. In this paper, the model used is the one defined by Nguyen and Schulze (2004). This model is based on five different equations, each applied to a specific range of the Archimedes Number. The Archimedes Number characterizes the effect of density differences in two-phase flow on the motion of the flow. For bubbly flow, it is defined as:

$$Ar = \frac{d_{eq}^3 \rho_L (\rho_L - \rho_g) g}{\mu_L^2}, \tag{13}$$

where ρ_g represents the density of the gas phase and g represents the acceleration of gravity. For this model, if the Archimedes Number of the system is less than or equal to 12,332, the terminal velocity of the bubbles is given by:

$$v_T = U_{st} / \left[1 + \frac{\frac{Ar}{96}}{(1 + 0.079 Ar^{0.749})^{0.755}} \right], \tag{14}$$

Otherwise, the terminal velocity is given by:

$$v_T = 18 U_{st} \left(\frac{4a^2 Ar^{2b-1} M_o^{0.46b}}{3k} \right)^{\frac{1}{2-2b}}, \tag{15}$$

where M_o represents the Morton Number which will be defined later in this section, k is a constant, and a and b are constants defined in Table 2.3 for various ranges of the Archimedes Numbers. It

is important to note that this constant *k* differs from the one used in the definition for the viscosity of glycerin-water mixtures. In this context, the value of *k* is 0.95.

Table 2.3: *Appropriate values of constants a and b*

Constraints	**a**	**b**
$12,332 < Ar \leq 3.158M_o^{-0.46}$	1	0
$3.158M_o^{-0.46} < Ar \leq 29.654M_o^{-0.46}$	1.14	-0.176
$29.654M_o^{-0.46} < Ar \leq 506.719M_o^{-0.46}$	1.36	-0.280
$506.719M_o^{-0.46} < Ar$	0.62	0

The Reynolds number in combination with the Morton Number and Eötvös Number are used to characterize two phase flow as illustrated in Figure 2.6. The significance of M in Figure 2.6 is the Morton Number. The Morten number can be defined as:

$$M_o = \frac{(\rho_L - \rho_g)g\mu_L^4}{\rho_L^2\sigma_L^3}, \tag{16}$$

where σ_L represents the surface tension of the liquid phase. The Eötvös Number can similarly be defined as:

$$E_o = \frac{(\rho_L - \rho_g)gd_{eq}^2}{\sigma_L}. \tag{17}$$

It differs from the Morton Number with a dependency on the equivalent diameter of the bubble.

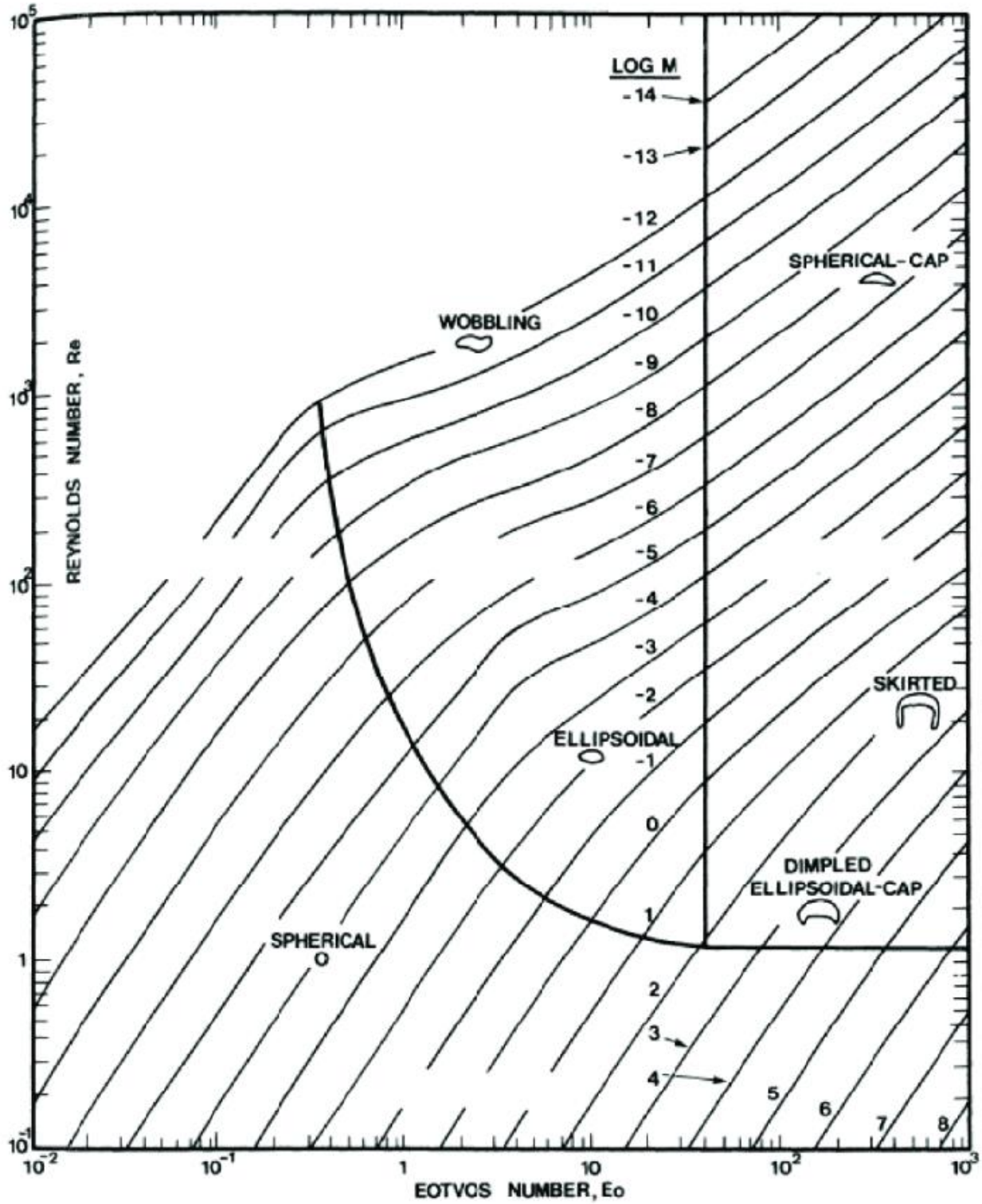

Figure 2.6: Shape regimes of bubbles defined by Reynolds, Eötvös, and Morton numbers courtesy of (Clift et al., 1978)

The final significant dimensionless number used in this study is the Capillary Number defined as:

$$Ca = \frac{\mu U}{\sigma}. \tag{18}$$

This number relates viscous forces to surface tension forces. In this study, the Capillary Number is used alongside the Reynolds Number to characterize microfluidic systems, as detailed in Section 2.4.

2.3. Dimensionless analysis

Before experimental design can proceed, it is essential to identify and define the conditions this study aims to replicate. As discussed in Section 2.3, these conditions can be classified using dimensionless numbers. In the MSRE, the salt temperature varied between 600°C and 700°C. This temperature range will be used to determine the corresponding ranges for the Reynolds Number, Morton Number, and Eötvös Number, as the fluid properties of the salt change with temperature. These variations are summarized in Table 2.4 and highlighted by the red box in Figure 2.7. These ranges will serve as the target parameters for the surrogate fluid in this study.

Table 2.4: Target values of dimensionless numbers

	600°C	**700°C**
$\boldsymbol{M_o}$	$3.486 * 10^{-9}$	$7.42 * 10^{-10}$
$\boldsymbol{Re}$	1.9742	4.0166
$\boldsymbol{E_o}$	0.0189	0.0198

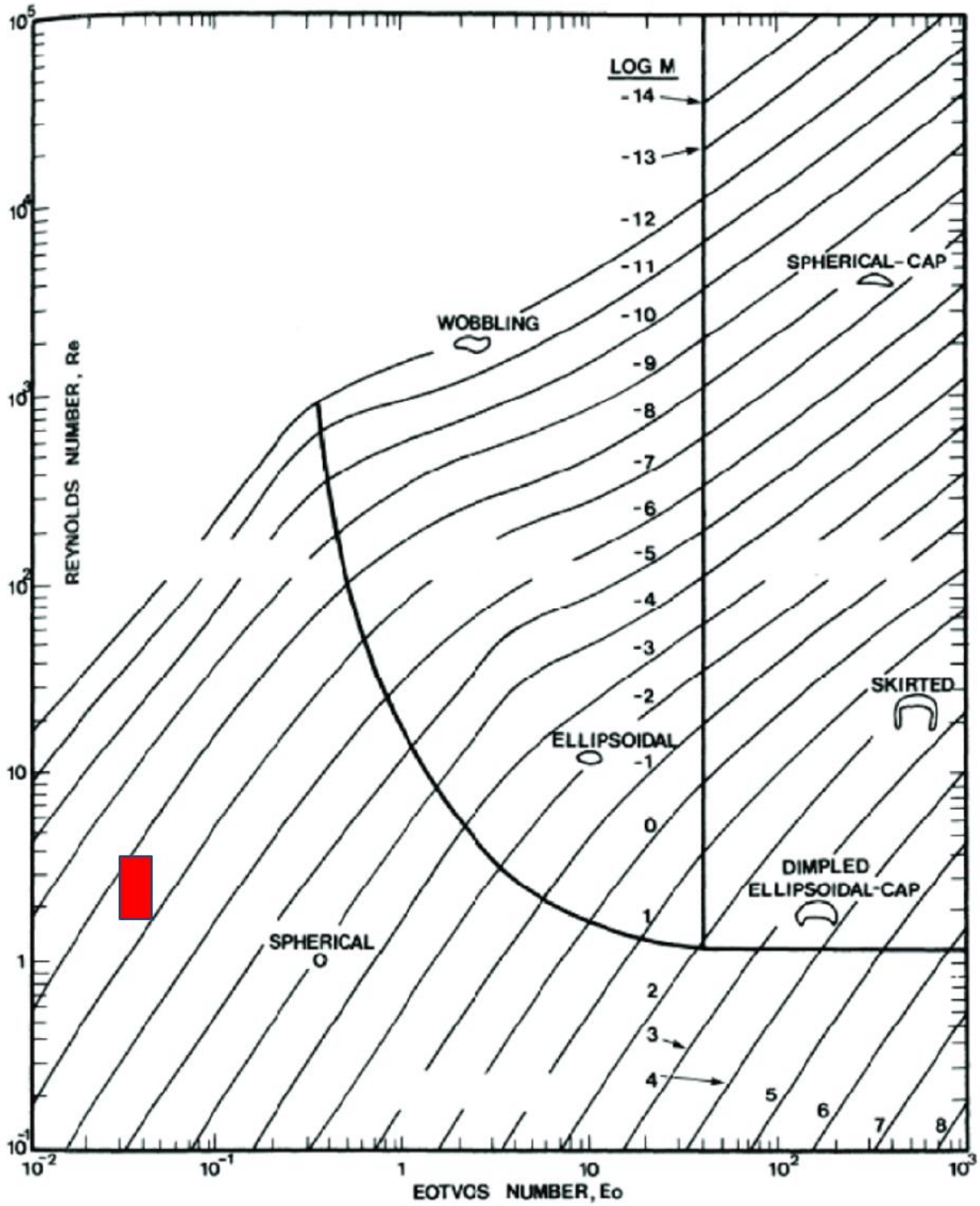

Figure 2.7: Region of acceptable dimensionless numbers on shape regime graph courtesy of (Clift et al., 1978)

The process begins by determining the fluid properties of the salt using the relations outlined in Section 2.1. Next, the Stokes velocity, along with the Eötvös, Morton, and Archimedes Numbers, are calculated using Equations (12), (17), (16), and (13), respectively, based on the properties at the specified temperature and the equivalent diameter of the bubbles. The terminal velocity is then determined using Equations (14) and (15), as appropriate. With this information, the Reynolds Number can be calculated using Equation (11).

The next step involves replicating these numbers in the surrogate fluid system, which has two degrees of freedom: the weight ratio of glycerin and the equivalent diameter of the bubbles. Conveniently, the Morton Number is independent of the equivalent diameter, so it is used first to establish a preliminary acceptable range for the glycerin weight ratio in the surrogate fluid. Both the Reynolds Number and Eötvös Number depend on both the equivalent diameter and the glycerin weight ratio. Although working with variables that have two dependencies can be complex, it becomes manageable using matrices.

Using the methods discussed in Section 2.1, this study first defines a weight ratio vector of length 10,000, ranging from 0 to 0.9, to represent all possible concentrations of glycerin in the surrogate fluid. An equivalent diameter vector, also of length 10,000, is similarly defined, ranging from 0 mm to 1 mm, to cover the likely range of equivalent diameters that would satisfy the conditions outlined in Table 2.4. The Morton Number is then calculated in vector form for each weight ratio in the weight ratio vector. The constraints on the Morton Number are applied, resulting in a new weight ratio vector containing only the values that satisfy the Morton Number conditions. The Morton Number after applying these constraints is visualized in Figure 2.8

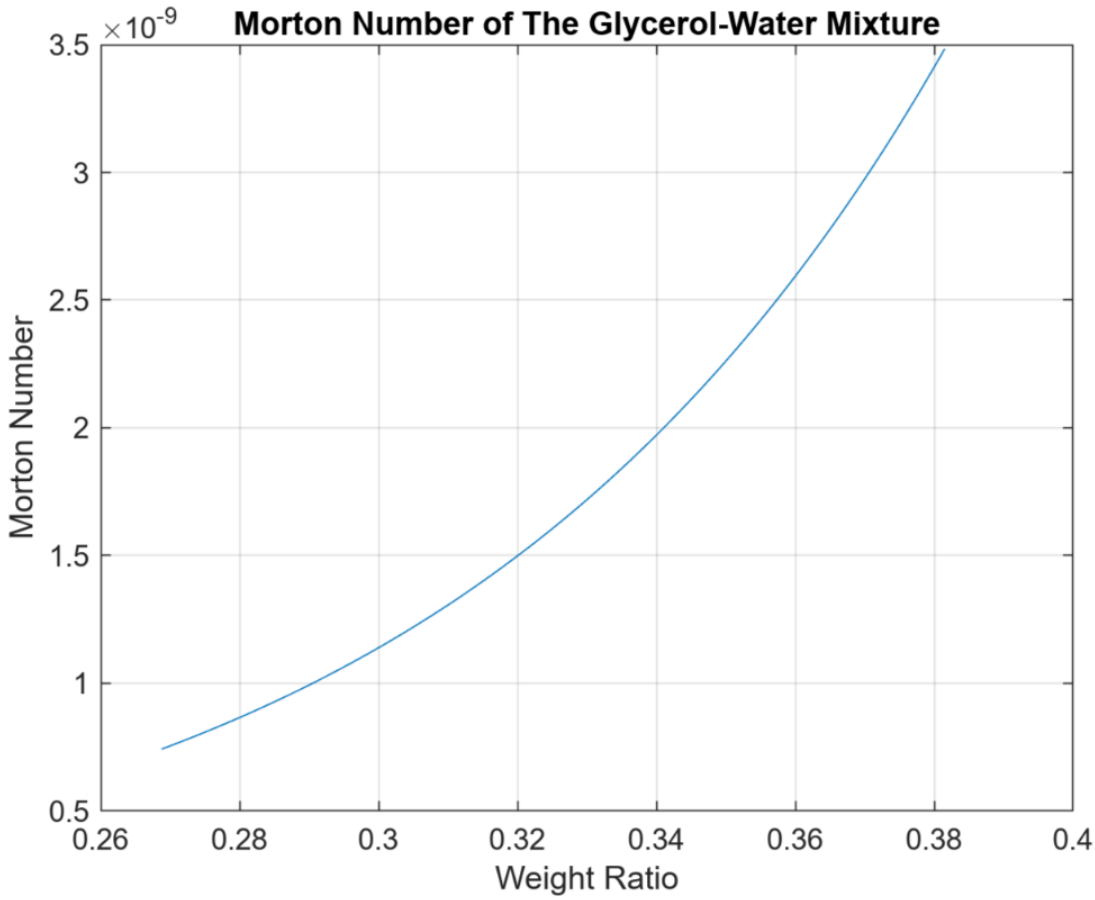

Figure 2.8: Plot to visualize the acceptable range of the Morton Number

The Reynolds Number was then calculated in a matrix, where the rows represent steps in the equivalent diameter and the columns represent steps in the weight ratio, corresponding to the values in the respective equivalent diameter and new weight ratio vectors. The process for calculating each element in the Reynolds Number matrix was similar to the method used earlier in this section for the molten salt, involving the calculation of the Stokes velocity, Archimedes Number, and Morton Number to determine the terminal velocity, which was then used to calculate

the Reynolds Number.

Next, the limitations on the Reynolds Number were applied to this matrix, and all values outside the target range were removed, leaving only the elements that satisfy the conditions. The matrix after these limitations were applied is visualized in Figure 2.9. The range of the equivalent diameter and weight ratio vectors was then adjusted by removing the indices that did not have an acceptable Reynolds Number value in their respective row or column.

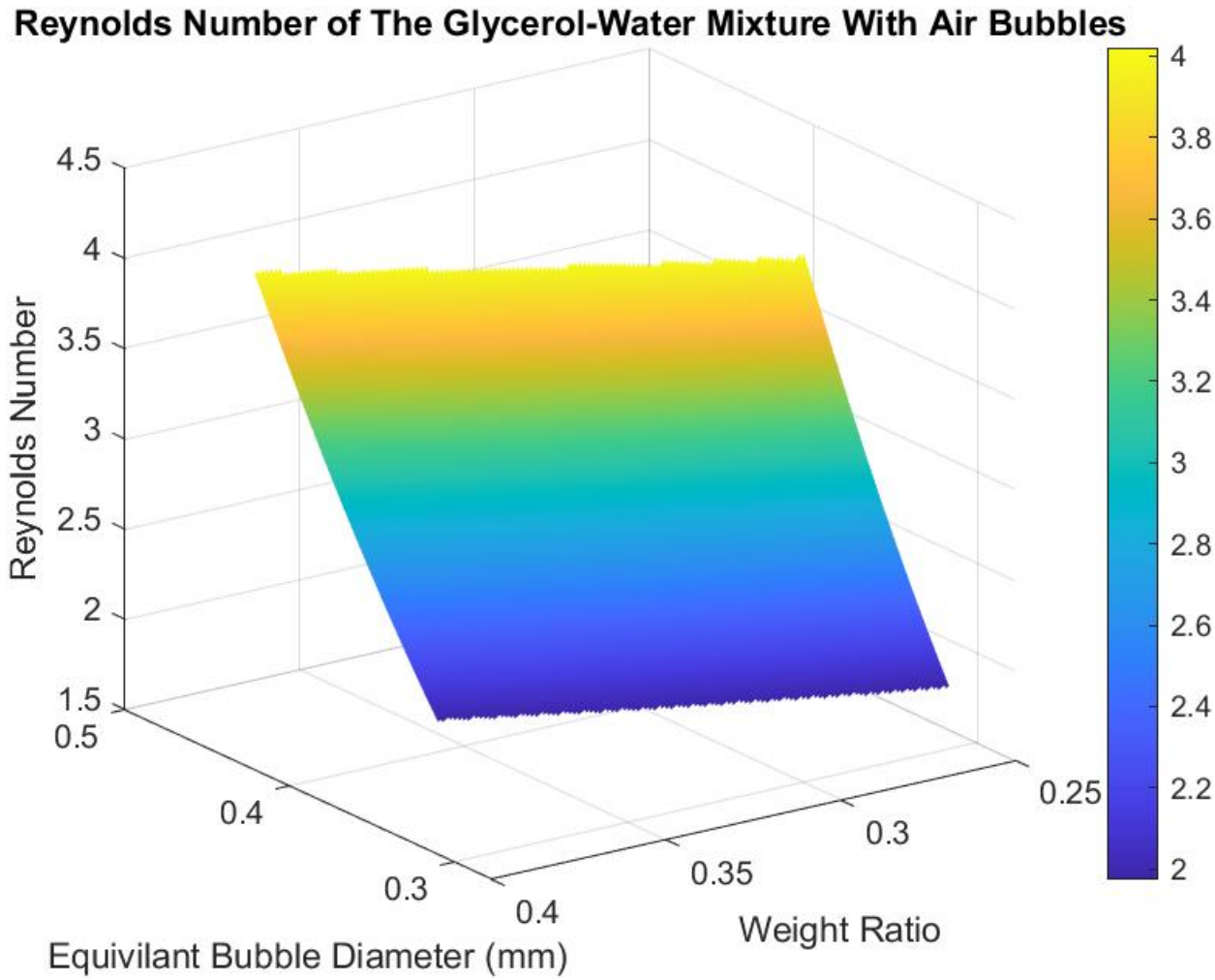

Figure 2.9: Surface plot to visualize the acceptable range of the Reynolds Number

A similar process was used to further narrow down the range of acceptable equivalent diameters and weight ratios based on the limitations of the Eötvös Number. The Eötvös Number was calculated for all the values in the modified equivalent diameter and weight ratio vectors, corresponding to the respective rows and columns of a matrix. The limitations on the Eötvös

Number were then applied, and all values outside the acceptable range were removed. The resulting matrix is visualized in Figure 2.10.

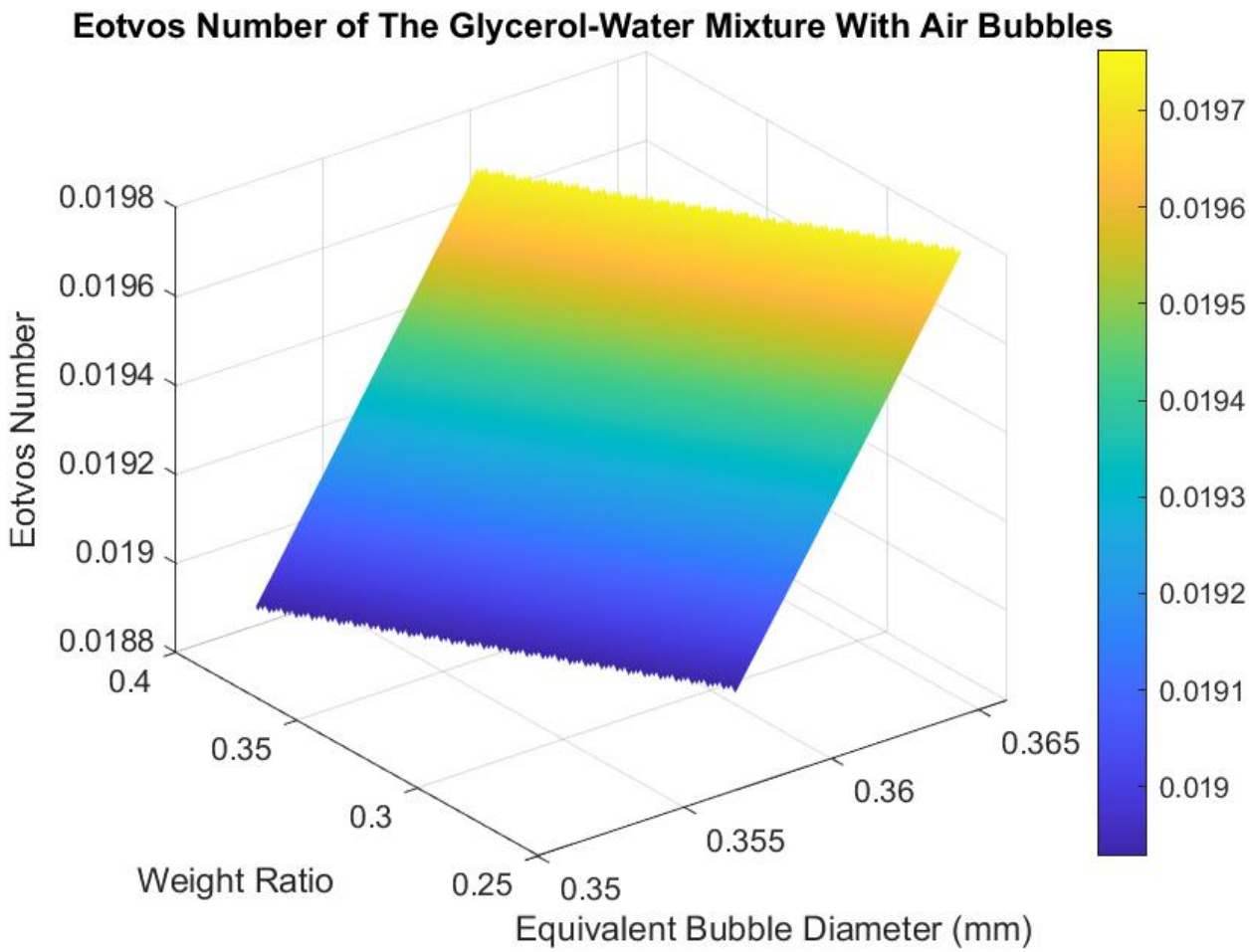

Figure 2.10: Surface plot to visualize the acceptable range of the Eötvös Number

The first key takeaway from this dimensionless analysis is that the surrogate fluid for this study should consist of 35% glycerin by weight. This composition falls within the acceptable range of 27%-40% while providing a margin for fluctuation and nonuniformity in concentration, as it

represents the median acceptable value for the weight ratio. The second important insight is that the validity of this surrogate fluid system in simulating conditions in molten salt is highly sensitive to the equivalent diameter of the bubbles. The acceptable range for this property is narrow, from 0.35 mm to 0.365 mm. Therefore, a process that can very precisely and accurately inject small bubbles into the test section is essential for the study of bubble dynamics in molten salt reactors. The definition of such a process is the purpose of this study.

2.4. Microfluidics

The method used for bubble size control in this study is microfluidics, which involves studying the behavior of fluids as they move through microchannels. Microchannels are typically less than one millimeter in diameter and are often made from materials like glass and polydimethylsiloxane (PDMS), a clear, elastic, and rubbery material. PDMS is useful for microfluidics as it is rather easy to fabricate microchannels into it by pouring it into a mold created with soft lithography or 3D printing. Microfluidic systems are commonly used for various fluid processing applications, one of which is droplet-based microfluidics.

Droplet-based microfluidics is a technique for creating very small and consistently sized pockets of a dispersed phase within a continuous phase, as visualized in Figure 2.11. For this method to work, the continuous and dispersed phases must have considerable interfacial or surface tension. Numerous experiments have been conducted using different substances for both the continuous and dispersed phases. For this study, the most relevant are those that use air as the dispersed phase, as this is the method for microfluidic bubble size control. Air is also used in this

case as the surface tension of the surrogate fluid, as discussed in Section 2.1, assumes that the interfacial gas is air.

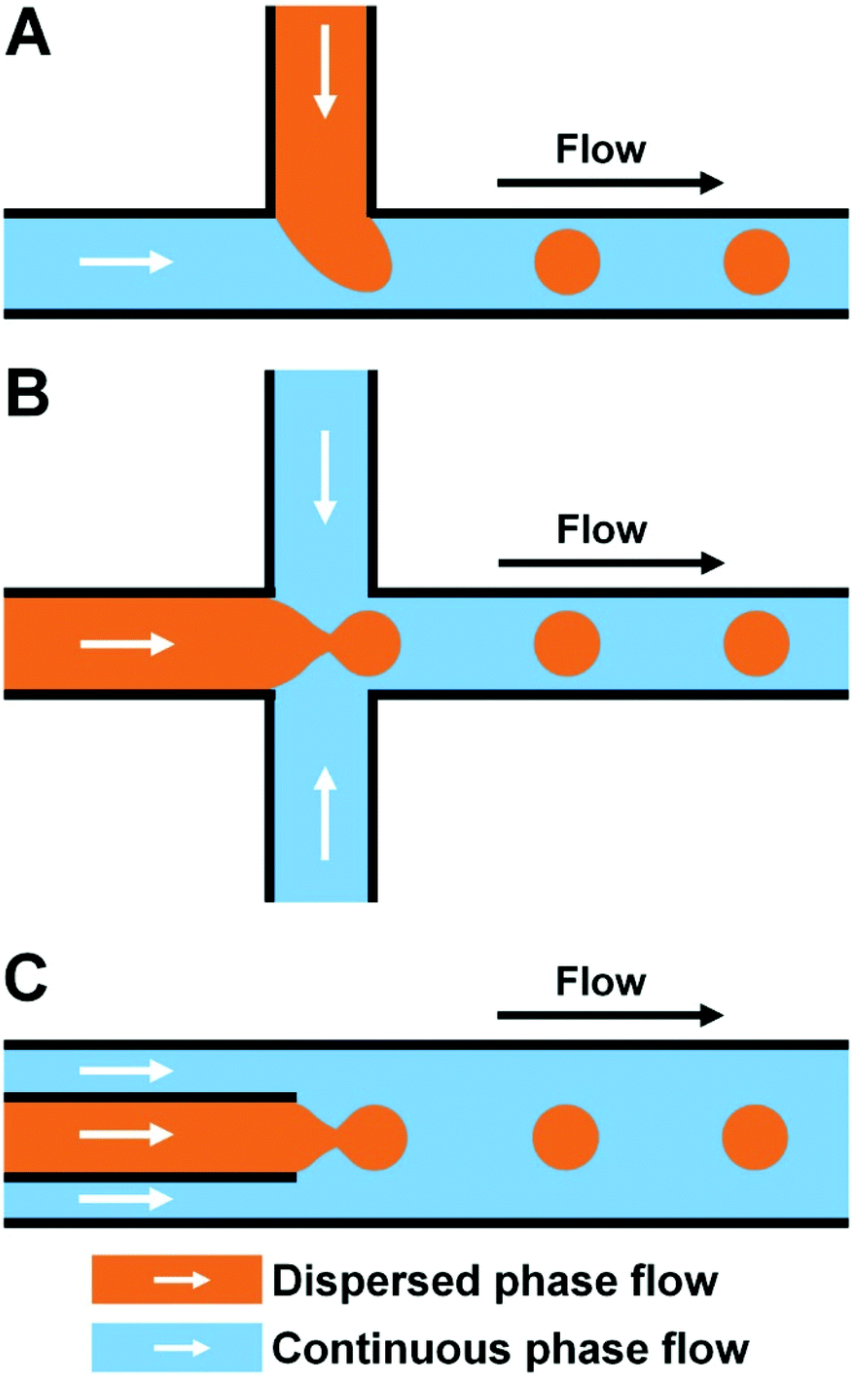

Figure 2.11: Visualization of (A) T-junction structure. (B) Flow-focusing structure. (C) Coaxial focusing structure for microfluidic devices (Liu et al., 2022)

The function of microfluidic systems is often characterized by the Capillary number of the microchannels. The importance of the Capillary number in this context lies in its ability to define the droplet formation regime. At low Capillary numbers ($Ca < 10^{-2}$) the viscous forces of the continuous phase are insufficient to overcome the interfacial tension between the dispersed and continuous phases. As a result, the flow of the dispersed phase blocks the inlet of the continuous phase until the pressure builds up enough to push the droplet or bubble through the outlet. Conversely, at higher Capillary numbers ($Ca > 10^{-2}$) the viscous forces of the continuous phase are strong enough to quickly shear the droplets or bubbles from the dispersed phase and drive them into the outlet (Garstecki, 2010)

Lu et al. (2014) propose a model for controlling bubble size within a flow-focusing microfluidic device, achieving a production frequency of up to 38.6 bubbles per second with diameters as small as 0.69 mm. The model predicts bubble size using the following equation:

$$\frac{V_b}{w^3} = 1.12\varphi^{0.52}Ca^{-0.29}, \tag{19}$$

where V_b represents the volume of the bubbles produced, w represents the width of the microchannels, and φ denotes the flow rate ratio defined as:

$$\varphi = \frac{Q_g}{Q_l}. \tag{20}$$

Here, Q_g represents the flow rate of the gas (dispersed phase) and Q_l represents the flow rate of the liquid (continuous phase). Intuitively, a higher φ value corresponds to a larger bubble volume, as more gas is being introduced into the system relative to the liquid (Lu et al., 2014).

This model will serve as the design basis for the injector in this study, as the predicted bubble size aligns with the target specifications, and the bubble generation frequency is large

enough that plenty of bubbles could be injected into the 1 cm by 3 cm test section used for this study. However, the model has not been validated for scaling to meet the bubble size requirements of this study. To apply this model to the current study, the channel width will be reduced, and the continuous phase will have different properties than those tested in the original model.

Chapter 3

3. Injector Design

3.1. PDMS Chip Design and Fabrication

The first critical step in the design process is creating the PDMS chip with integrated microchannels. The study builds on the work of Lu et al. (2014), which investigated a flow-focusing geometry with microchannels featuring square cross-sections of 0.6 mm in width. Given that the target bubble size for this study is 0.355 mm, the microchannel width was reduced to 0.4 mm. Although Lu did not specifically test this configuration, similar devices can produce bubbles with a diameter approximately 60% of the channel width (Wang et al., 2021). Channel geometry is just as important as channel width for the injector design.

The first consideration for microchannel geometry is the type of microfluidic structure. Since this study is based on the flow-focusing device from Lu et al. (2014), the same geometry is replicated, with the air (dispersed phase) flowing parallel to the outlet and the surrogate fluid (continuous phase) flowing perpendicular to the air at the T-junction, as illustrated in Figure 3.1.

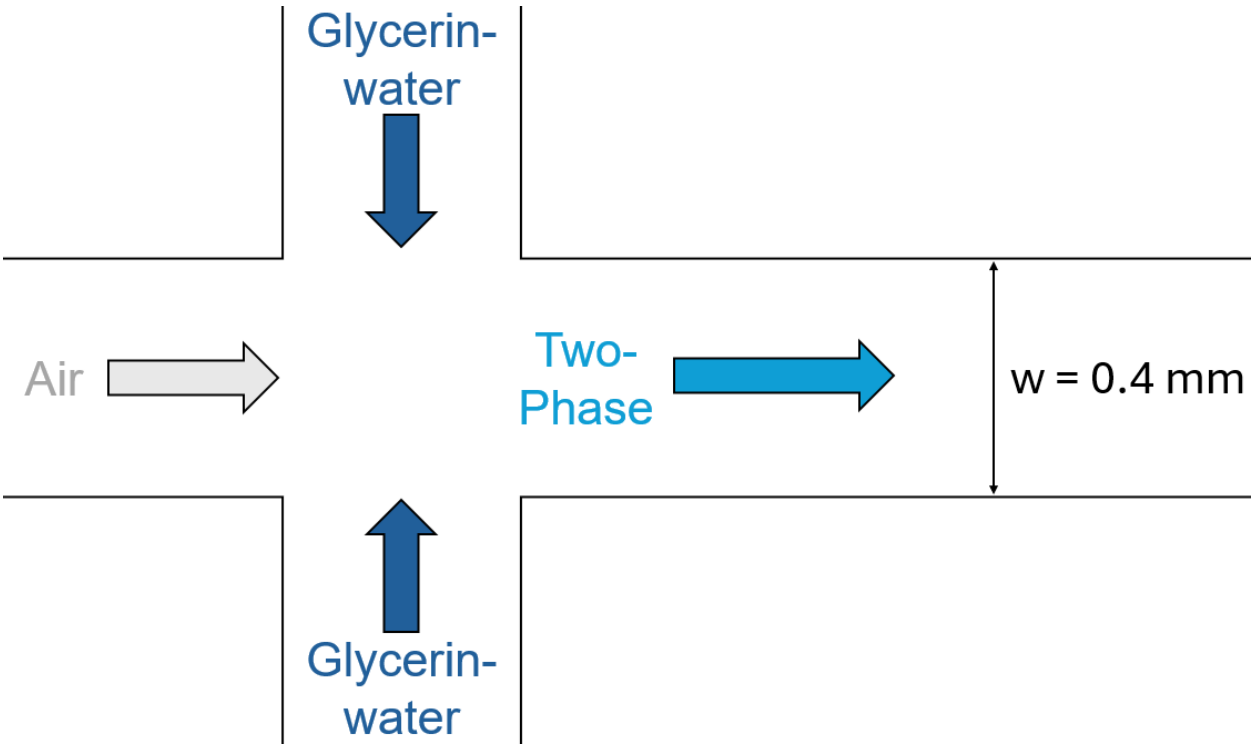

Figure 3.1:Visualization of the T-junction geometry

Based on design calculations using the bubble size control model, the estimated bubble production frequency is 10 Hz. This number was obtained from staying within the Capillary Number range Lu et al. (2014) tested. The flow rates that result from this are 1.3 ml/hr for air and 145 ml/hr for the surrogate fluid. Given that this frequency is relatively low, two injection channels are required. The test section for this injector has a width of 3 cm, so even distribution of bubbles across the section is essential. To achieve this, the channels are spaced 1 cm apart, with each positioned 1 cm from the section walls. The final microchannel geometry is shown in Figure 3.2.

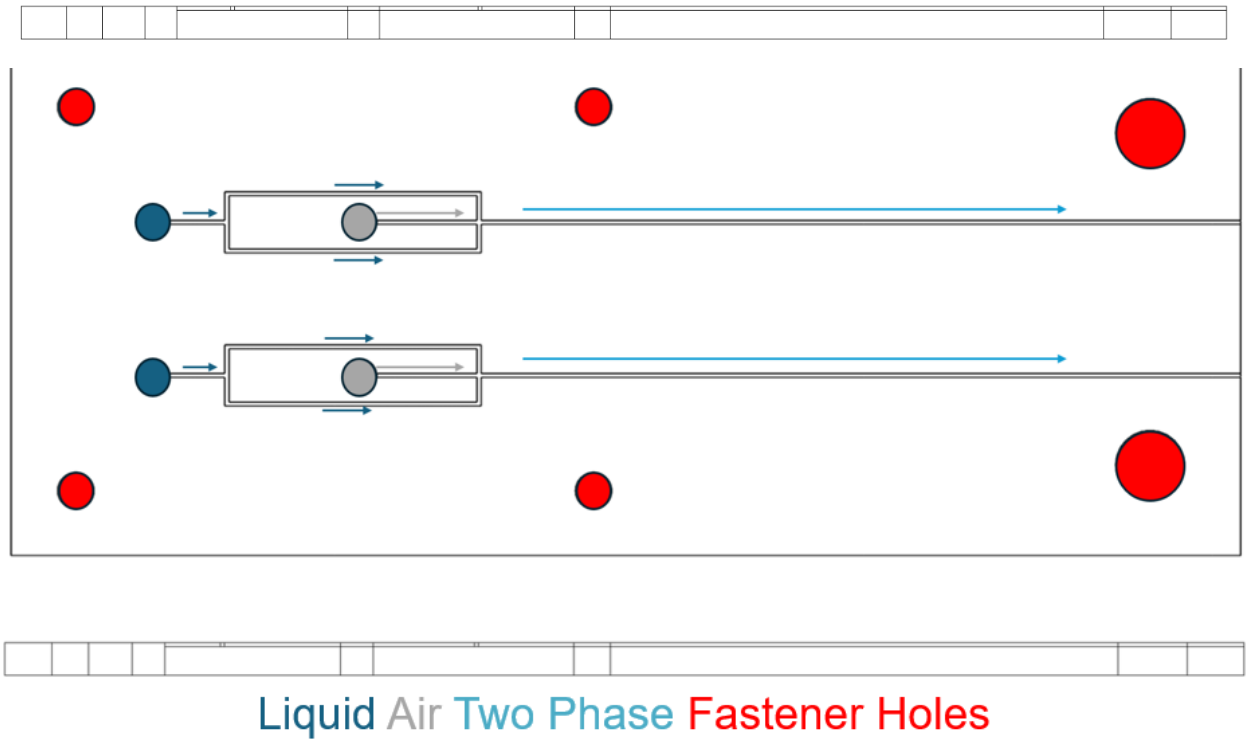

Figure 3.2: Final geometry of the PDMS chip

The circles in Figure 3.2 connected to the microchannels, represent the inlets for the surrogate fluid and air. The two inlets on the left side are for the surrogate fluid, while the two on the right are for the air. The circles along the chip's border indicate fastener placements, as discussed in Section 3.2. This geometry serves as the basis for fabricating a mold, which is created by forming a negative of all the chip's desired features. A CAD model of the mold is shown in Figure 3.3. Upon close inspection, the fastener holes near the outlet are missing, as their necessity was not identified during the initial design phase.

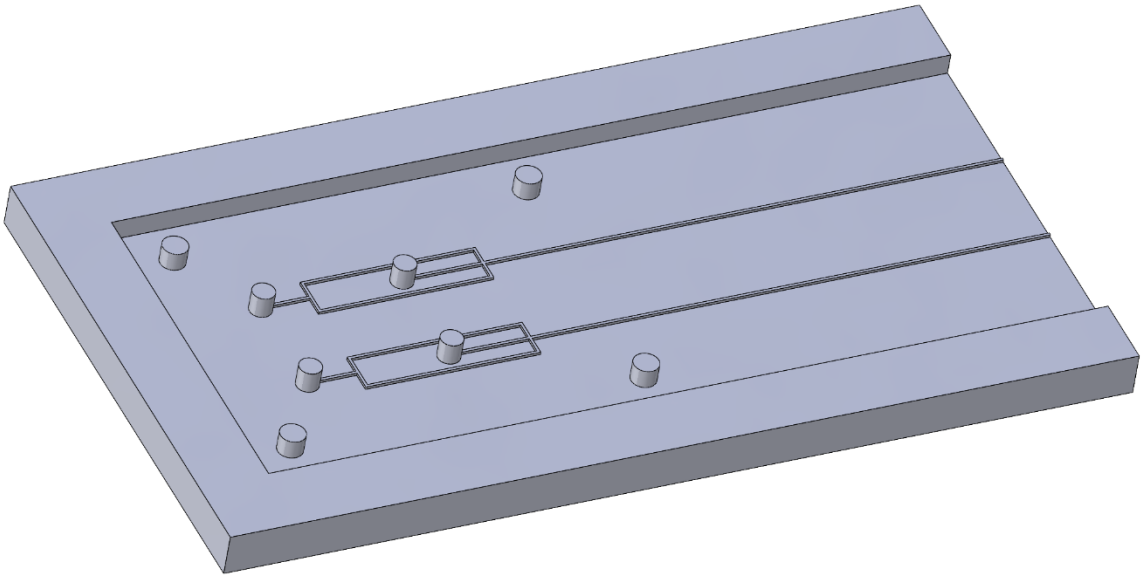

Figure 3.3: CAD model of the PDMS mold

Soft lithography would typically be the ideal method for fabricating microfluidic molds due to its precision; however, the size and complexity of the chip's geometry made this method impractical. Instead, this study utilized 3D printing to fabricate the mold. Recent advancements in 3D printing technology have made producing such molds both accessible and cost-effective. Online services like Xometry and Protolabs offer high-precision prints suitable for this type of application. A photograph of the finished mold fabricated by Protolabs can be seen in Figure 3.4.

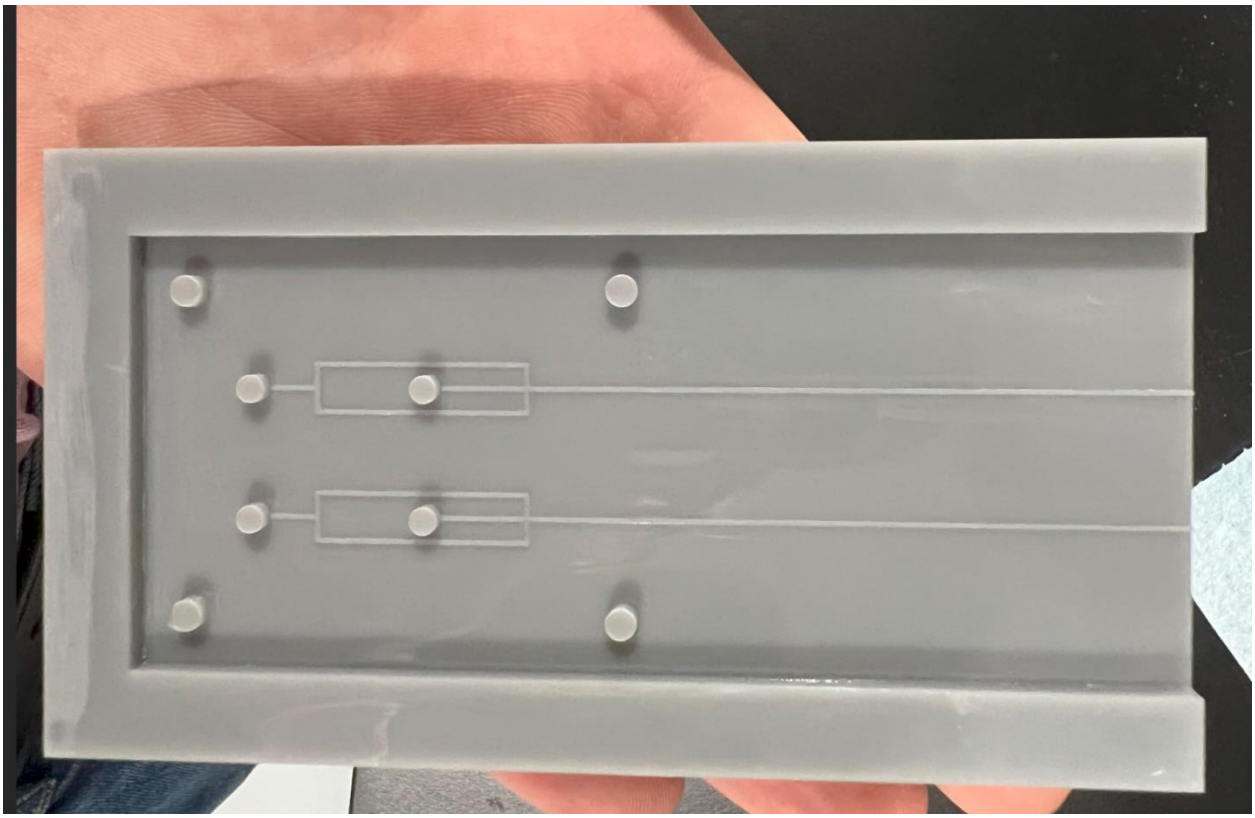

Figure 3.4: 3D printed PDMS mold

Once the mold is ready, fabricating the PDMS chip is a relatively straightforward process. The base compound (dimethylsiloxane) is mixed with a curing agent in a 10:1 ratio by weight. For this study, the SYLGARD 184 Silicone Elastomer Kit was used. After mixing, any trapped air bubbles are removed using a Synthware vacuum glass desiccator, as shown in Figure 3.5 creating a vacuum of -12.5 psi with a GAST Compressor/Vacuum Pump (model: DOA-P704-AA). A useful trick for more effectively eliminating bubbles is to rapidly reintroduce atmospheric pressure rather than doing so gradually. This process was repeated two to three times until most of the bubbles were eliminated. The remaining bubbles were removed with a pipet.

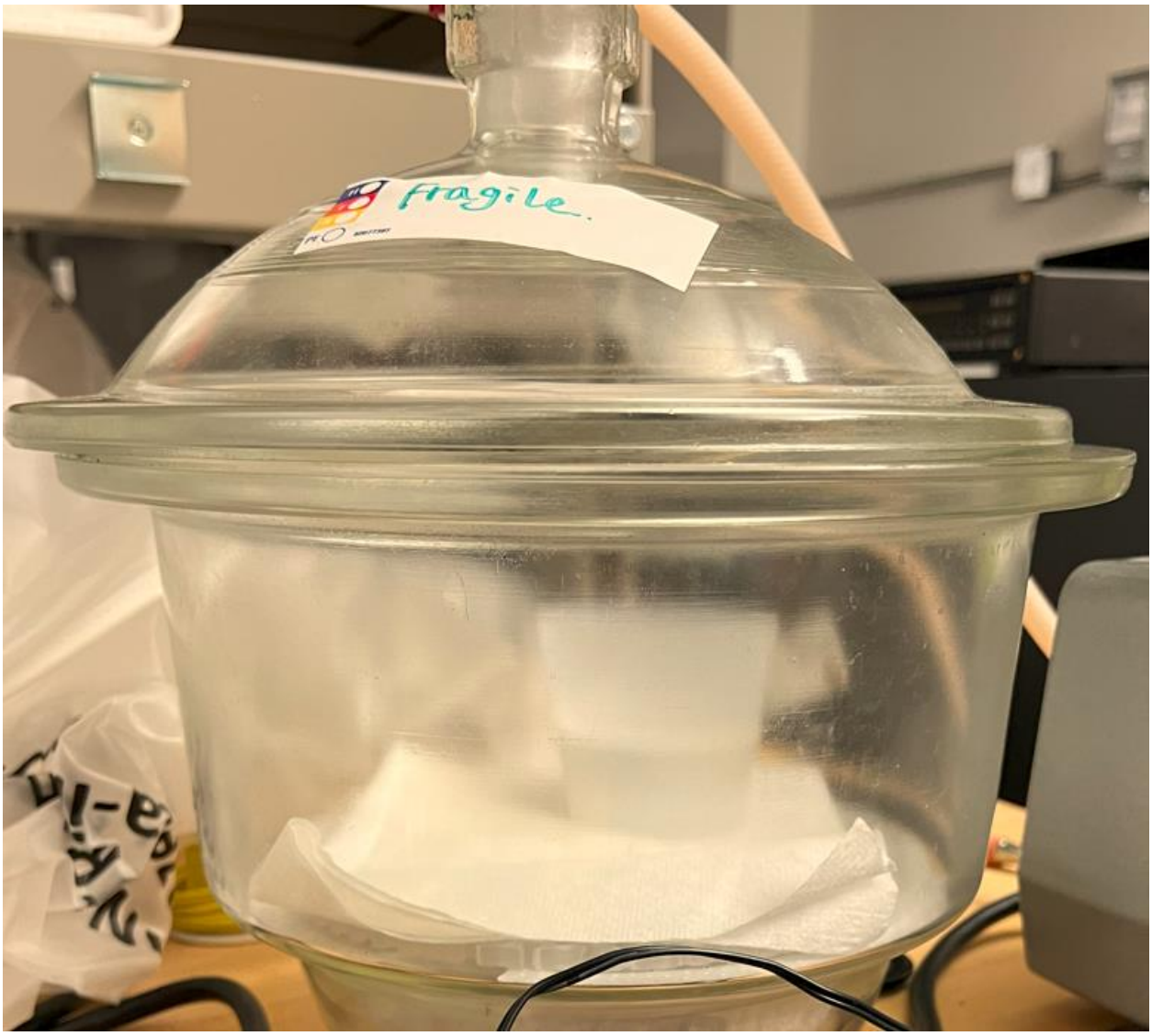

Figure 3.5: PDMS mixture in vacuum chamber

After the bubbles are removed, the PDMS is poured into the mold. Since the mold has an open face for easy removal of the PDMS chip, a small pane of glass is used to cover this side during pouring and curing. To ensure proper and efficient curing, the mold is placed on a hotplate set to 55 ºC. Figure 3.6 displays the mold pouring setup, where the red piece supports the glass

pane, and metal dowel pins are used to create holes for the fasteners. It's important to pour slightly more mixture than needed so it overflows, ensuring the chip is thick enough and doesn't have a concave surface. Laying a piece of acrylic over the mold during curing helps to achieve a flat surface.

Figure 3.6: PDMS mold and curing setup

After curing for a day, the PDMS chip can be removed from the mold. At this stage, any excess material is trimmed away with scissors or a sharp knife.

3.2. Acrylic Sandwich Design and Fabrication

To close the open face of the microchannels in the PDMS and create practical inlets for both the air and surrogate fluid, while also providing a durable structure to prevent damage in a lab environment, acrylic plates are used. Although glass is typically preferred for microfluidic applications due to its adhesive properties with PDMS, the complexity of the injector's geometry makes glass fabrication impractical. Acrylic, chosen for its machinability and transparency, is a suitable alternative. However, because acrylic doesn't adhere to PDMS as strongly as glass, pressure must be applied to ensure a tight seal. This is achieved by sandwiching the PDMS chip between two acrylic slabs, secured by fasteners around the border, as illustrated in Figure 3.7 and Figure 3.8.

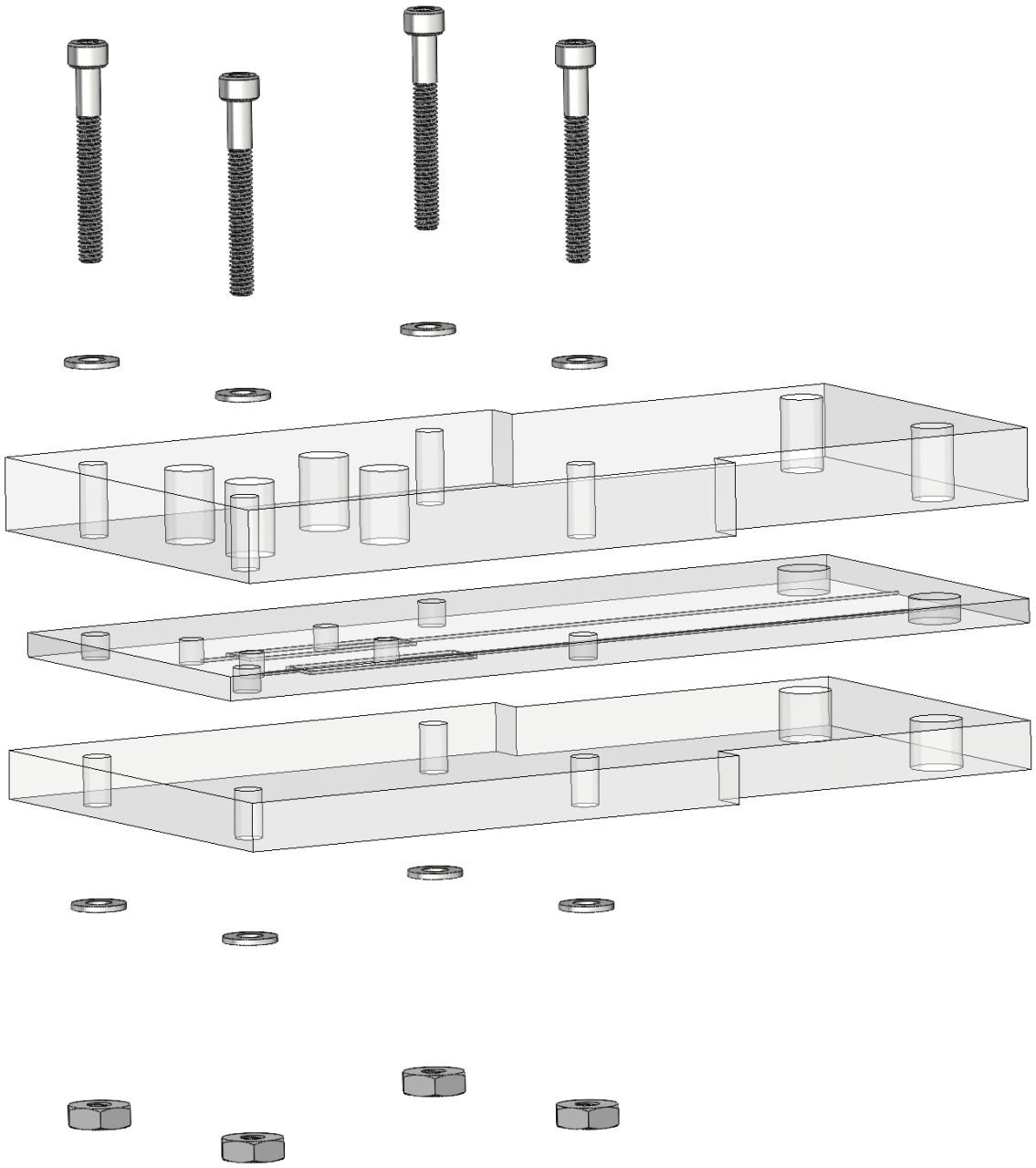

Figure 3.7: Exploded view of acrylic-PDMS sandwich

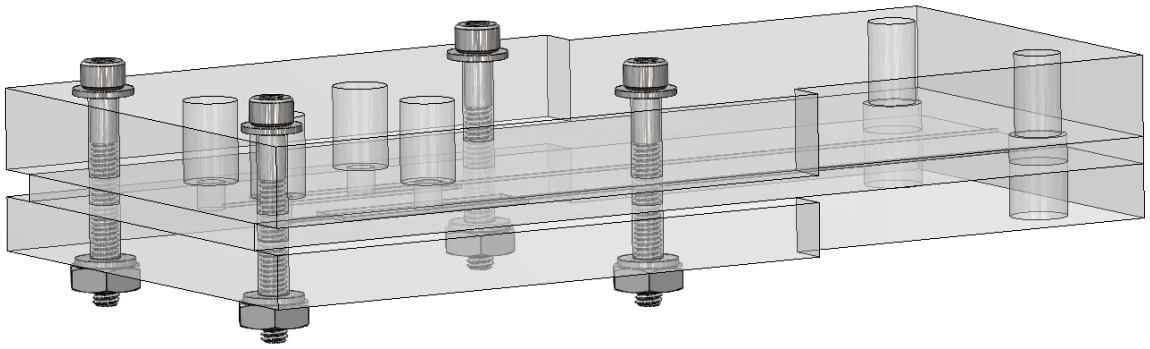

Figure 3.8: Assembled acrylic-PDMS sandwich

The acrylic plates were sourced from McMaster-Carr and were initially cut to size using a horizontal band saw. A CNC router machine was then employed to refine the cuts to tighter tolerances and to create the jutted-out sides for the injector's inlet. These jutted-out sides were initially thought necessary to keep the injector in place but were later deemed unnecessary after further design revisions. The inlet and fastener holes were drilled with a drill press.

To accommodate fittings for the air and surrogate fluid inlets, the acrylic inlet holes were tapped with a 1/16 NPT thread. Brass push-to-connect fittings were installed using Teflon tape and silicone caulk to ensure a proper seal. Figure 3.9 shows a CAD model with the attached fittings, which allow for easy connection and disconnection of 1/8" interior and 1/4" exterior diameter flexible PVC tubing.

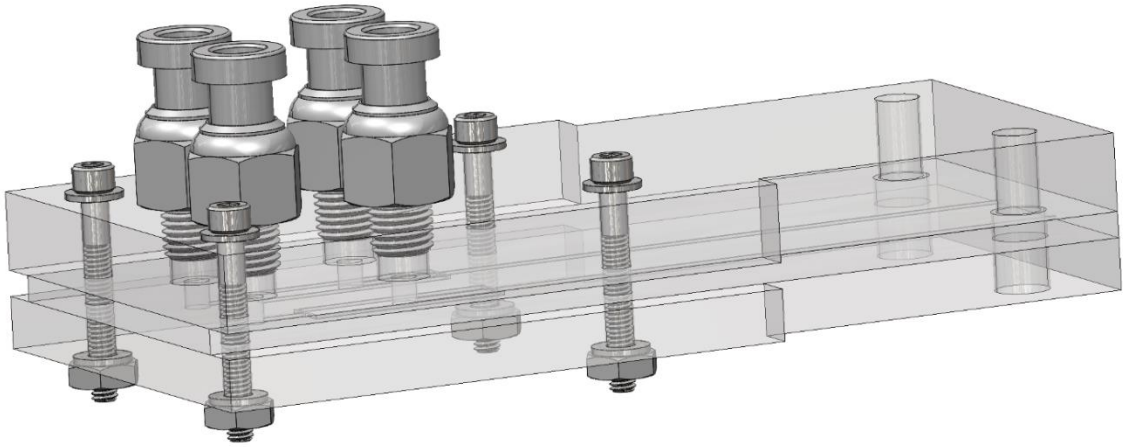

Figure 3.9: CAD model with fittings

Initial calculations did not indicate a need for fasteners at the injector's outlet, but after testing, the design was updated to include them. Holes were drilled in the acrylic slabs, and 1/4-28 female threads were tapped in the acrylic slab with the NPT fittings. For tabletop validation, the injector was configured as shown in Figure 3.10.

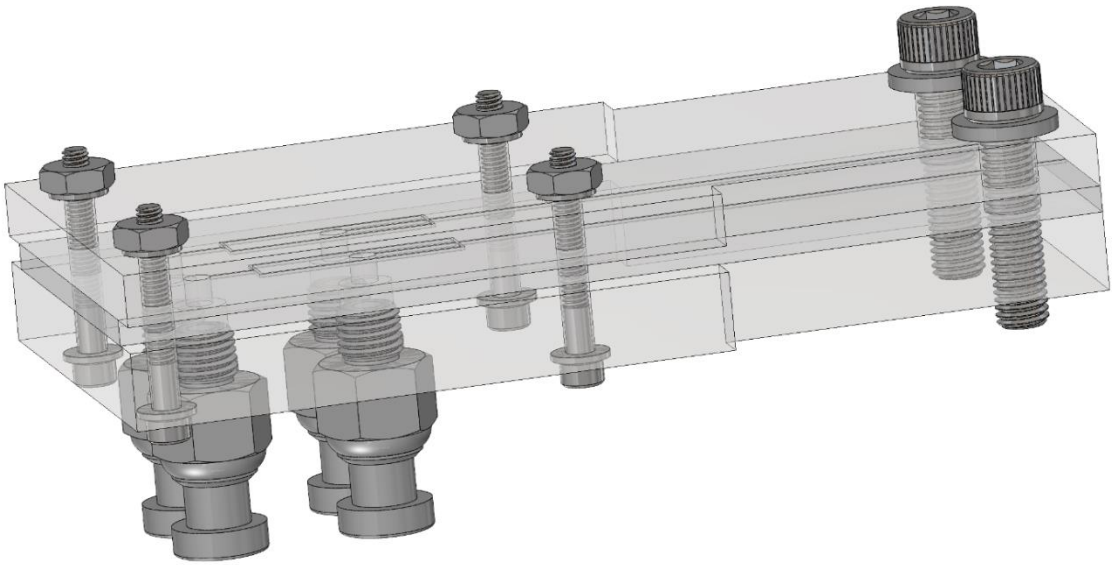

Figure 3.10: CAD model of injector for outside test loop testing

This setup provides excellent visibility for validating bubble formation outside the test section. However, the injector is ultimately designed to be inserted into the test section detailed in Section 3.4. To achieve this, a flange was required. Song (2018) established the geometry for fitting an injector into the test section in the same lab as this study, so this design was modified to accommodate the microfluidic injector. The flange design is shown in Figure 3.11.

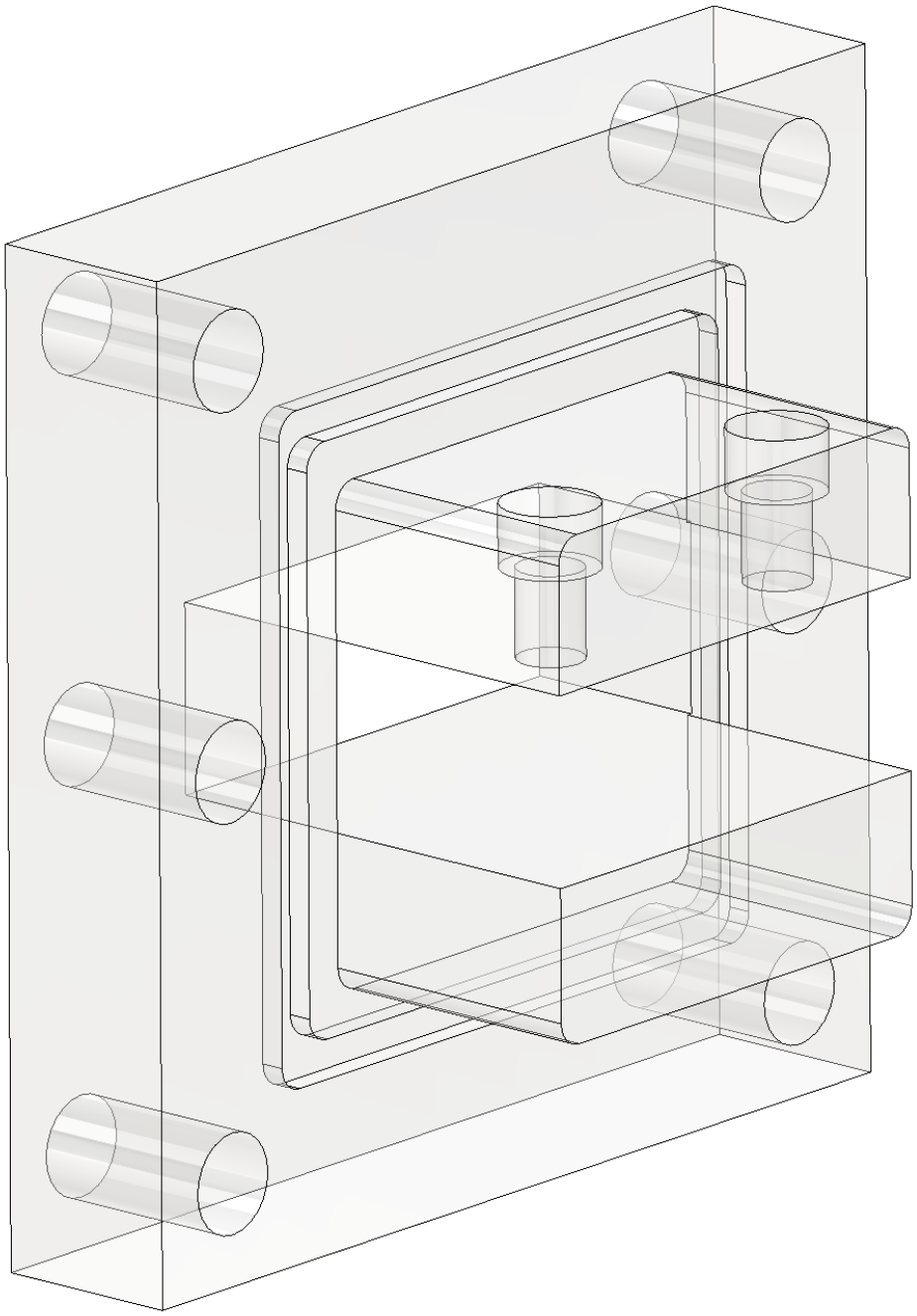

Figure 3.11: CAD model for injector flange

Although acrylic is easy to machine, the complexity of the flange's geometry necessitated outsourcing the fabrication to Xometry. Upon arrival, the flange was opaque from the machining process, as shown in Figure 3.12, requiring sanding and polishing to restore transparency for bubble observation. A hand sander was used starting at 120 grit and working up to 3000 grit. After this, the NOVUS 3-step plastic polishing kit was used to get a transparent finish to the acrylic. The polished flange is shown in Figure 3.13.

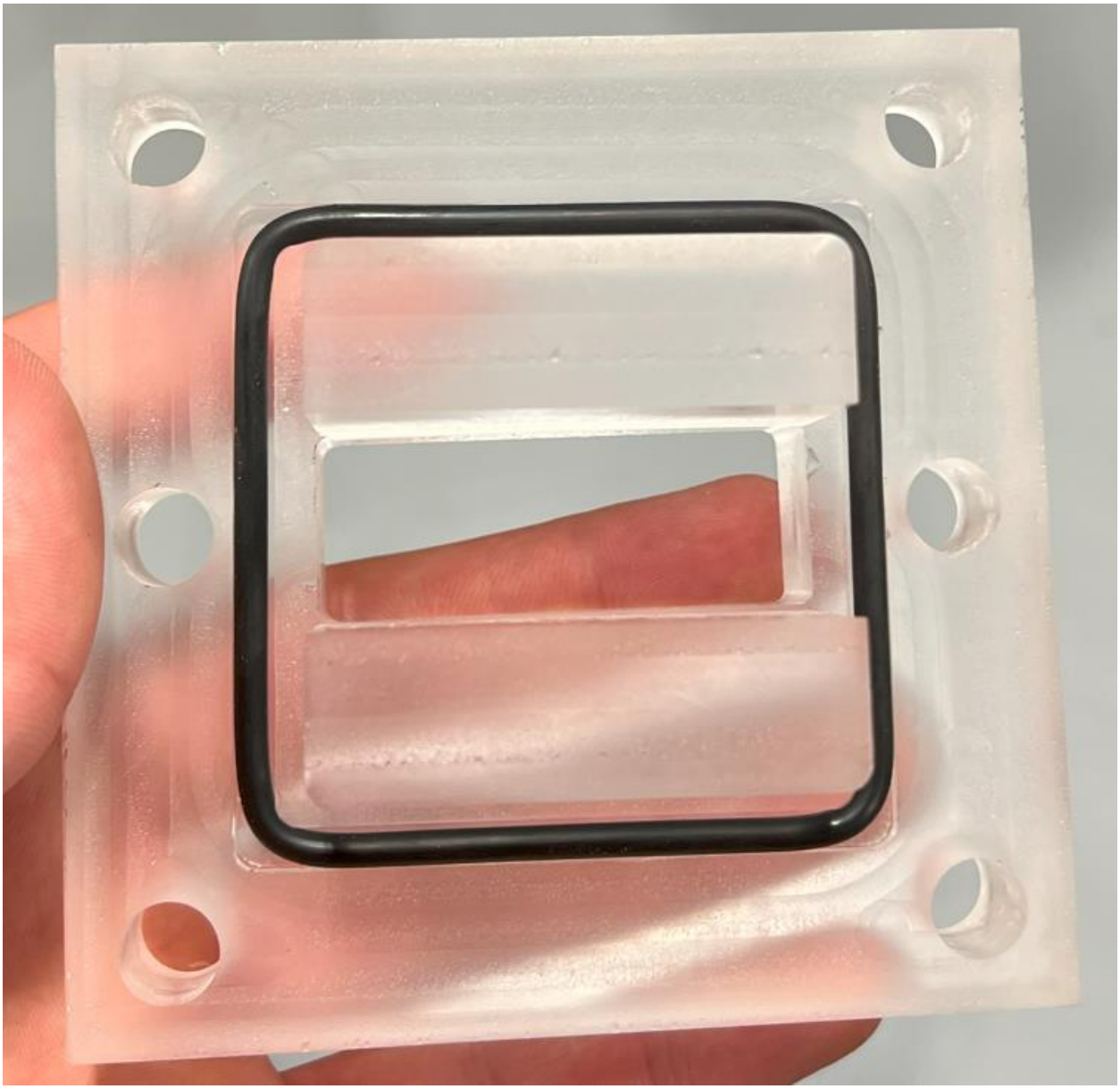

Figure 3.12: Unpolished flange

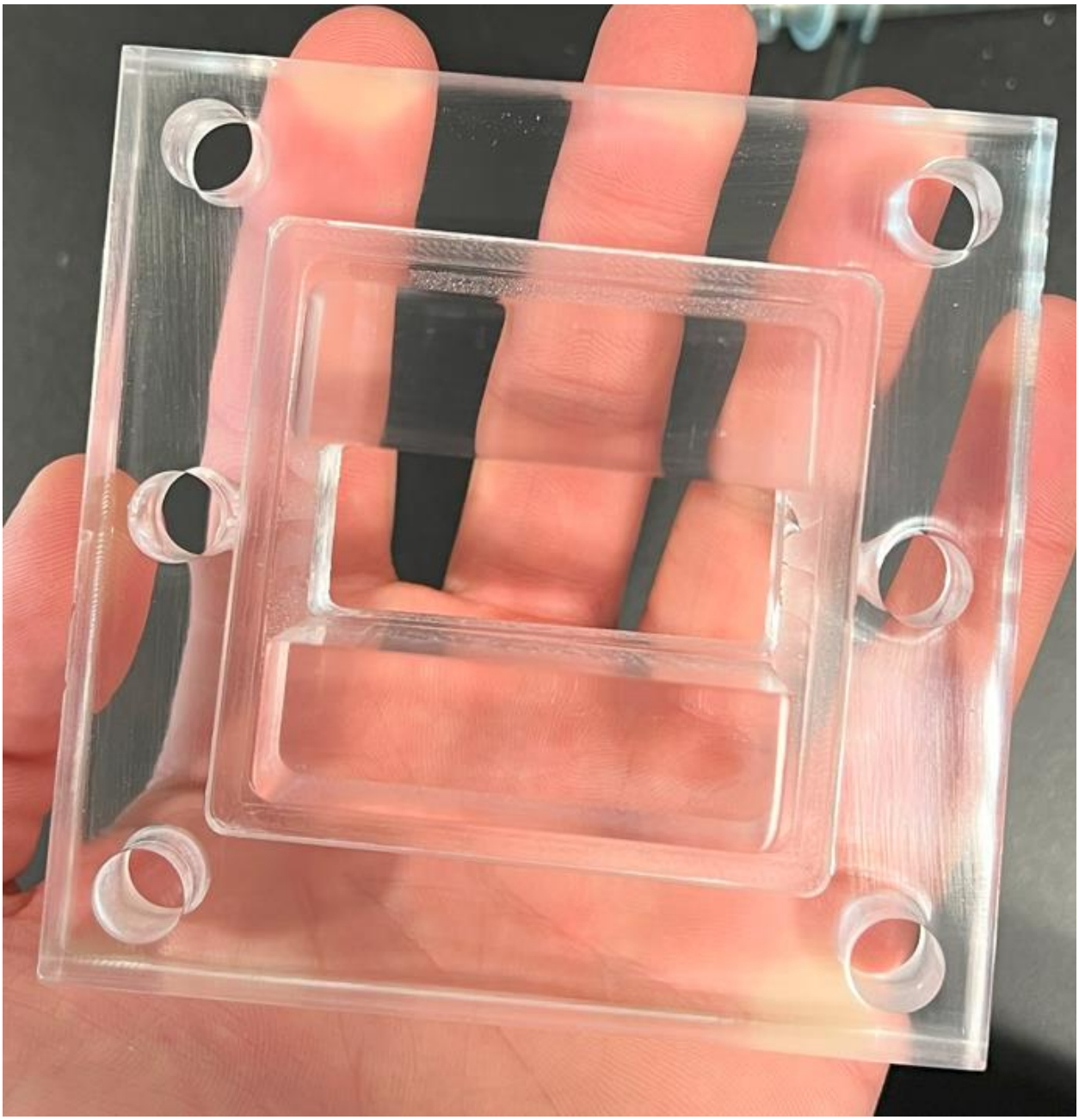

Figure 3.13: Polished flange

The injector fits into the rectangular slot, as seen in Figure 3.14 and Figure 3.15. The fasteners that apply pressure to the injector's outlet fit into the vertical holes in the flange, which

were drilled after the flange was received due to a design change. The injector assembly's square boss fits into a corresponding square hole in the test section. To ensure proper connection, the socket screw heads at the injector's outlet were recessed within the square boss. Silicone caulk was applied where the injector sandwich meets the flange to prevent leaks.

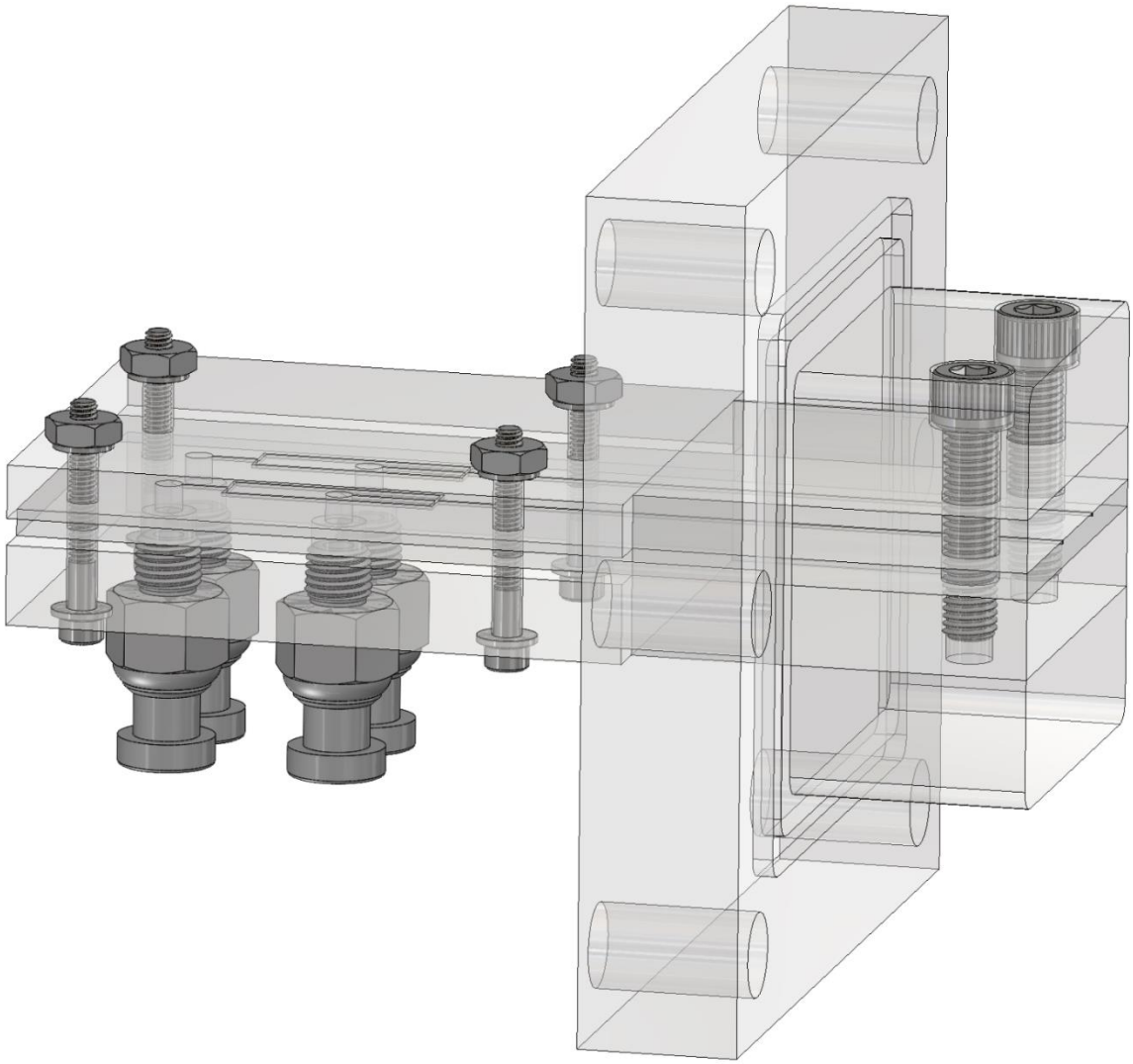

Figure 3.14: CAD model of the complete injector assembly

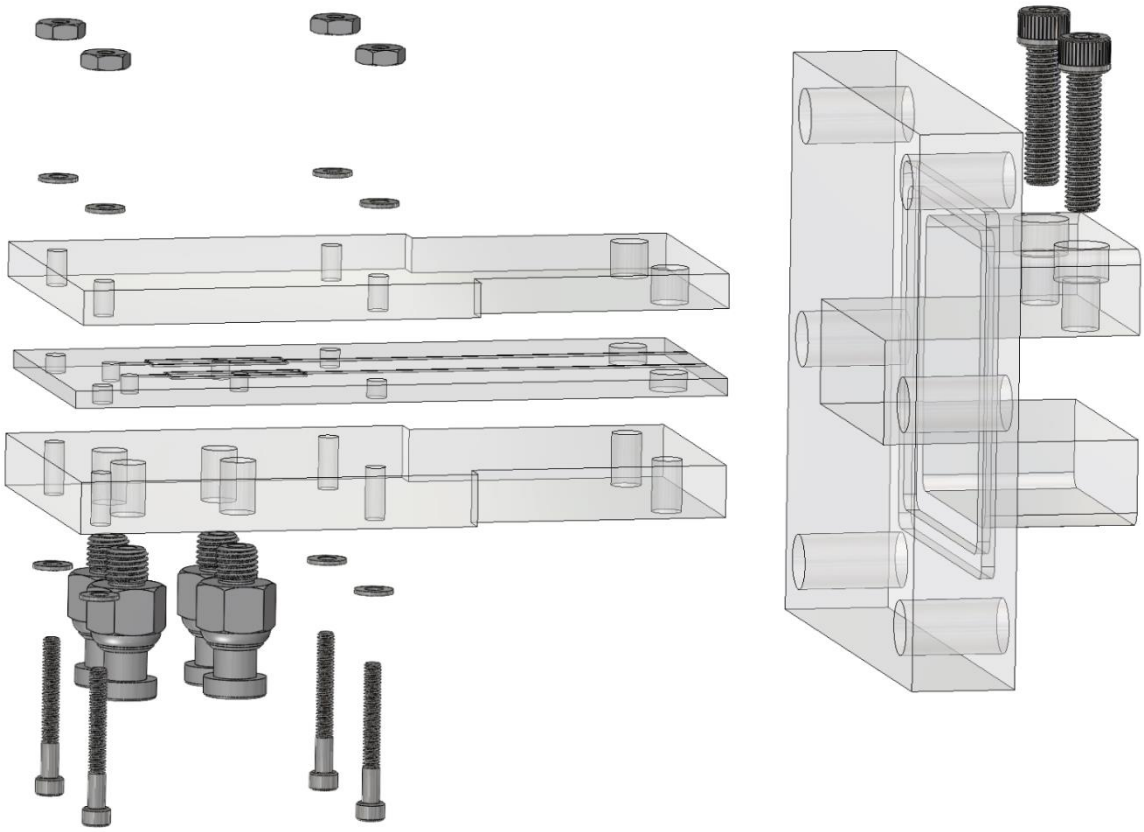

Figure 3.15: Exploded view of the complete injector assembly

As shown in Figure 3.12, an O-ring is embedded in the flange. For a proper seal when fastening the injector assembly to the test section, the O-ring must be compressed. During initial testing, it was discovered that the square boss was too long, preventing a proper seal. The box was subsequently sanded down to achieve a better fit. The completed injector assembly, prior to applying silicone caulk, is shown in Figure 3.16.

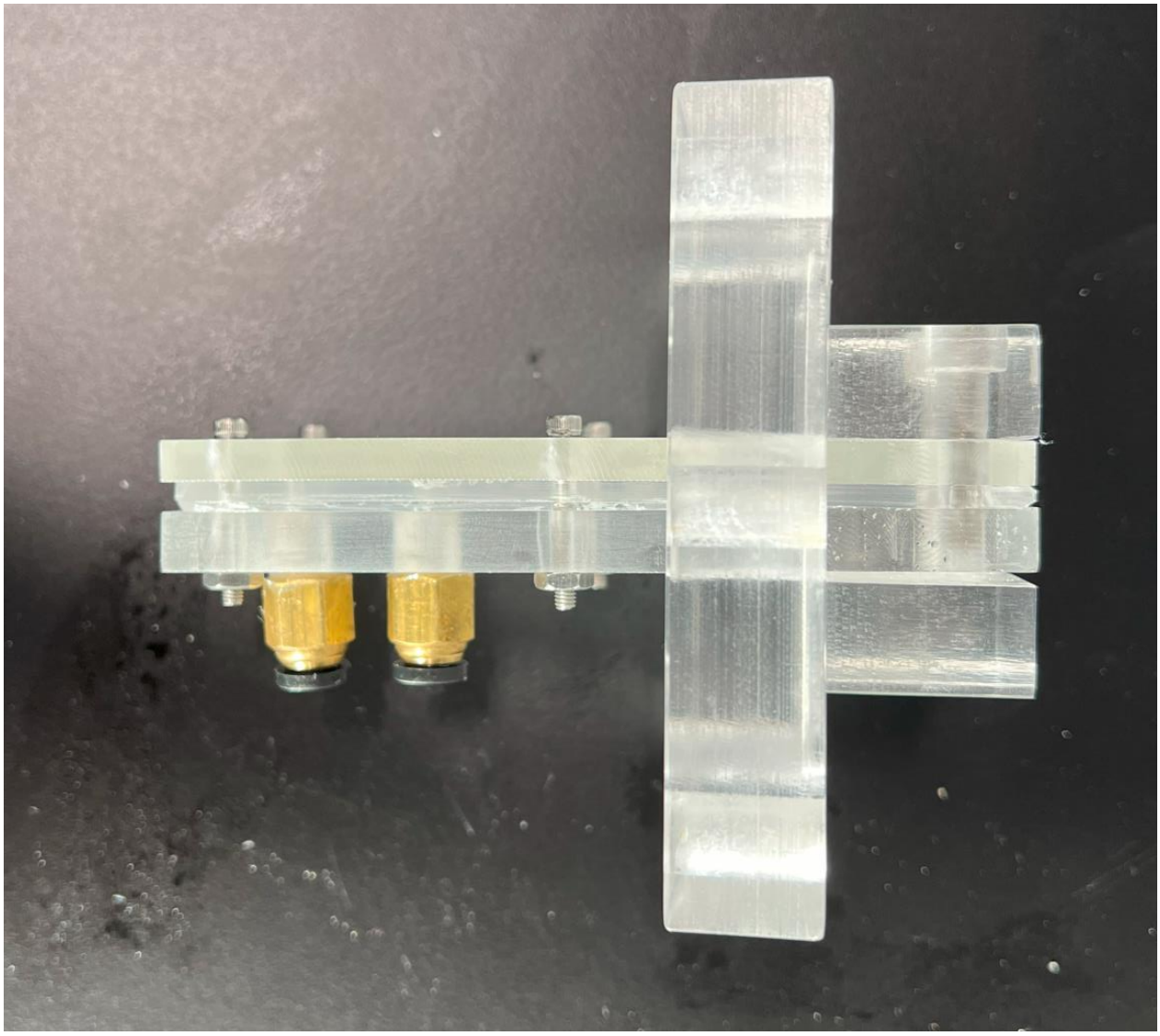

Figure 3.16: Picture of complete injector assembly

3.3. Injection

In this study, a consistent method for injecting air and the surrogate fluid at a controlled rate is essential. Due to the small width of the microchannels, the required injection rate is quite low, ranging from 30 mL/hr to 140 mL/hr. To achieve constant and highly accurate flow rates with minimal variability, syringe pumps are employed. Syringe pumps operate by driving the plunger of a syringe at a precisely controlled and adjustable rate, delivering the exact volume of fluid needed. This study utilizes two syringe pumps—one for each injected substance—for flow control. The specific pump used is the NE-300 InfusionONE Syringe Pump, as shown in Figure 3.17.

Figure 3.17: NE-300 InfusionONE Syringe Pump

The NE-300 Syringe Pump offers a wide flow rate range, from as low as 12.2 nL/min to 20.95 mL/min, depending on the syringe size. Since the study requires long-duration tests, the largest compatible syringes were chosen: 100 mL capacity luer lock tip syringes for both air and the surrogate fluid. The pump allows for the internal diameter of the syringe to be entered into the settings to ensure the correct flow rate is maintained. The accuracy of the injection rate of this syringe pump is +/- 1%.

As mentioned in Section 3.2, 1/8" interior and 1/4" exterior diameter flexible PVC tubing was used to transport the air and surrogate fluid to the injector. A luer lock-to-1/8" inner diameter tube adapter was used to connect the syringe to the tubing. For air injection, since the pressure can vary between tests, it is necessary to monitor the air pressure exiting the syringe to determine the mass flow rate. A simple pressure gauge was installed for this purpose. The pressure gauge used ranges from 0 psig to 30 psig with graduations every 0.5 psi. The injection setup is shown in Figure 3.18.

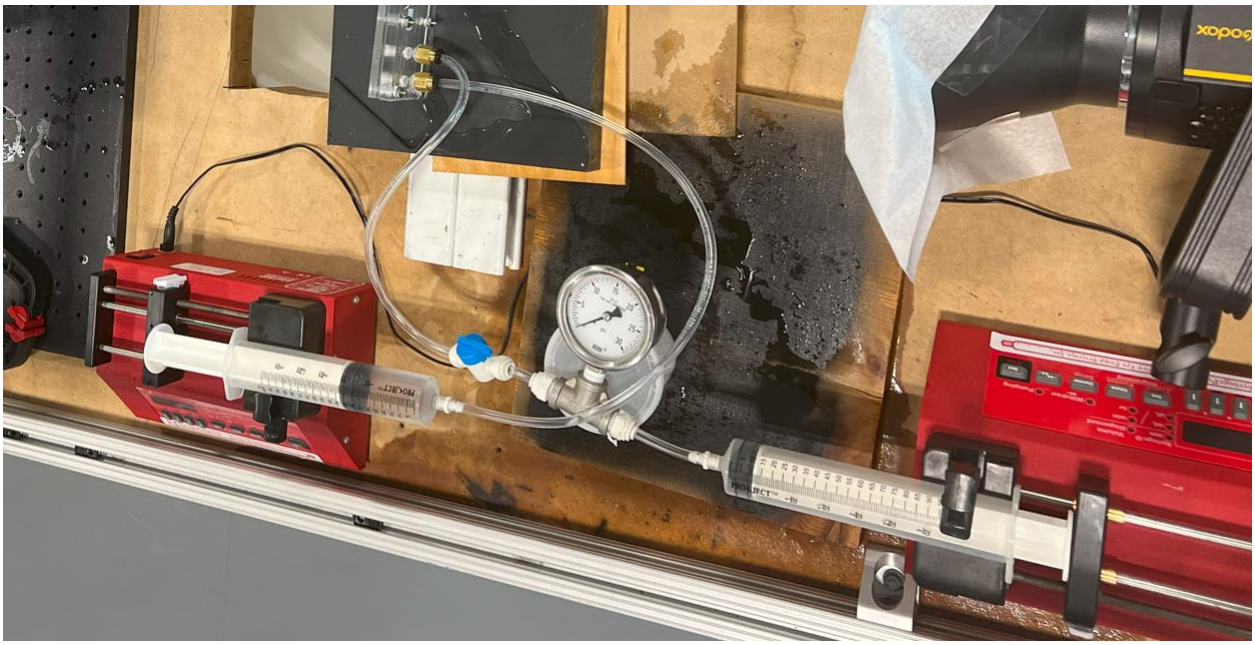

Figure 3.18: Injection setup

3.4. Test Section Loop

As mentioned in Section 3.1, the injector is designed to fit into a test loop with a cross-section of 3 cm by 1 cm. Much of the test loop was designed and fabricated in Song (2018), and only minor modifications and assembly were required for the tests in this study. Additionally, a few major components of the test loop needed to be replaced. The injector fits into the test section as shown in Figure 3.19. When fastening the injector assembly to the test section, as noted in Section 3.3, the O-ring must be compressed to ensure a proper seal. This is accomplished with the fasteners shown in Figure 3.19.

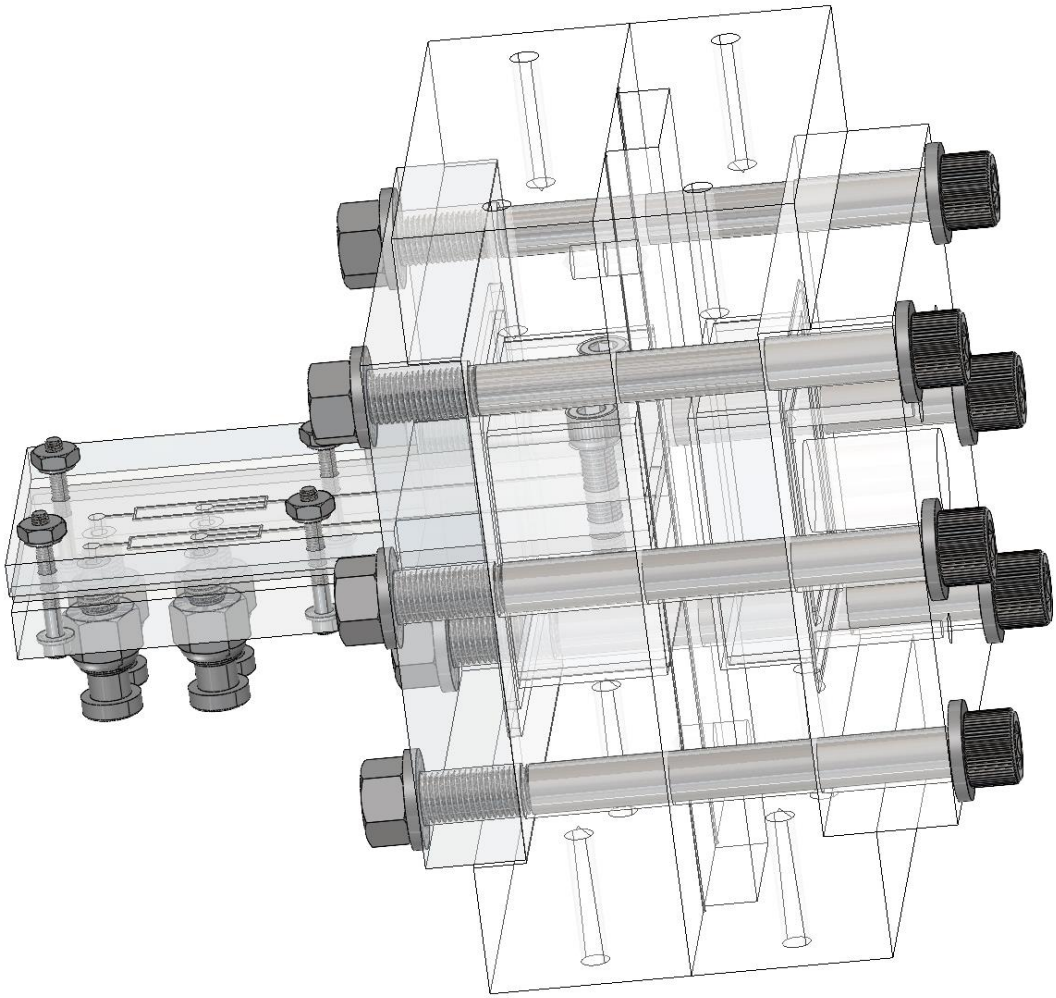

Figure 3.19: CAD model of the injector assembly fitting into the test section.

The test loop structure consists of two major support frames, both anchored to the concrete floor. As seen in Figure 3.20, the first structure is an aluminum frame supporting the test section and flow meters, which are discussed later. The second structure supports the tank and circulation

pump. The tank, with a capacity of 15 gallons, holds the glycerin-water mixture and feeds it directly into the circulation pump.

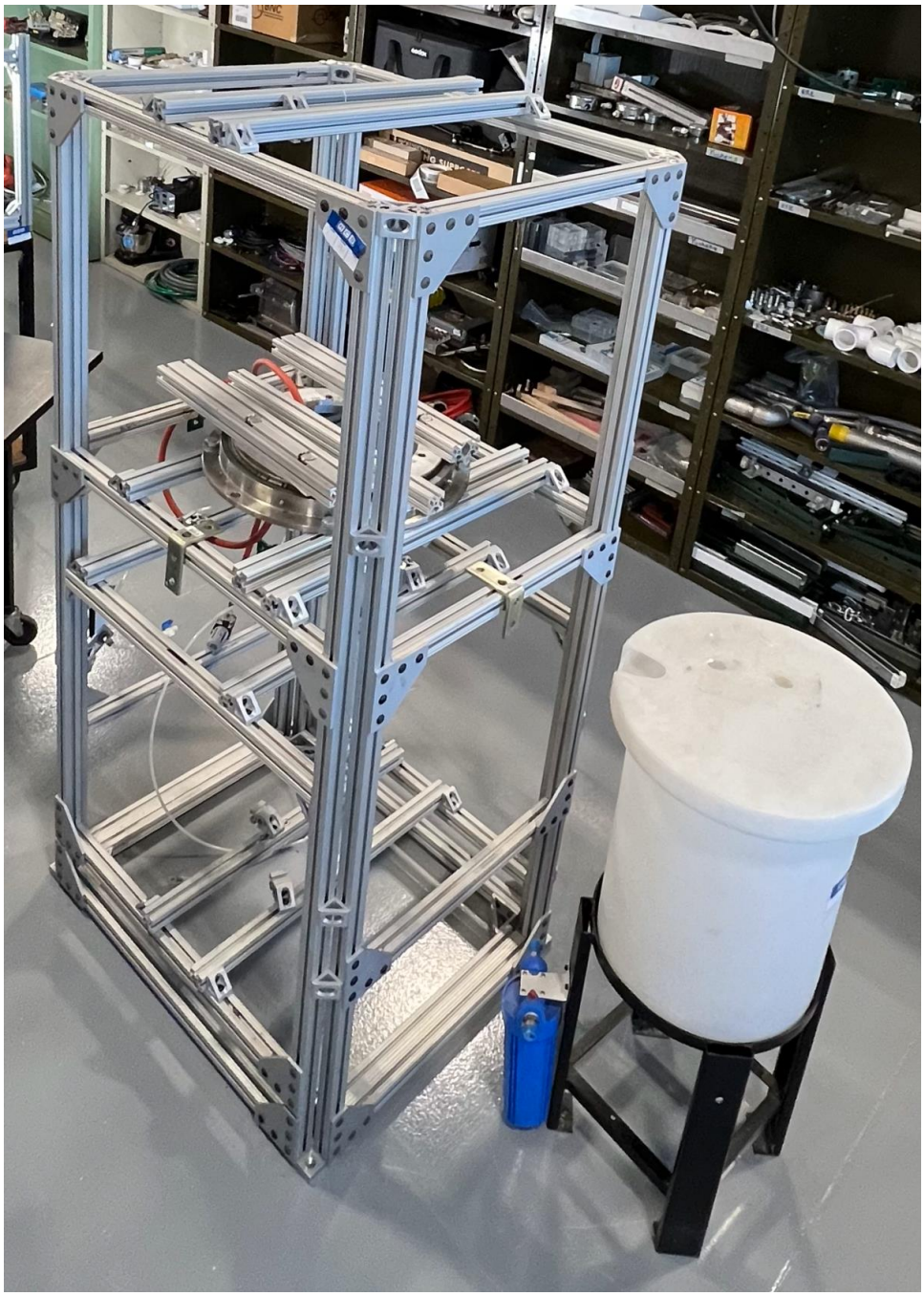

Figure 3.20: Test loop structure and tank

The tank is connected to the circulation pump via PEX tubing. The circulation pump used in this study is a 1.5-horsepower model, secured beneath the tank on the left side of Figure 3.20, as shown in Figure 3.21. While Song (2018) utilized a 1-horsepower pump, the increased viscosity and density of the surrogate fluid in this study necessitated the use of a more powerful pump to achieve comparable flow rates.

Figure 3.21: Circulation pump fastened to the tank structure

The outlet of the pump feeds into a PEX tubing system, shown in Figure 3.22, which directs flow to one of two volumetric flow meters using two valves. To ensure proper circulation when the pump is running, one valve must remain open. To obtain accurate flow readings, the other valve is closed. When the left valve is open and the right is closed, flow is directed to a flow meter ranging from 0 to 1 gallon per minute. When the right valve is open and the left closed, flow is directed to a flow meter ranging from 0 to 7 gallons per minute.

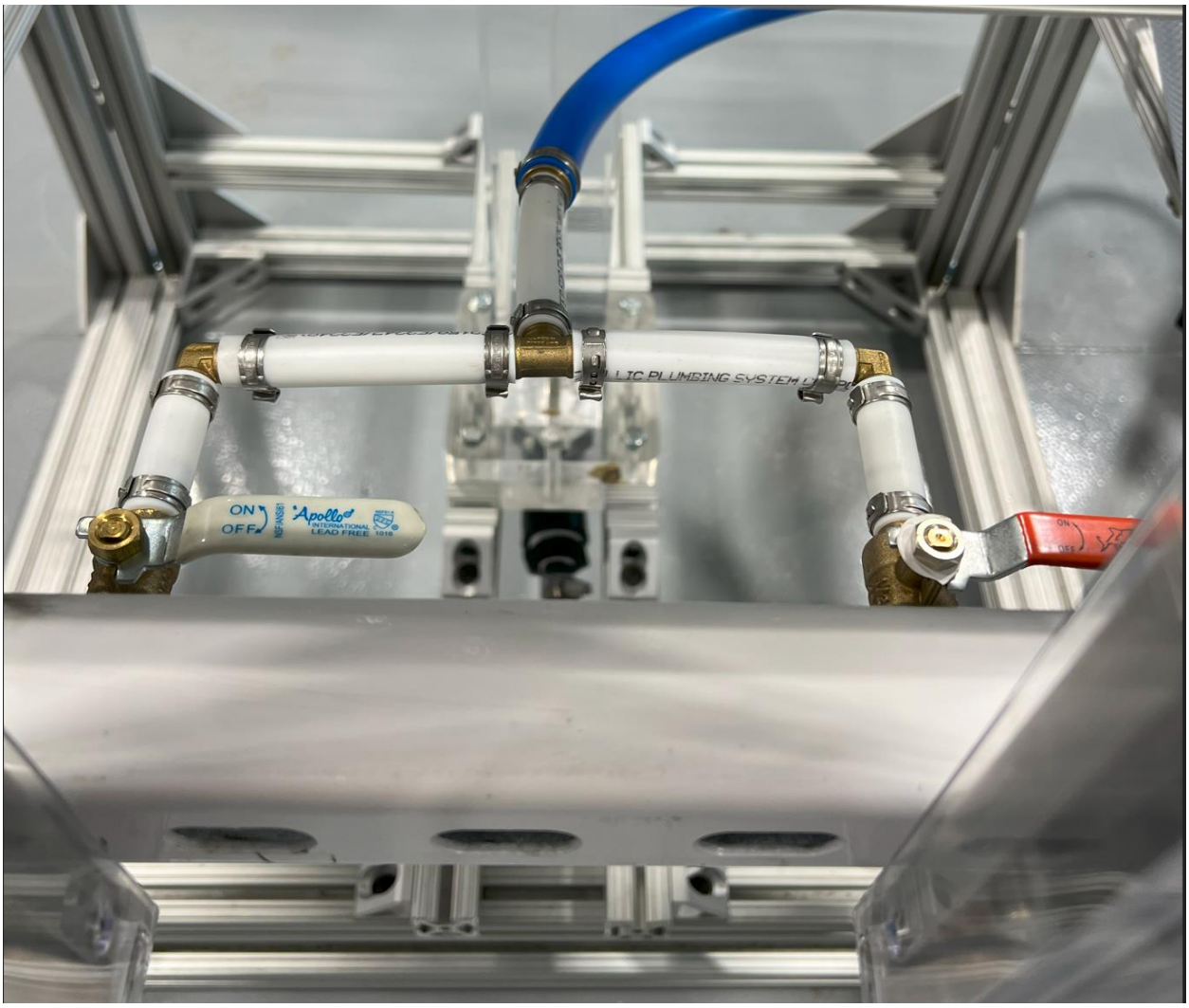

Figure 3.22: Flow directing device for flow meters

The tests in this study did not require the smaller flow meter; instead, the larger flow meter was used to measure the flow rate of the surrogate fluid through the test section. As shown in Figure 3.23, this flow meter reads in gallons per minute of water. The reading is based on the drag force exerted on a mass within the meter by the fluid, calibrated for the density of water. To

calculate the actual flow rate for the glycerin-water mixture, the following correction is applied:

$$Q_{actual} = Q_{reading}\sqrt{\frac{\rho_w}{\rho_{gw}}}, \tag{21}$$

where Q_{actual} is the corrected flow rate through the flow meter, $Q_{reading}$ is the flow meter reading, ρ_w is the density of water, and ρ_{gw} is the density of the glycerin-water mixture.

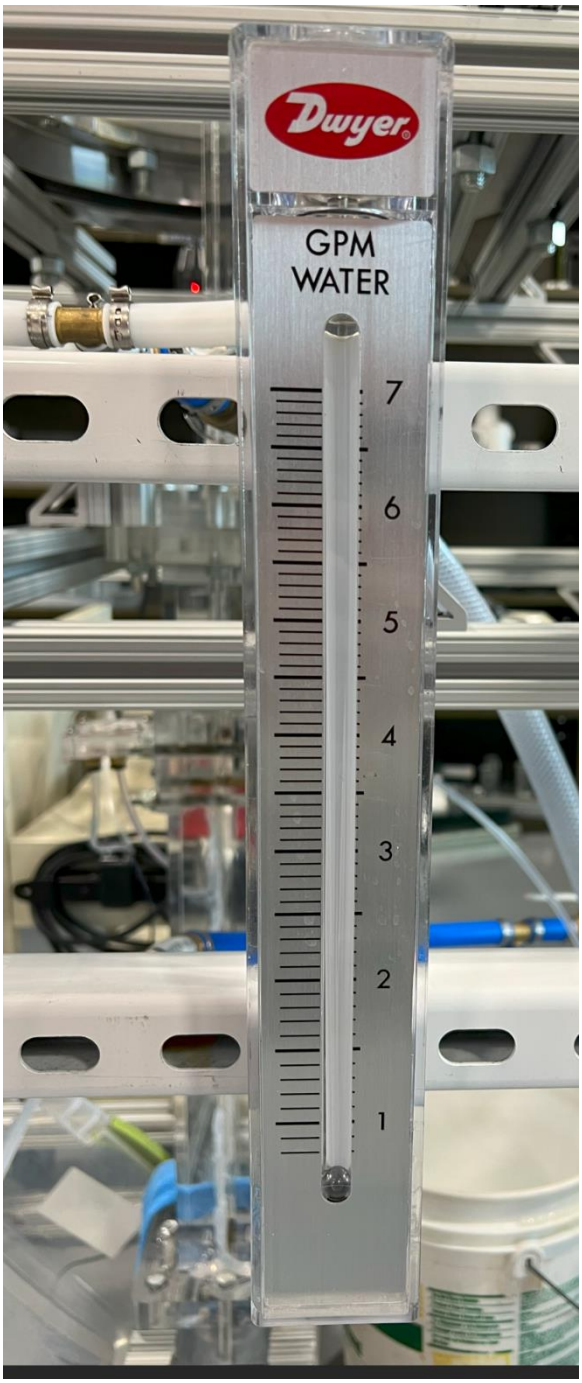

Figure 3.23: Flow meter used for tests inside loop

The outlets of the two flow meters converge into a single flow path, as shown in Figure 3.24. This flow then passes through a valve that allows for the adjustment of the flow rate. When fully open, the flow is at its maximum; when fully closed, the flow is stopped entirely. Flow control is important because at maximum capacity, the pump introduces small bubbles into the system, disrupting data collection.

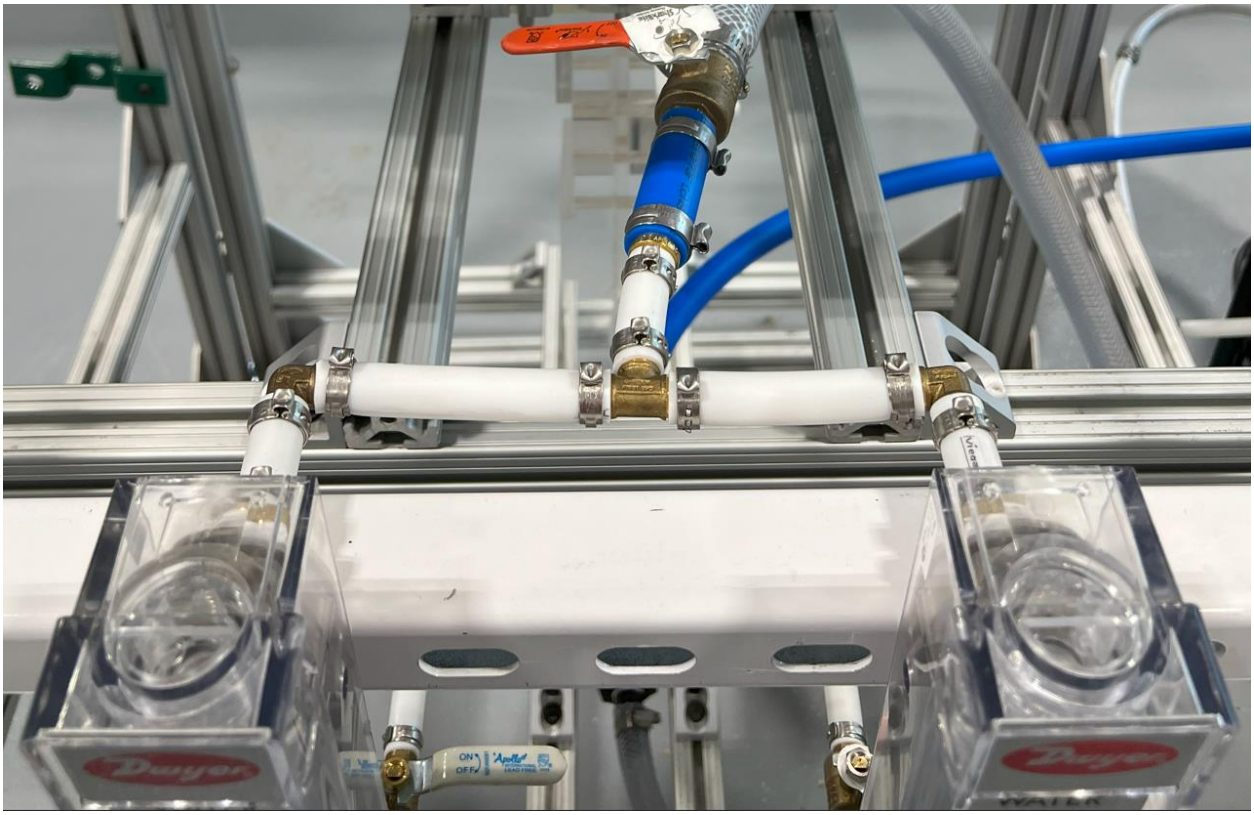

Figure 3.24: T-joint uniting flow from both flow meters.

Two drains are installed in the test loop to facilitate fluid changes or purging of the test section, as shown in Figure 3.25 and Figure 3.26. The first drain is located between the tank outlet

and the pump inlet to empty the tank, while the second drain is located between the pump outlet and the flow meter inlets. Both drains operate using gravity.

Figure 3.25: Drain for emptying the tank

Figure 3.26: Drain for emptying the test section

Once the test loop was fully assembled, it was tested with water to check for leaks and

ensure proper operation. Any leaks were sealed with superglue or silicone caulk. Issues with the injector were mostly resolved by adjusting the tightness of the fasteners. Once these adjustments were made, the loop was ready for testing.

Chapter 4

4. Injector Testing

4.1. Outside Loop Experimental Setup and Procedure

Before assembling the acrylic-PDMS sandwich to the flange, it was important to fully understand the function of the microfluidic flow-focusing device used in the injector. Measuring the size of the bubbles produced by the device before they are injected is the most effective way to ensure that the microchannels are functioning properly. This method evaluates the device's performance before introducing uncertainties. Setting up the test correctly is crucial to obtaining accurate results.

Since the tests conducted outside the loop required only small volumes of the surrogate fluid, small batches of the mixture were prepared at a time. The surrogate fluid was created by measuring the glycerin and water by volume using the injection syringe. The volume ratio of glycerin in the surrogate fluid was set at 0.3. To prepare the mixture, 100 mL of glycerin was drawn into the syringe from a 5-gallon bucket using a short section of the injection tubing and then transferred to a sealable bottle. Next, 233 mL of water was measured with the syringe and added to the bottle. The bottle was shaken to ensure proper mixing and homogenization. This process also aerates the mixture, so before testing, air bubbles were removed by creating a vacuum in the syringe—blocking the outlet and pulling back on the plunger to allow air to escape from the

solution.

The test setup for the outside loop tests, shown in Figure 4.1, was simple but effective. The syringe pumps were placed on the left side of the testing table, with the injector standing upright in the middle, its outlet pointing to the right. A camera was positioned at the far end of the table, pointed toward the injector, with a light on the opposite side of the camera directed at the injector. The camera was connected to a computer (not shown in the picture) for control, and the brightness of the light was adjustable using the control board on the right side of Figure 4.1.

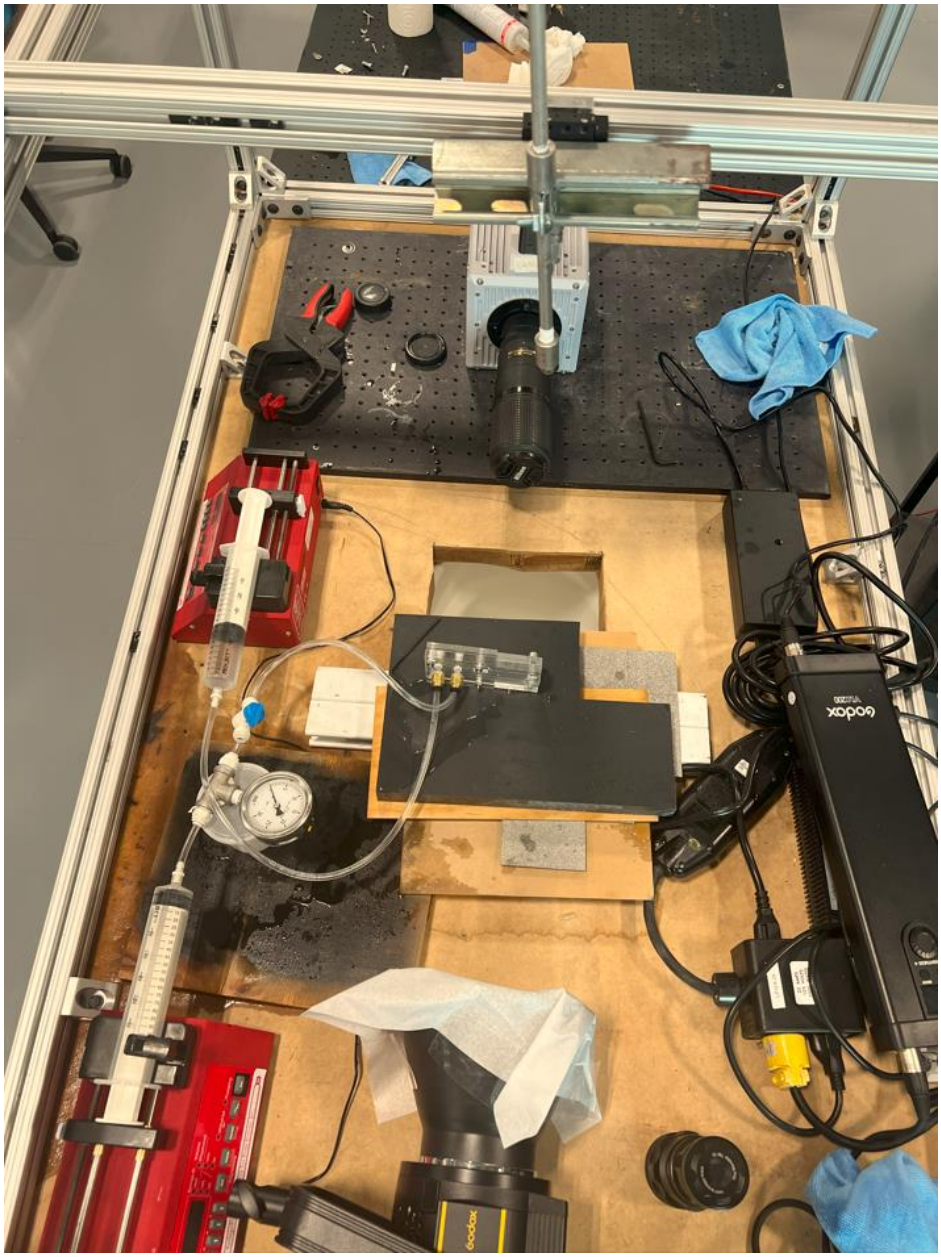

Figure 4.1: Test setup for outside loop tests

The testing procedure was as important as the setup to ensure high-quality results. A total of 96 conditions were tested, each with five trials, resulting in 480 tests overall. Each test captured 200 images at a frame rate of 3000 frames per second and a shutter speed of 1/4000 of a second.

The test matrix consisted of 12 different injection rates for the surrogate fluid, each paired with one of eight air injection rates. These injection rates are detailed in Table 4.1. The gas injection rates initially appear peculiar. This is because it was discovered after the tests were conducted that the interior diameter of the syringe was set to 27.3 mm when it should have been 31.75 mm. To correct for this mistake in the interest of proper processing, the indicated injection rate was corrected with:

$$Q_{actual} = Q_{indicated}\left(\frac{D_{actual}}{D_{set}}\right)^2, \tag{22}$$

where Q_{actual} represents the corrected injection rate, $Q_{indicated}$ represents the indicated injection rate, D_{actual} is the actual diameter of the syringe used, and D_{set} is the diameter that the syringe pump was set to.

Table 4.1: Injection volumetric flow rates

Glycerin-Water Mixture Injection Rate (mL/hr)	50, 55, 60, 65, 70, 75, 80, 85, 95, 105, 115, 125
Gas Injection Rate (mL/hr)	54.10, 60.87, 67.63, 74.39, 81.16, 87.92, 94.68, 101.44

To initiate flow in the injector, the fluid injection was started first, followed by the air injection. Since the air syringe typically begins at atmospheric pressure, fluid from the injector would rise into the air inlet. At this point, manual adjustment of the syringe pump was needed to increase pressure until the fluid was forced out of the system. Once the pressure equalized, steady-state flow was achieved, and data collection could begin.

Data collection began with recording the injector's temperature using an infrared

thermometer, which was used to determine the air mass flow rate. Next, the pressure was recorded from a gauge, and 200 images were captured and saved to a hard drive. There was a 15-second interval between each trial to ensure system stability. Once five trials were completed for a given condition, the flow condition was adjusted, and the process was repeated.

To determine the pixel-to-millimeter conversion for the images, a calibration sheet with 1 mm squares was used as a reference. By counting the number of pixels per square in the images, the pixel-to-mm conversion factor was calculated.

4.2. Image Processing Outside Loop

Once the raw data is acquired, it must be processed to extract useful information. While images are typically qualitative data, when converted to grayscale, they essentially become matrices in which each element corresponds to the brightess of a pixel. This transformation allows for the application of matrix operations to extract quantitative properties from the images. MATLAB, known for its strength in matrix operations, was used for this image processing.

An example of a raw image from the tests is shown in Figure 4.2. It is a grayscale image containing unnecessary space, with the bubbles in the microchannel being the focus for analysis.

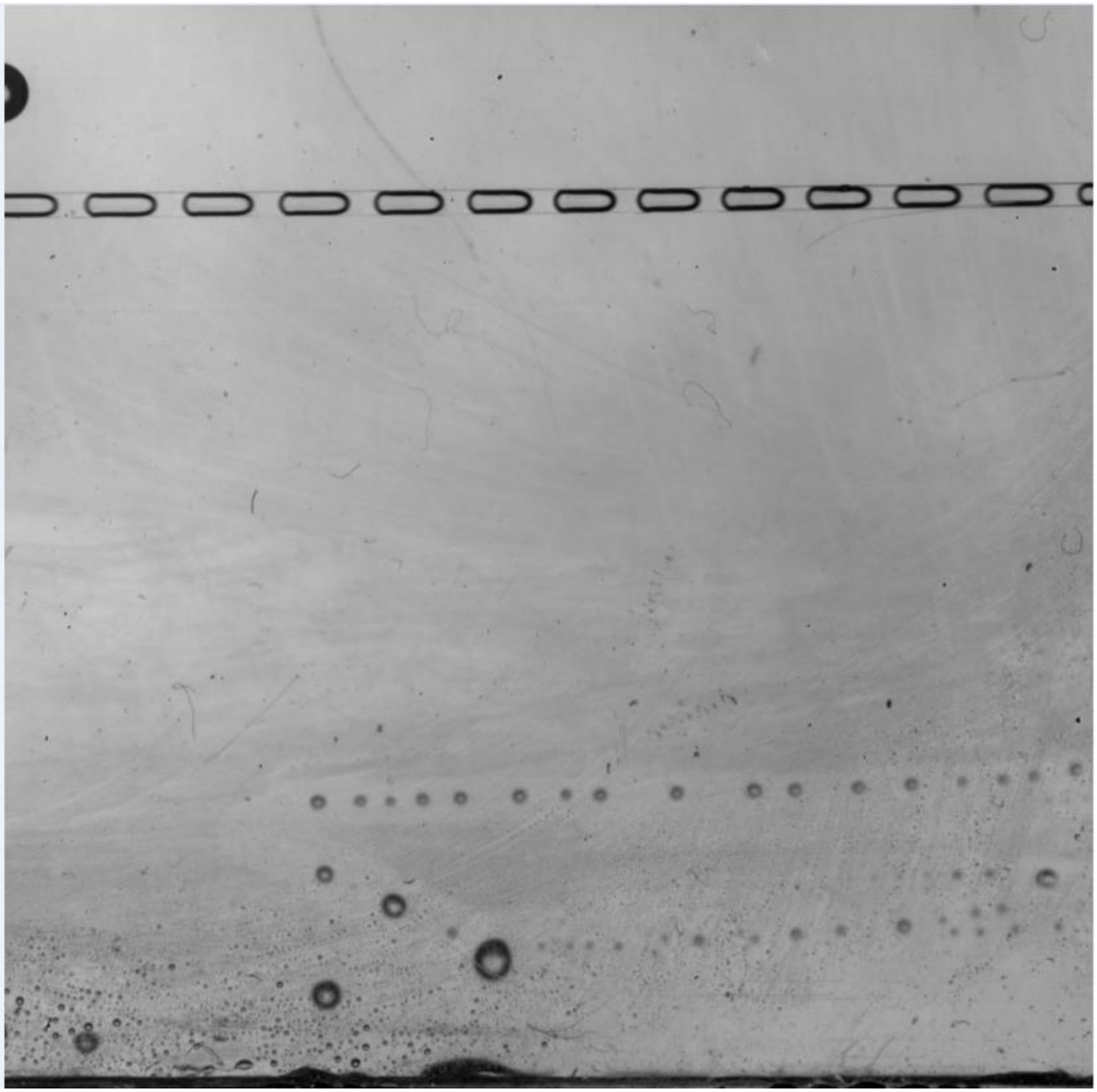

Figure 4.2: Example of raw image captured in outside loop testing

The first step in processing the image is to identify the region of interest and crop the image to focus solely on this area. The result of this cropping is shown in Figure 4.3.

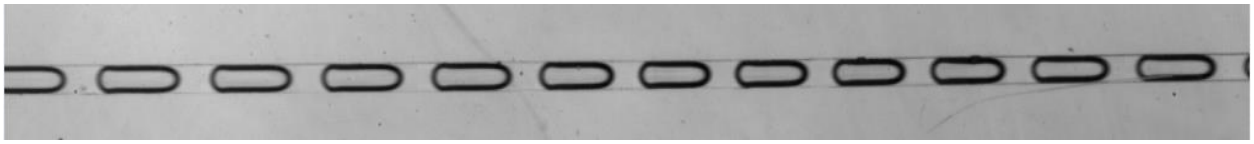

Figure 4.3: Cropped image of microfluidic region of interest

Next, the image is inverted, as shown in Figure 4.4. Since the bubbles we are analyzing appear as dark entities, inverting the image (by subtracting its matrix from one) makes the bubbles appear lighter, which is more convenient for subsequent processing.

Figure 4.4: Inverted image of microfluidic region of interest

The image is then saturated to increase the contrast of the image, so it is easier to identify the entities within the image. This is done with a built-in function in MATLAB called “imadjust” which evaluates the pixels within the image and converts the top 1% to value 1 and the bottom 1% to value 0. This makes the brightest pixels white and the darkest pixels black as displayed in Figure 4.5.

Figure 4.5: Saturated image of microfluidic region of interest

Small specks in the images, caused by imperfections in the injector, dust, or other debris, are removed using MATLAB's "medfilt2" function, which applies a median filter. This filter replaces each pixel with the median value from a surrounding neighborhood, smoothing the image as shown in Figure 4.6.

Figure 4.6: Mediad-filtered image of microfluidic region of interest

The image is then binarized so that the values in the image matrix are either 1 or 0 corresponding to white or black respectively. MATLAB has a built-in function for binarizing an image using a threshold defined with Otsu's method called "imbinarize" (Otsu, 1979). This binarizing function converts all the pixels above this threshold to 1 (white) and below the threshold to 0 (black). The example image after this process is displayed in Figure 4.7.

Figure 4.7: Binarized image of microfluidic region of interest

To ensure that the bubbles are treated as continuous masses, any gaps or holes within the bubbles are filled. This is done using the "imclose" function to close gaps and the "imfill" function to fill holes. The final processed image, used for calculations, is shown in Figure 4.8.

Figure 4.8: Final image used for calculations.

These image processing steps are computationally intensive, so the raw images were processed and saved separately, with a second code used to calculate the mass, volume, and frequency of bubble generation.

At the beginning of the code, variables for injection rates, temperature, and pressure readings for each trial are defined. The pixel-to-millimeter conversion factor is also specified. To ensure efficiency, matrix or vector variables are preallocated with the correct sizes, and a second region of interest similar to the one shown red in Figure is defined. All of the image conversion processes for the outside of the loop test were done with one MATLAB script (see Appendix A).

Figure 4.9: Second region of interest

MATLAB's "regionprops" function is used to extract properties of the bubbles, such as their bounding box and centroid. The bounding box helps determine the width of the bubbles, while the centroid is used to track their movement across frames.

The method of calculating the frequency of bubble generation in this study begins with counting the number of bubbles that exit the frame within each test. This is done by tracking where the centroid of the bubble closest to the exit is. In the first frame that doesn't include that bubble, the bubble closest to the exit is now the bubble behind that one, and thus the centroid of bubble closest to the exit in this frame is now farther from the exit. When this happens, the code adds 1 to the number of bubbles that have exited the frame.

With this, the average frequency of bubble generation can be calculated with:

$$\bar{f} = \frac{N_{exit}}{t_{test}}, \tag{23}$$

where N_{exit} represents the number of bubbles that exited the frame and t_{test} represents the total duration of the test given by:

$$t_{test} = \frac{N_{frames}}{framerate}, \tag{24}$$

where N_{frames} represents the number of frames in the test. It is important to note that $\bar{f}$ is not necessarily equal to the frequency of bubble generation at every point within the test.

It's important to ensure that the bubble generation frequency remains constant throughout the test. To validate this, the code sums the pixels within the second region of interest for each frame, storing these sums in a vector. As bubbles enter and exit the region, the values of the vector rise and fall. If the frequency is constant, the vector's plot should appear periodic, as shown in Figure 4.10.

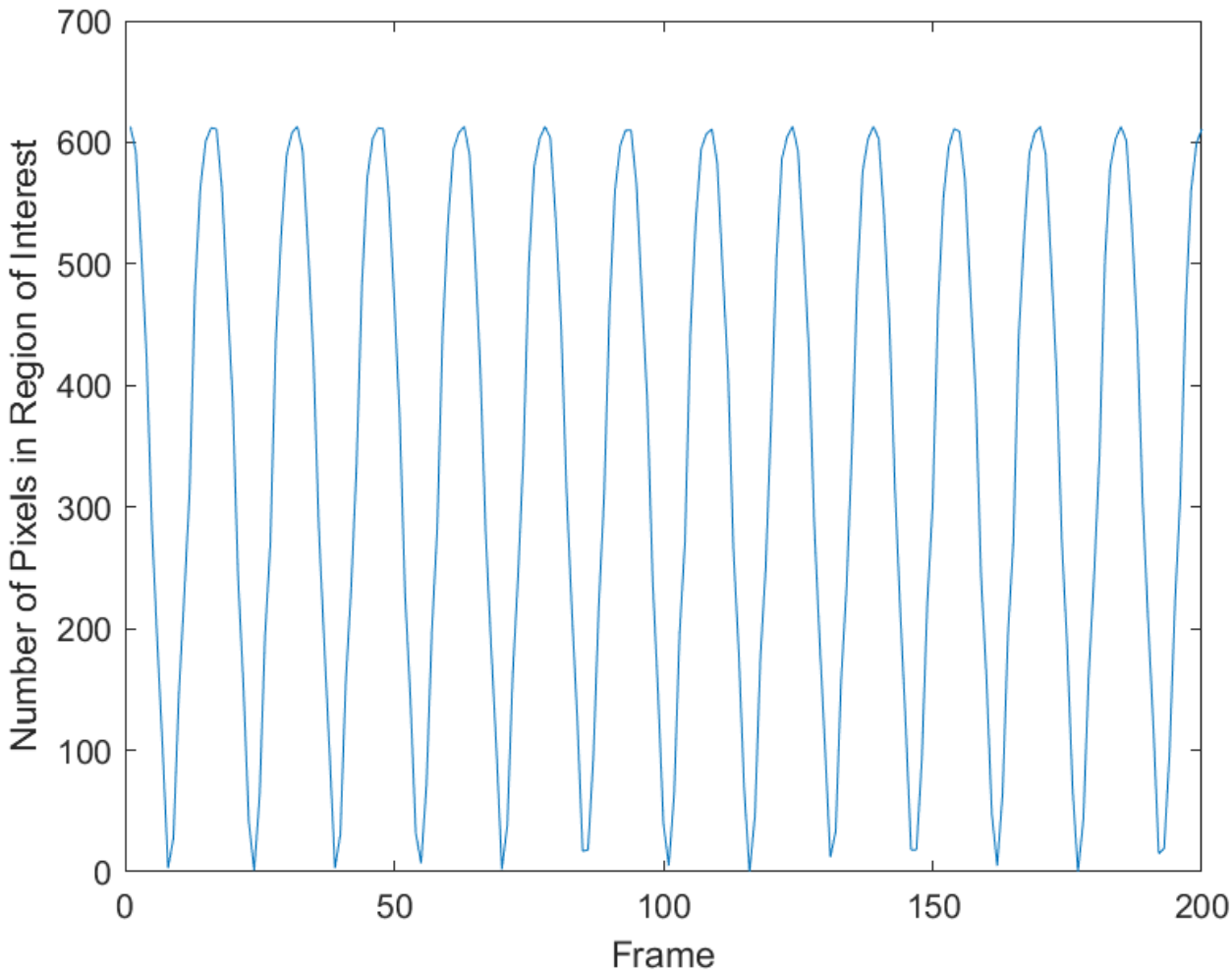

Figure 4.10: Plot of pixel count within the second region of interest

Fourier analysis is then performed on this vector to identify the dominant frequency. If there is one clear peak in the frequency domain, as shown in Figure 4.11, the bubble generation is periodic. If the data is nonperiodic, the frequency domain graph will look more like Figure 4.12, indicating potential issues with the injector, such as uneven pressure or debris in the microchannels.

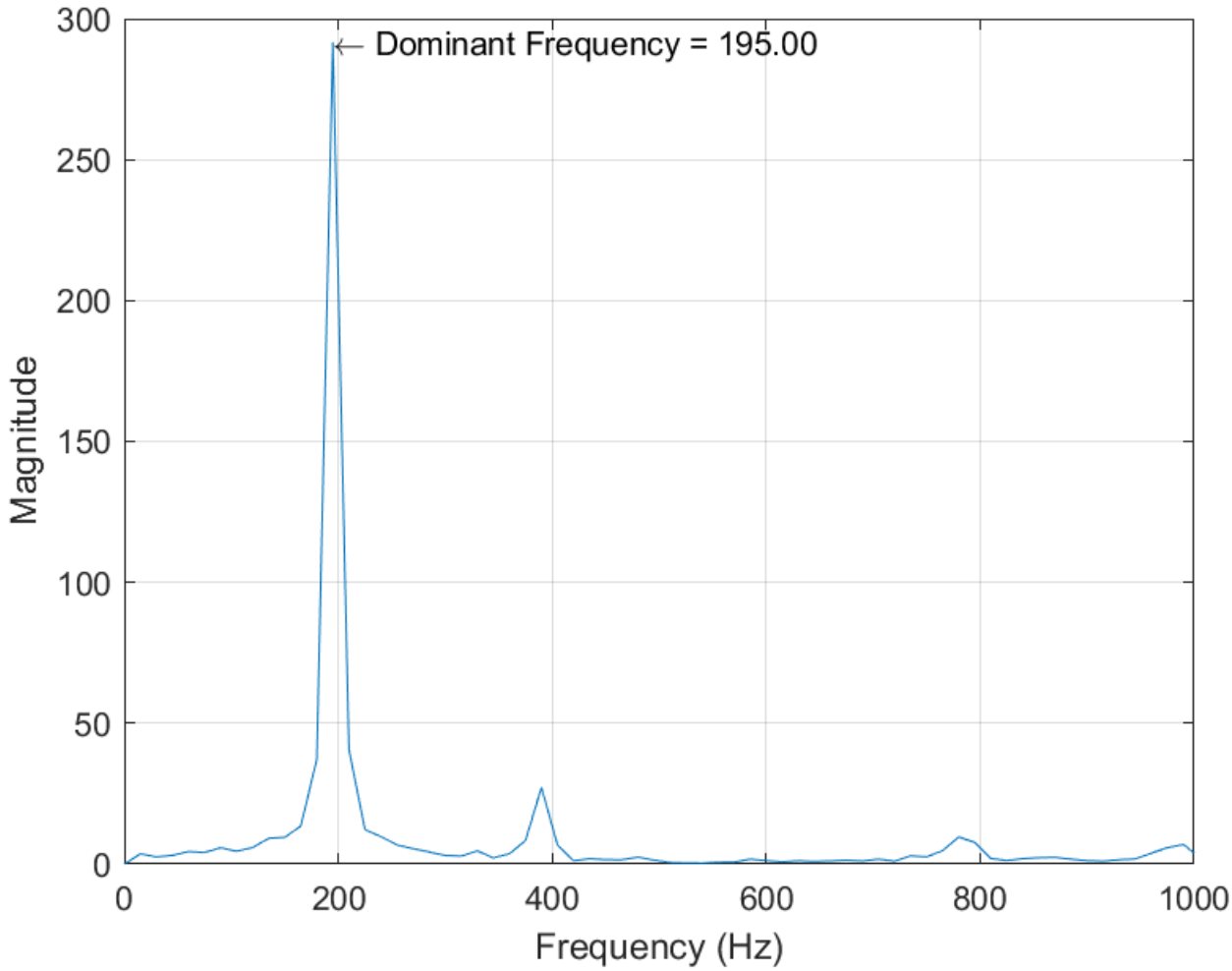

Figure 4.11: Frequency domain graph of periodic data

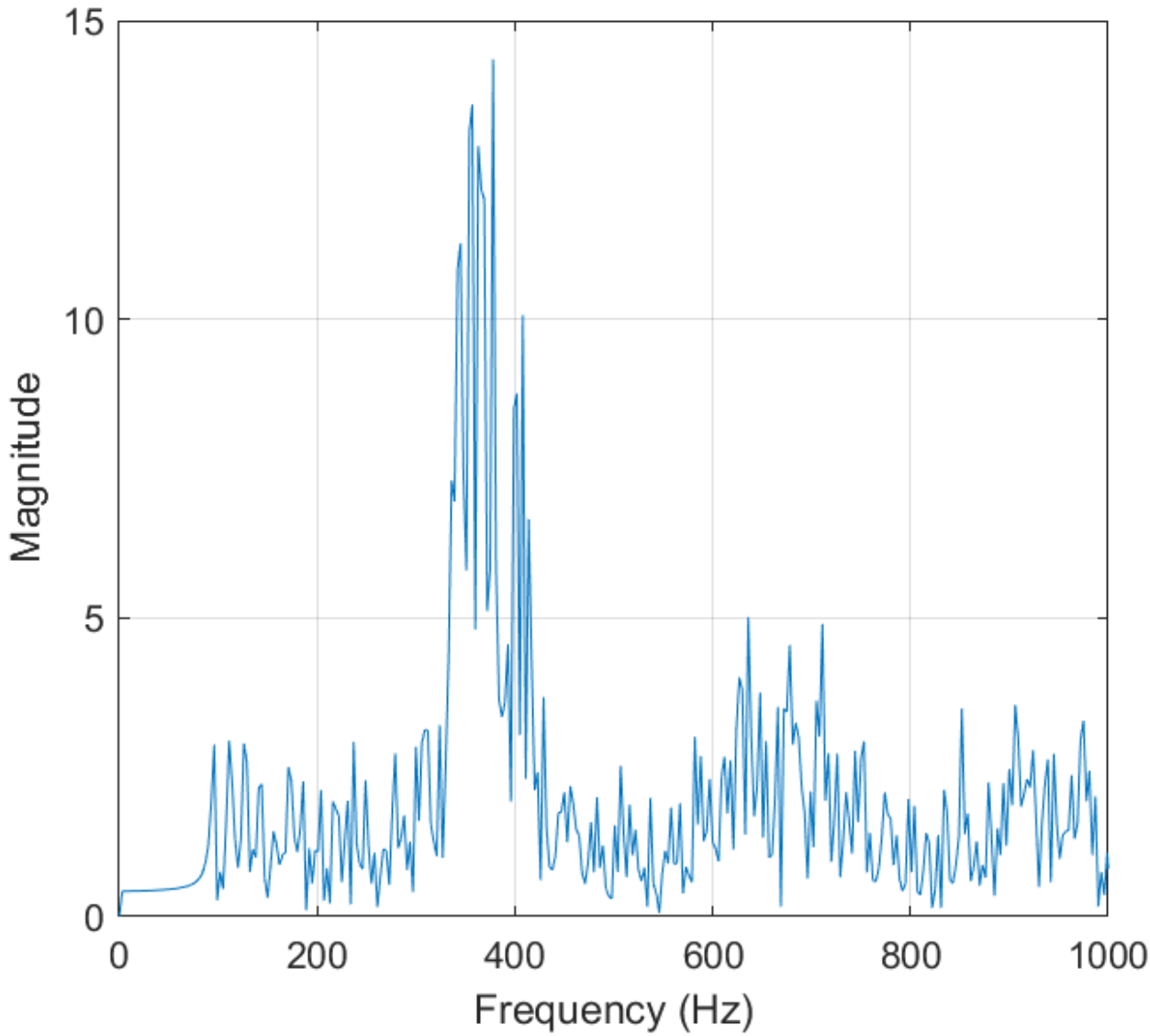

Figure 4.12: Frequency domain graph of nonperiodic data

To calculate the mass flow rate of the air injection, the ideal gas law is used:

$$\dot{m} = \frac{PQ_{air}}{R_{air}T}, \tag{25}$$

where P represents the absolute pressure of the air, Q_{air} represents the volumetric flow rate of the

air, R_{air} represents the gas constant for air, and T represents the absolute temperature. It is important to pay attention to the units in this equation and to use the proper value for R that is compatible with those units. Using the conservation of mass:

$$\dot{m}_1 = \dot{m}_2 \rightarrow \frac{P_1 Q_{air_1}}{T_1} = \frac{P_2 Q_{air_2}}{T_2}, \tag{26}$$

where the subscripts denote the conditions or positions of the gas. Knowing the bubble generation frequency, and the mass flow rate of a particular test, the average mass of the bubbles within that test can be calculated with

$$\bar{m} = \frac{\dot{m}}{f}, \tag{27}$$

where $\bar{m}$ represents the average mass of the bubbles.

In addition to confirming the assumption of constant frequency, it is important to assess the variability in bubble mass. This process begins by determining the volume of the bubbles in the captured images, assuming each bubble cross-section is circular. The top image in Figure 4.13 shows a close-up example of a bubble being analyzed in the microchannels. Each column in the image corresponds to a width of 1 pixel. To calculate the bubble's volume, the bubble is treated as a series of stacked cylinders. The diameter of each cylinder is determined by the number of pixels the bubble spans in each column, which is then converted to millimeters. The height of each cylinder is 1 pixel (also converted to millimeters), and by summing the volumes of these cylinders, the total volume of the bubble is obtained. The assumed 3-dimensional geometry of the bubble is shown in the bottom image of Figure 4.13

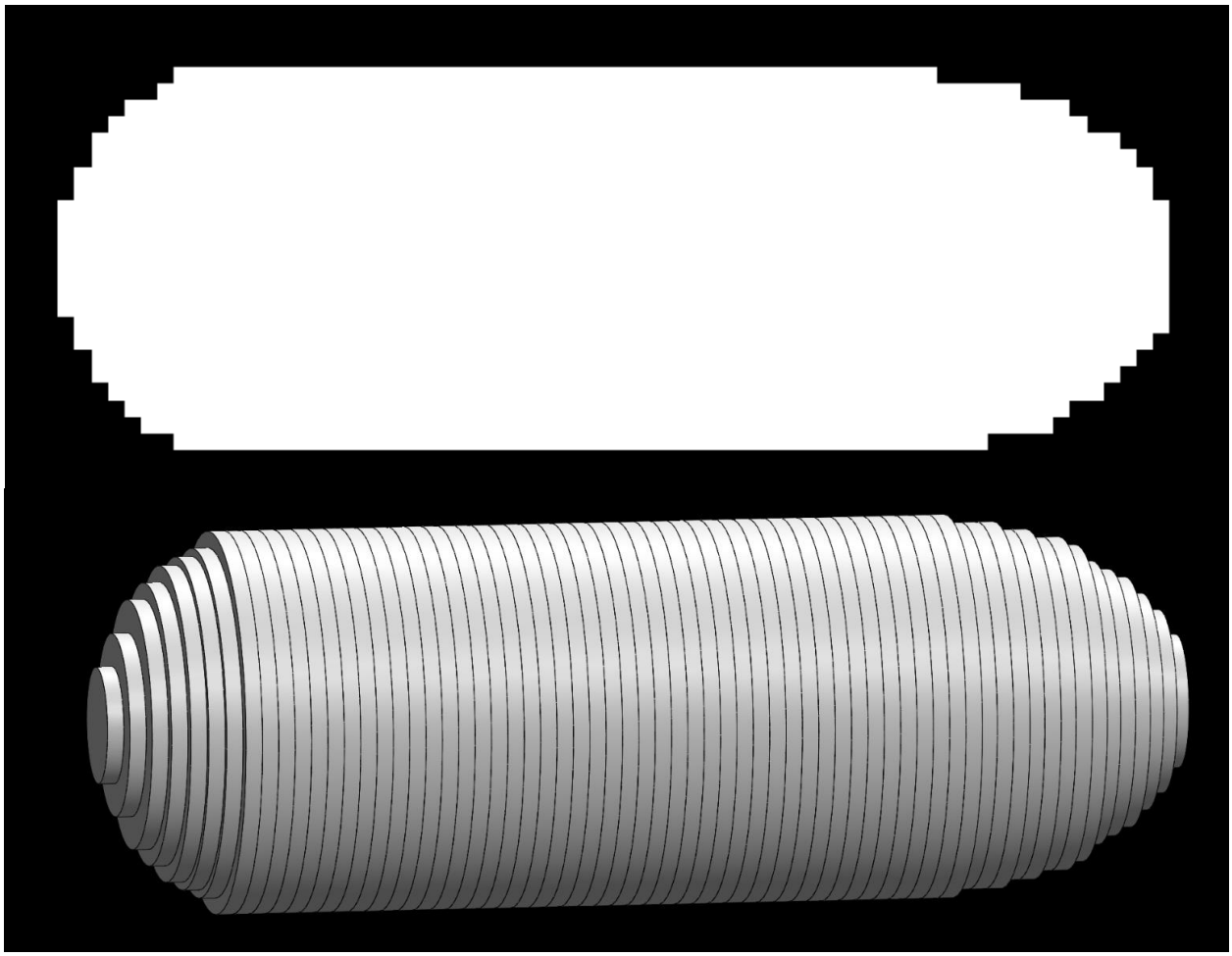

Figure 4.13: Close-up example of an individual bubble analyzed by the program.

Similar to Equation (*25*), the volume can be converted to mass with the ideal gas law:

$$m = \frac{PV}{R_{air}T}. \tag{28}$$

However, since pressure is not constant, it must be calculated for each bubble individually. This process begins by determining the velocity of each bubble in each frame. Assuming the bubble

moves strictly horizontally, the velocity is calculated by tracking the x-position of the bubble's centroid across frames. The velocity in each frame is then given by:

$$v_i = framerate * (x_{i+1} - x_i), \tag{29}$$

where x represents the x-position of the bubble's centroid and the subscript denotes the frame being analyzed. Since this formula cannot be applied to the last frame in which the bubble appears, it is assumed that the velocity in the last frame is the same as in the second-to-last frame.

The velocity is used to calculate the Reynolds number using Equation (*8*). Since the Reynolds number is less than 2000 in all tests, the flow is assumed to be laminar. Based on this assumption, the Darcy friction factor is calculated using:

$$f_D = \frac{64}{Re}. \tag{30}$$

This factor is then used to calculate the pressure drop along the flow path:

$$\Delta P = f_D \frac{L}{D} \frac{1}{2} \rho v^2 \tag{31}$$

where L is the length of the pipe the pressure drops through, D is the characteristic length of the pipe, and ρ is the density of the medium. The outlet of the injector is assumed to be at atmospheric pressure. Therefore, the pressure at each point in the microfluidic device is calculated by adding the pressure drop from Equation (*31*) to atmospheric pressure. The distance between the outlet and the edge of the frame is 12.5 millimeters, and this value is added to the x-position of the bubble's centroid and substituted into Equation (*31*) as L.

With the pressure known, the mass of each bubble in each frame is calculated using Equation (*28*) The calculation of the average bubble mass is considered more accurate since it relies on fewer unvalidated assumptions. As such, the mass results calculated using the cylinder

stacking method are normalized to the average mass derived from the frequency analysis. This was done by obtaining a correction factor given by:

$$A_m = \frac{\overline{m}_{frequency}}{\overline{m}_{pixel}} \tag{32}$$

where $\overline{m}_{frequency}$ represents the average mass calculated from the frequency, and $\overline{m}_{pixel}$ represents the average mass calculated by the cylinder stacking method. The individual masses of each bubble were then multiplied by this correction factor.

Finally, the masses for each condition are converted back to volume, assuming the pressure in the test section is atmospheric plus the hydrostatic pressure of the surrogate fluid, measured as 47 inches above the point of measurement. Using Equation (*28*). With Equation (*10*), the volume can be converted to equivalent diameter.

4.3. Experimental Setup Inside Loop

The injector is designed to control the size of the bubbles produced in the test section, so it is essential to verify its full functionality by capturing images of the bubbles within the test section. For these tests, the complete injector assembly is fastened securely to the test section.

As in the outside loop tests, the first critical step for the inside loop tests is preparing the glycerin-water mixture. This process begins by weighing a 5-gallon bucket of glycerin (denoted as W_{Gf}) on a scale with a resolution of 0.05 pounds. The bucket is then emptied into an empty 15-gallon tank. The bucket is reweighed (denoted as W_{Ge}), and then filled with water and weighed again (denoted as W_{Wf1}). After emptying the bucket into the tank, the bucket is reweighed

(denoted as W_{We}). These measurements allow for the calculation of the amount of glycerin added to the tank using the formula:

$$W_G = W_{Gf} - W_{We}. \tag{33}$$

W_{we} is used instead of W_{Ge} due to residual glycerin left in the bucket during the initial measurement. Next, the amount of water added to the tank is determined using the relation:

$$W_{W1} = W_{Wf1} - W_{Ge}. \tag{34}$$

Finally, the total amount of water required is calculated as:

$$W_W = \frac{0.65}{0.35} W_G = \frac{13}{7} W_G. \tag{35}$$

With this, the amount that was still needed to be added can be determined with:

$$\begin{gathered} W_W = W_{W1} + W_{W2} + W_{W3} \\ W_{W2} + W_{W3} = W_W - W_{W1}, \end{gathered} \tag{36}$$

where W_{W2} and W_{W3} represent the weights of water added in the second and third buckets. The bucket is then refilled with water and weighed again (denoted as W_{Wf2}) then emptied into the tank. The weight added from the second bucket of water is determined similarly to Equation (23):

$$W_{W2} = W_{Wf2} - W_{We}. \tag{37}$$

Finally, the weight of water in the third bucket is calculated by:

$$W_{Wf3} = W_W - W_{W1} - W_{W2} + W_{We}. \tag{38}$$

Water was then added to the third bucket until it reached that weight, and it was added to the tank.

Since the pump is not rated for high density liquids such as glycerin the mixture must be manually stirred to ensure the glycerin is not settled at the bottom before the pump is run. After

this initial mixing, the pump circulates the fluid through the test section at maximum speed for further homogenization. Glycerin is highly soluble in water, so once it is mixed in the first time, this step is no longer required. Since this process introduces small bubbles into the fluid, the mixture must sit for 30 minutes with the pump off before testing can proceed.

The test setup, shown in Figure 4.14, is more complex than the outside loop setup but remains straightforward. A high-speed camera on a tripod was positioned facing the test section, capturing a region 12 inches above the injection site. The light source was clamped to the aluminum structure on the opposite side of the test section. The syringe pumps and light controller were placed on a cart next to the aluminum structure.

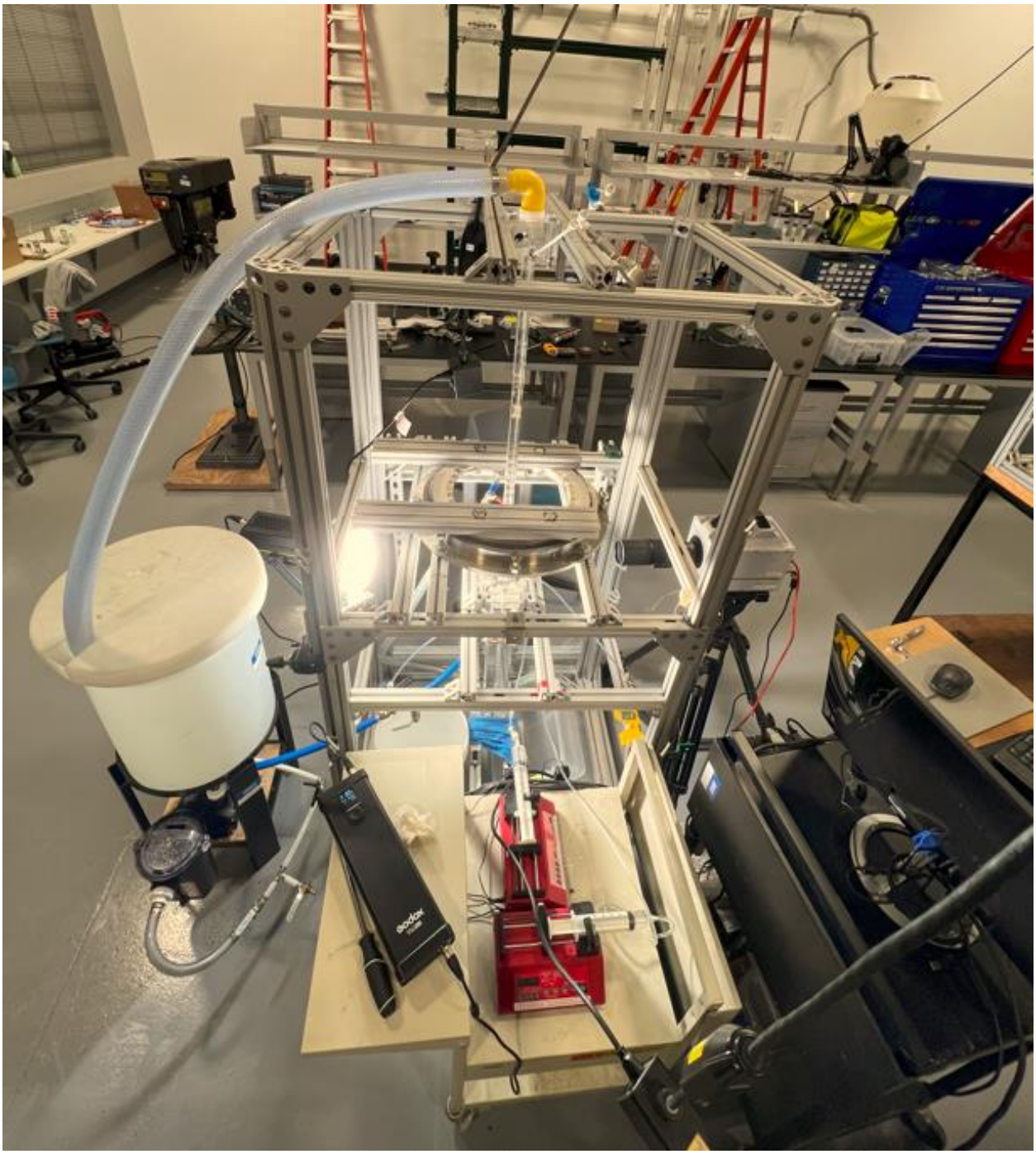

Figure 4.14: Picture of inside test loop experimental setup

A total of 25 injection conditions were tested, with each trial capturing 500 images at 60 frames per second and a shutter speed of 1/4000 of a second. These conditions were composed of five surrogate fluid flow rates paired with five different air flow rates. The flow rates for each substance are detailed in Table 4.2. The flow rates for the air injection were again corrected as outlined in Section 4.1. The flow rate in the test section, measured by the flow meter, was 3.55 gallons per minute, which, after correction using Equation (*21*), corresponded to a true volumetric flow rate of 3.3976 gallons per minute. This flow rate produced an average fluid velocity of 0.71 m/s in the test section. The relatively low frame rate ensured that no two frames captured the same bubble, maximizing the number of bubbles analyzed per frame and eliminating the need for complex processing strategies to handle bubbles appearing in consecutive frames.

Table 4.2: Injection flow rates

Glycerin-Water Mixture Injection Rate (mL/hr)	100, 110, 120, 130, 140
Gas Injection Rate (mL/hr)	40.58, 54.10, 67.63, 81.16, 94.68

It is important to note that there was minimal overlap between the flow conditions tested in the inside and outside loop experiments. During initial tests, air pockets formed at the injection site, an issue that diminished when the liquid flow rate increased. It is likely that the injector's performance was affected by the pressure at the injection site. For comparable injection conditions, the air inlet pressures in the inside loop tests were on average 0.13 psi lower than

those in the outside loop tests. Since the static pressure at the injection site was not measured and several uncontrolled variables were present, accurately estimating this pressure was not possible. For example, the outlet tube feeding into the tank was partially filled with surrogate fluid during tests, and the amount of fluid was not measured, making it difficult to estimate a reference pressure. Future tests should incorporate pressure gauges at various points in the test section to collect more precise reference pressures. It is clear that static pressure at the injection site influences the injector's performance, so this dependency should be studied further, especially for applications where the static pressure significantly deviates from atmospheric pressure.

To determine the pixel-to-millimeter conversion factor for the images, calibration sheets were placed on both the near and far sides of the test section. The possibility of a different conversion factor in the middle of the test section was considered, but the conversions from both sides were identical, making this step unnecessary.

4.4. Image Processing Inside Loop

The processing of the images for the inside loop tests is much simpler. Like the outside loop image processing, the process begins by importing the raw image as displayed in Figure 4.15.

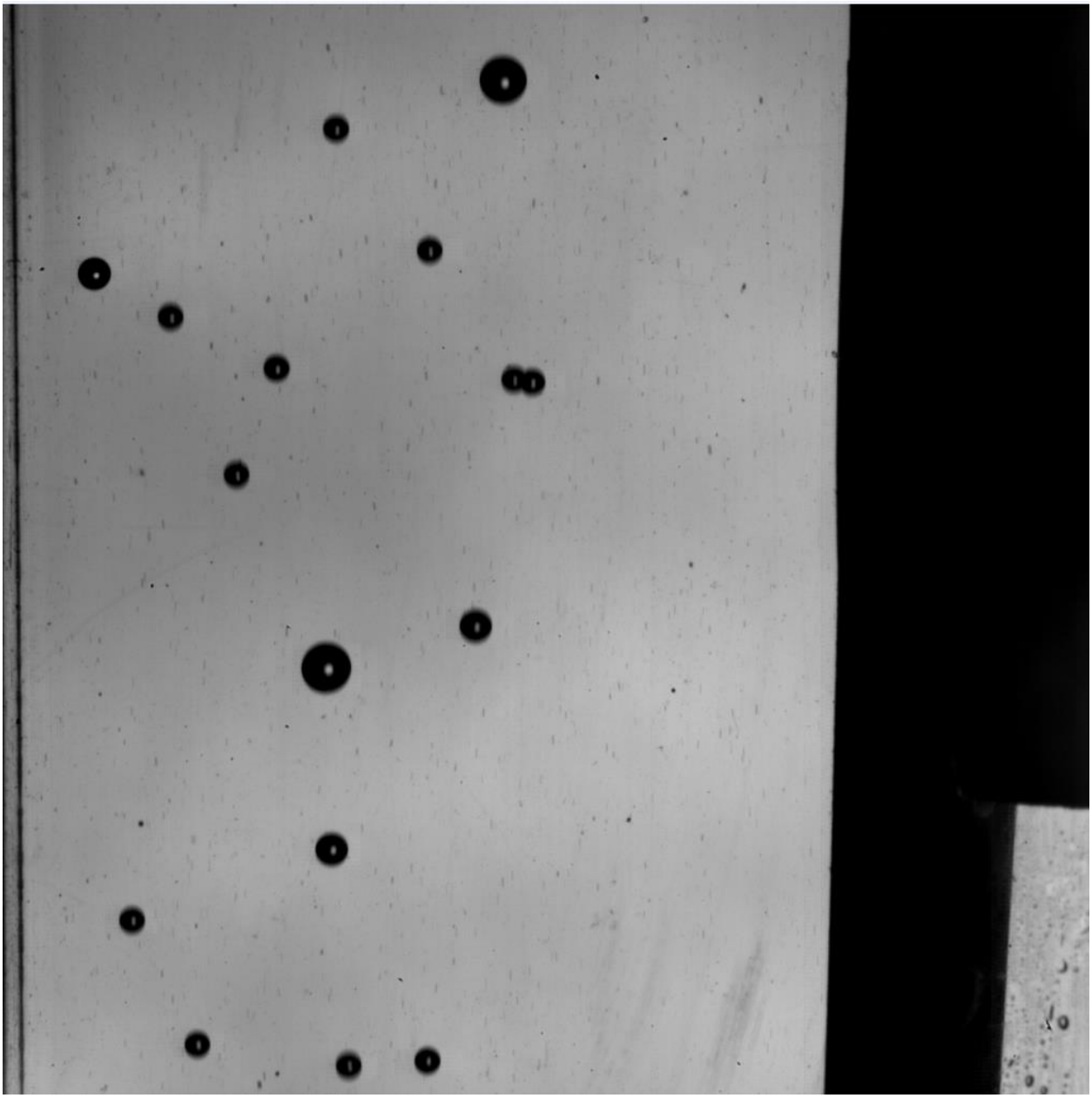

Figure 4.15: Raw image of inside test loop bubbles

Although the calibration sheets are visible on the right side of the image, their details are indistinguishable due to backlighting. To properly calibrate the pixel-to-millimeter conversion, a

front-lit image is required, as shown in Figure 4.16.

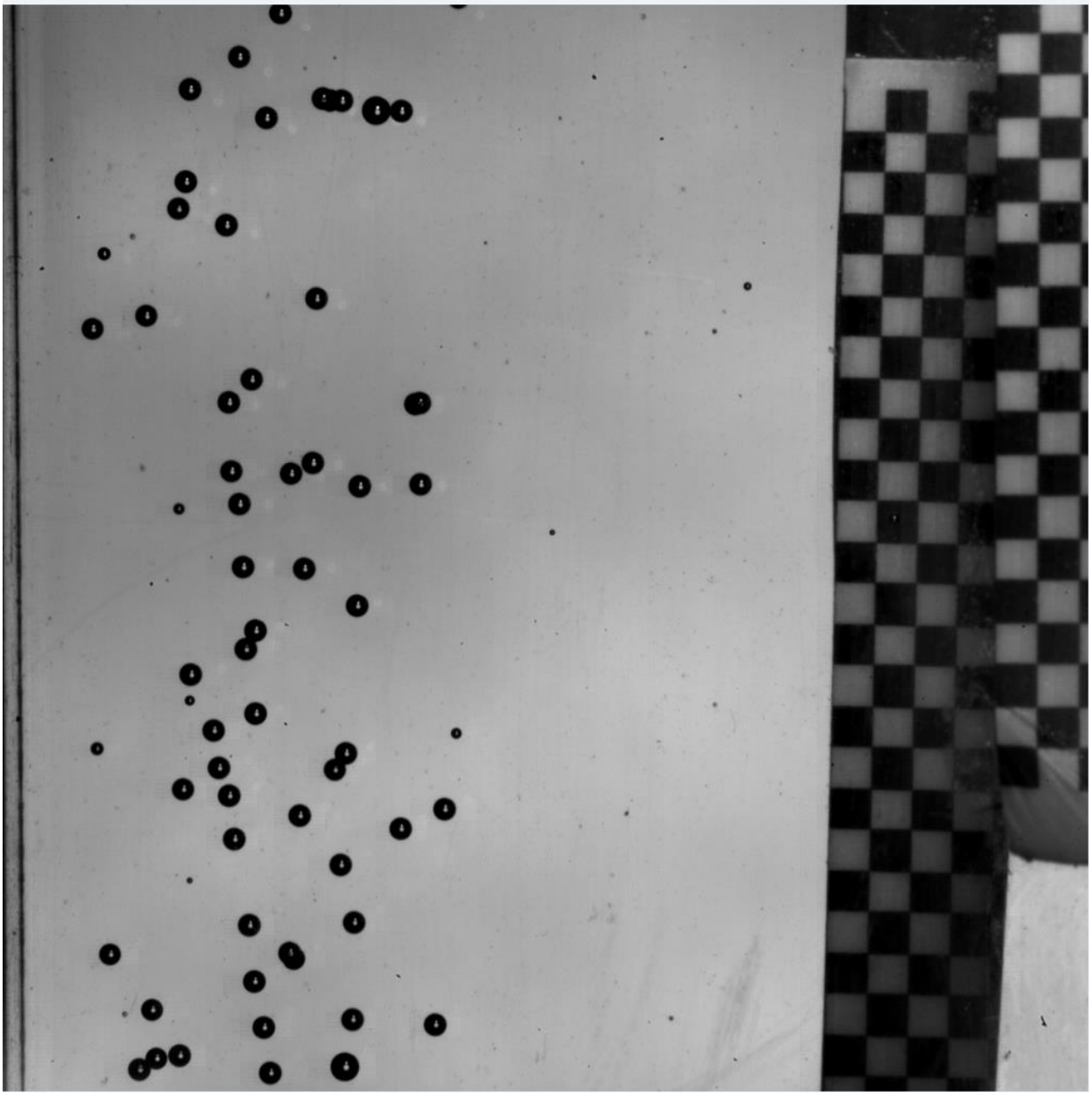

Figure 4.16: Calibration image for inside loop tests

Next, a background image is created by analyzing 100 frames and identifying pixels that remain consistent across all the images. The resulting background image is shown in Figure 4.17.

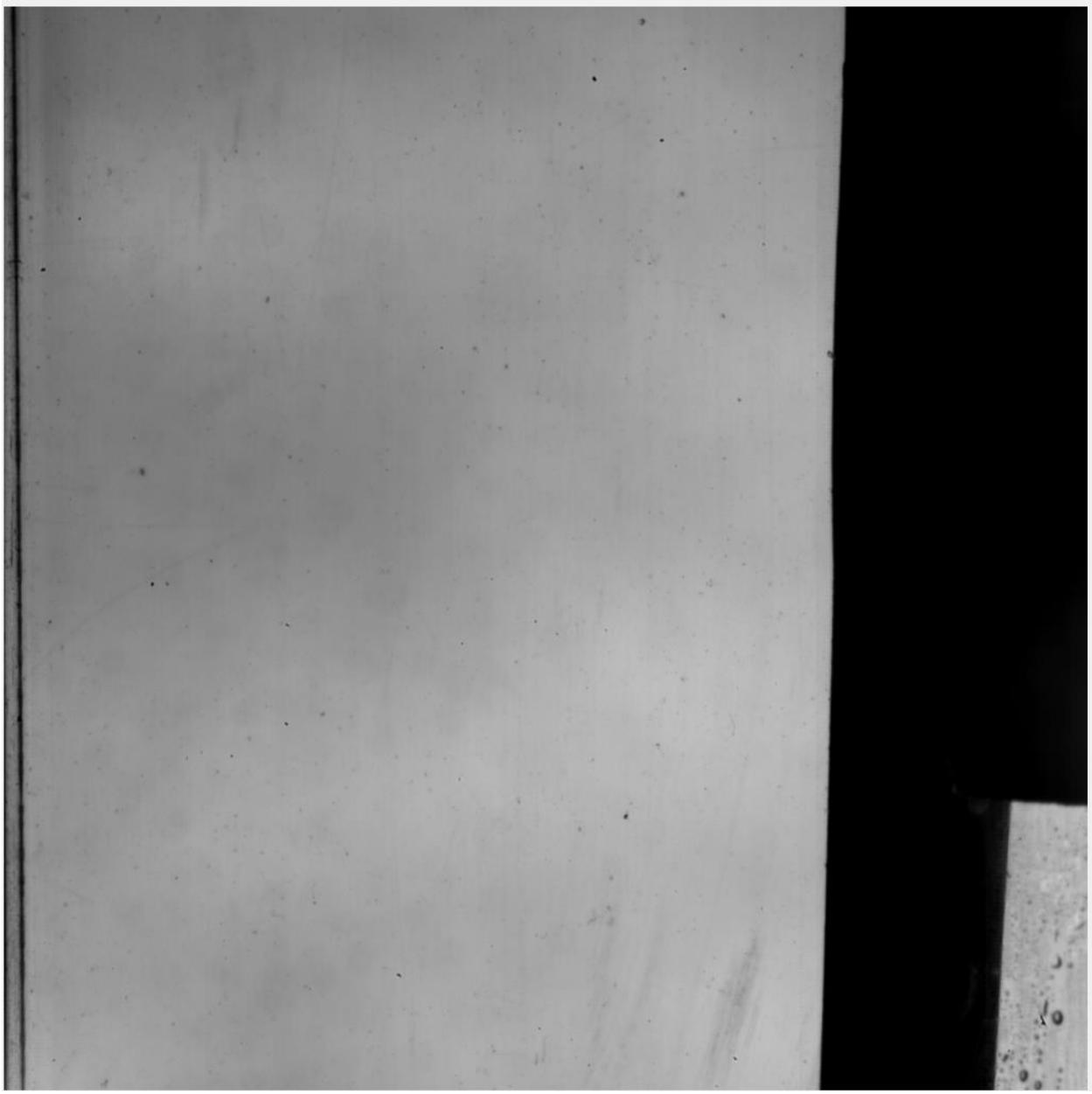

Figure 4.17: Background image

Using this background image, a region of interest is identified, and the raw image is cropped to include only the relevant parts for analysis. The cropped image is displayed in Figure 4.18.

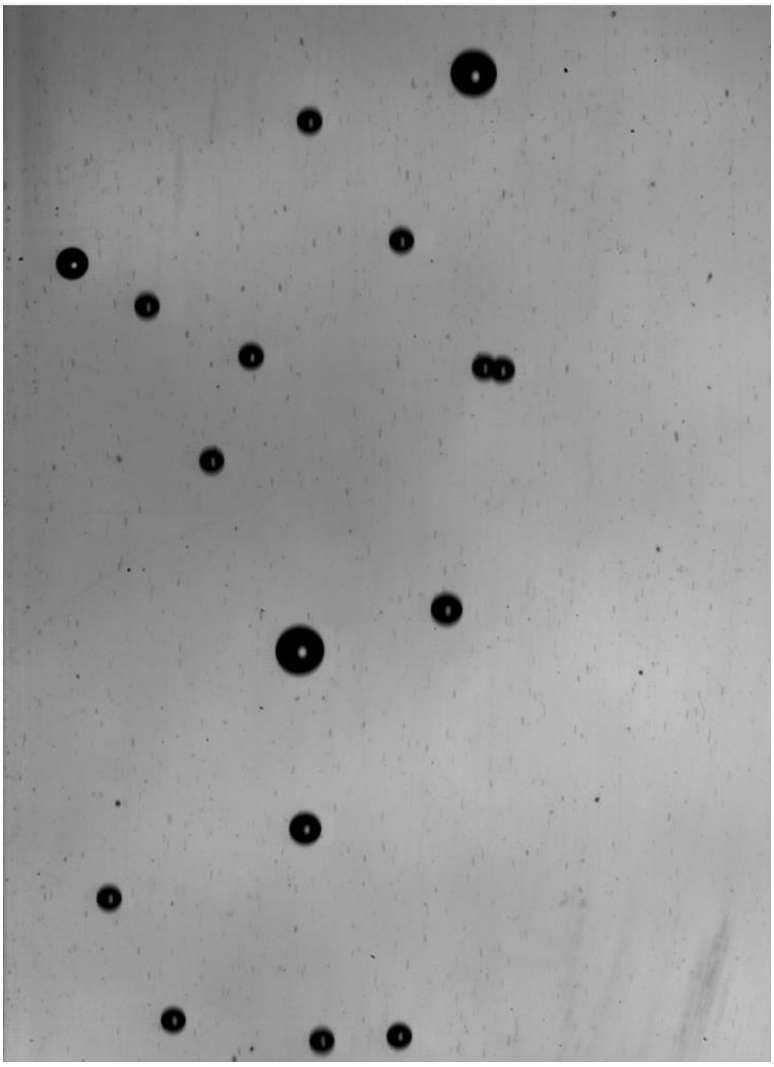

Figure 4.18: Cropped image of inside test loop bubbles

The cropped raw image is then subtracted from the cropped background image so that image is inverted and the only entities that remain are those that are unique to that frame. The result is displayed in Figure 4.19

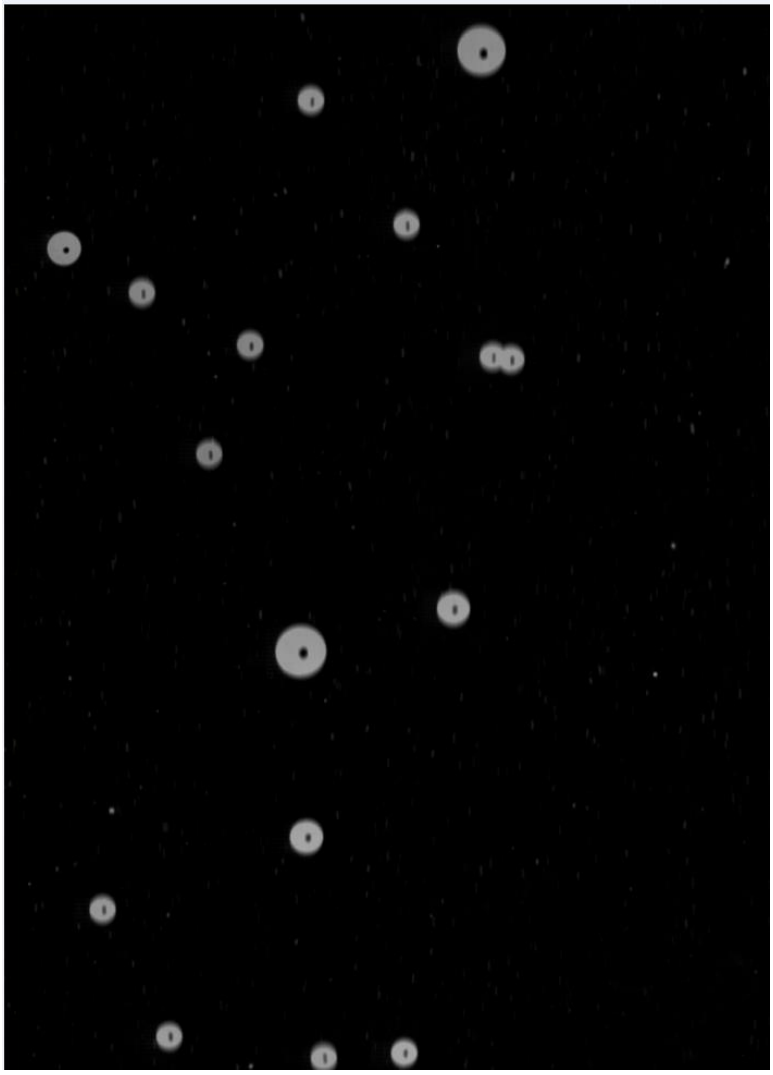

Figure 4.19:Inverted image of inside test loop bubbles

As in Section 4.2, the image is saturated by adjusting the top 1% of pixels to value 1 and the bottom 1% to value 0, enhancing contrast. The result is displayed in Figure 4.20.

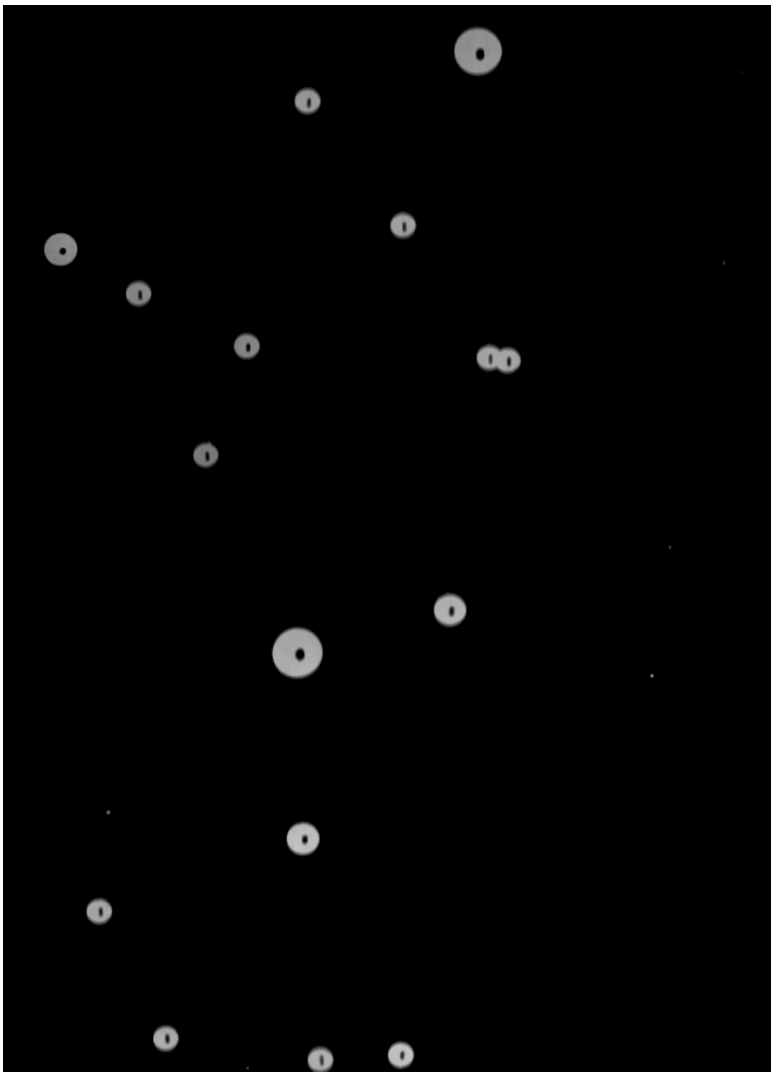

Figure 4.20: Saturated image of inside test loop bubbles

The image is then passed through a median filter, as detailed in Section 4.2. The filtered image is shown in Figure 4.21.

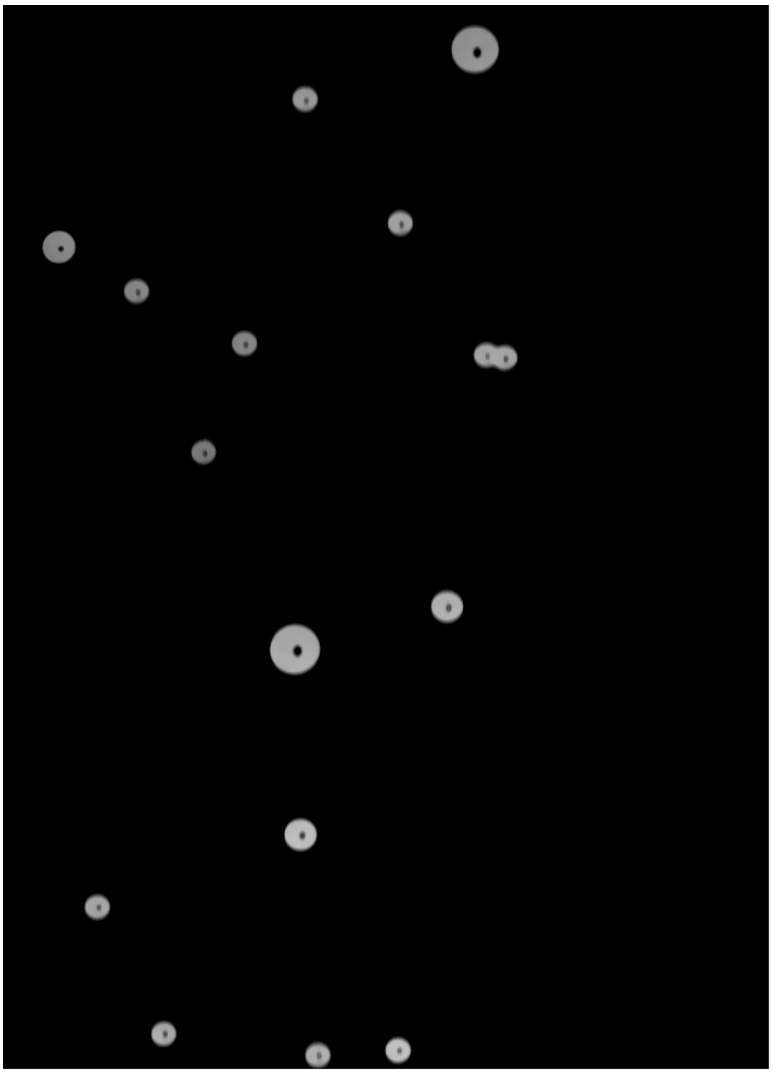

Figure 4.21: Filtered image of inside test loop bubbles

Following this, the image is binarized similarly to the process outlined in Section 4.2. The binarized image is displayed in Figure 4.22

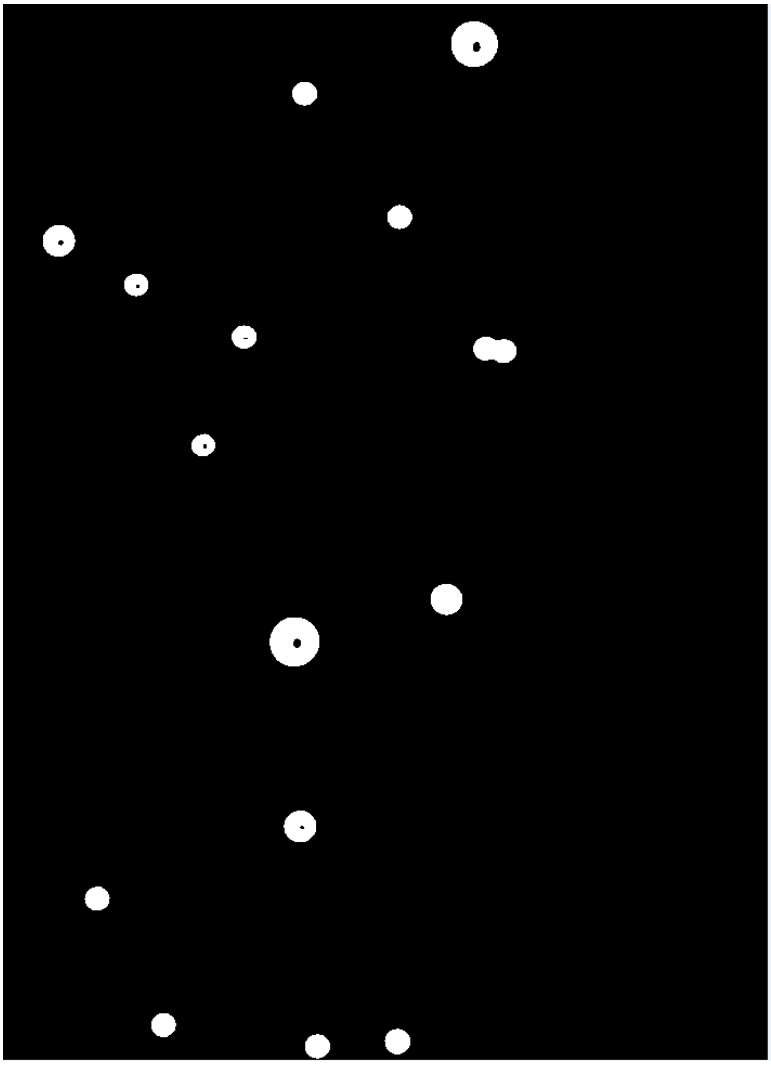

Figure 4.22: Binarized image of inside test loop bubbles

Next, any holes within the individual bubbles are filled, as shown in Figure 4.23.

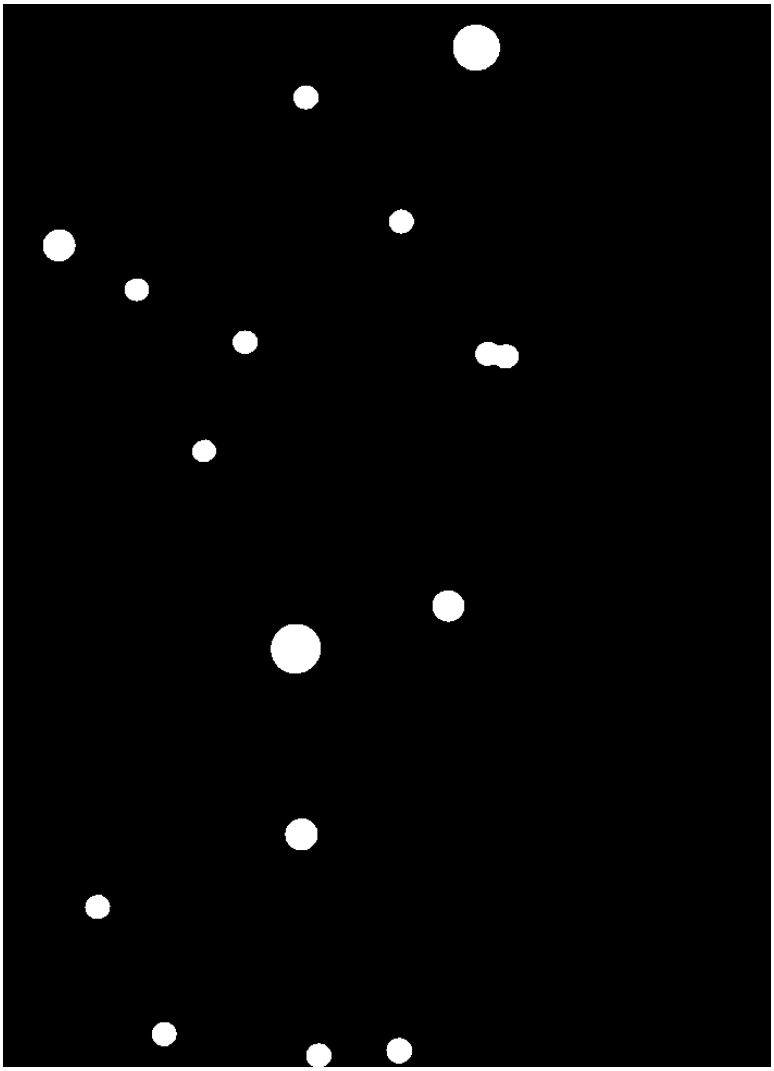

Figure 4.23: Binarized image of inside test loop bubbles with the bubbles filled in

Entities that are either too small (having less than half the number of pixels as the smallest expected bubble) or too large (having more than twice the number of pixels as the largest expected bubble) are then removed from the image, as shown in Figure 4.24.

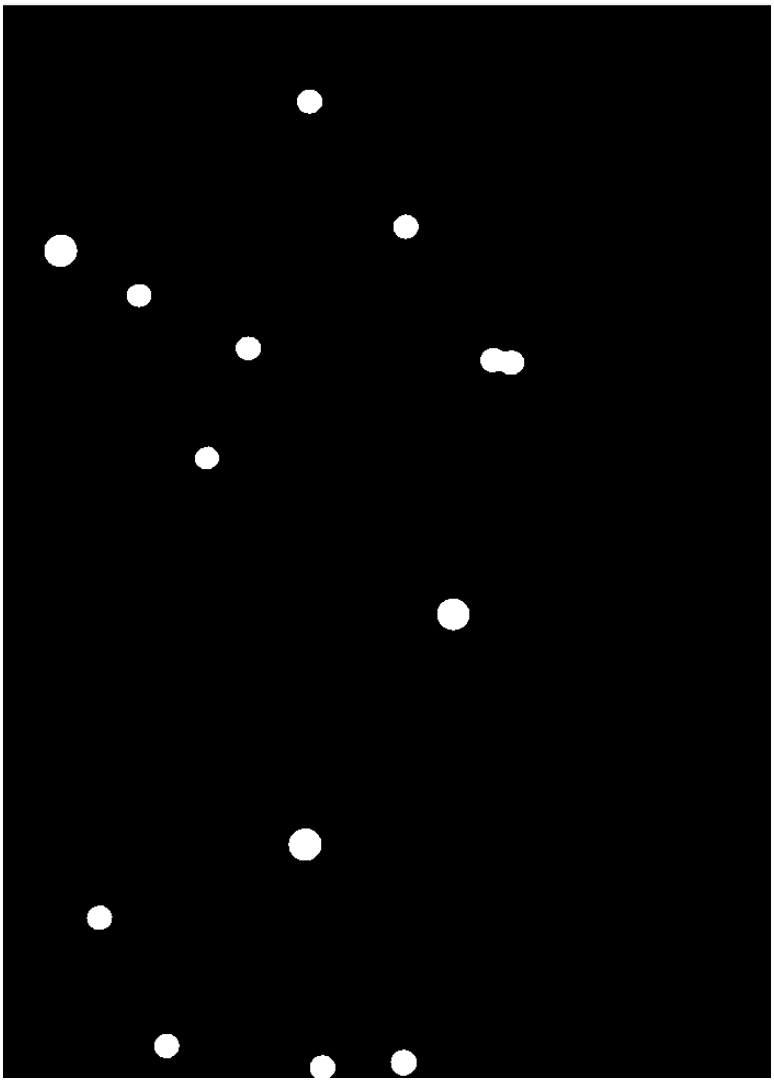

Figure 4.24: Binarized image of inside test loop bubbles with big and small bubbles removed

It is only of interest to this study to analyze individual bubbles. Particularly, the bubbles this study would like to evaluate are the smallest ones that come straight from the injector without joining together with any other bubbles. A convenient way to eliminate entities that are cut off on the borders of the region of interest as well as eliminate bubbles clumped together in groups is to eliminate bubbles with a circularity below a certain limit. The circularity is a number that

approaches 1 the more circular an entity is, and it is extracted for each element from the MATLAB "regionprops" function. The final image after applying the circularity filter is shown in Figure 4.25. All of the image conversion processes for the inside of the loop test were done with one MATLAB script (see Appendix B).

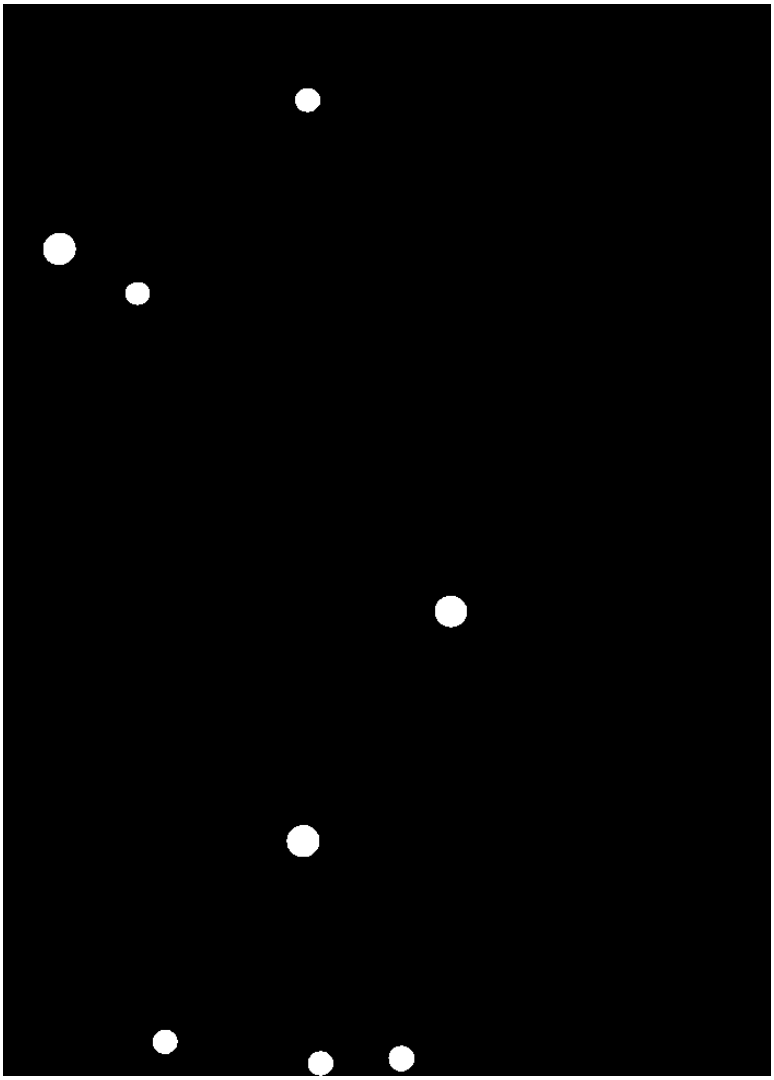

Figure 4.25: Final image used to calculate the size of the bubbles

Since the bubbles appear circular in the images, they are assumed to be spherical. This allows the equivalent diameter of the circles to represent the equivalent diameter of the spheres. This diameter is easily extracted from the images using MATLAB's "regionprops" function. It is evident from the images that some bubbles are significantly larger than others, likely due to the coalescence of two or more bubbles. Bubble coalescence is an expected phenomenon, but it is of interest to this study to analyze the size of these bubbles as they exit the injector and disregard coalesced bubbles as these would skew the results. To assess the validity of the coalescence assumption, the diameters of all the bubbles are plotted on histograms, as shown in Figure 4.26.

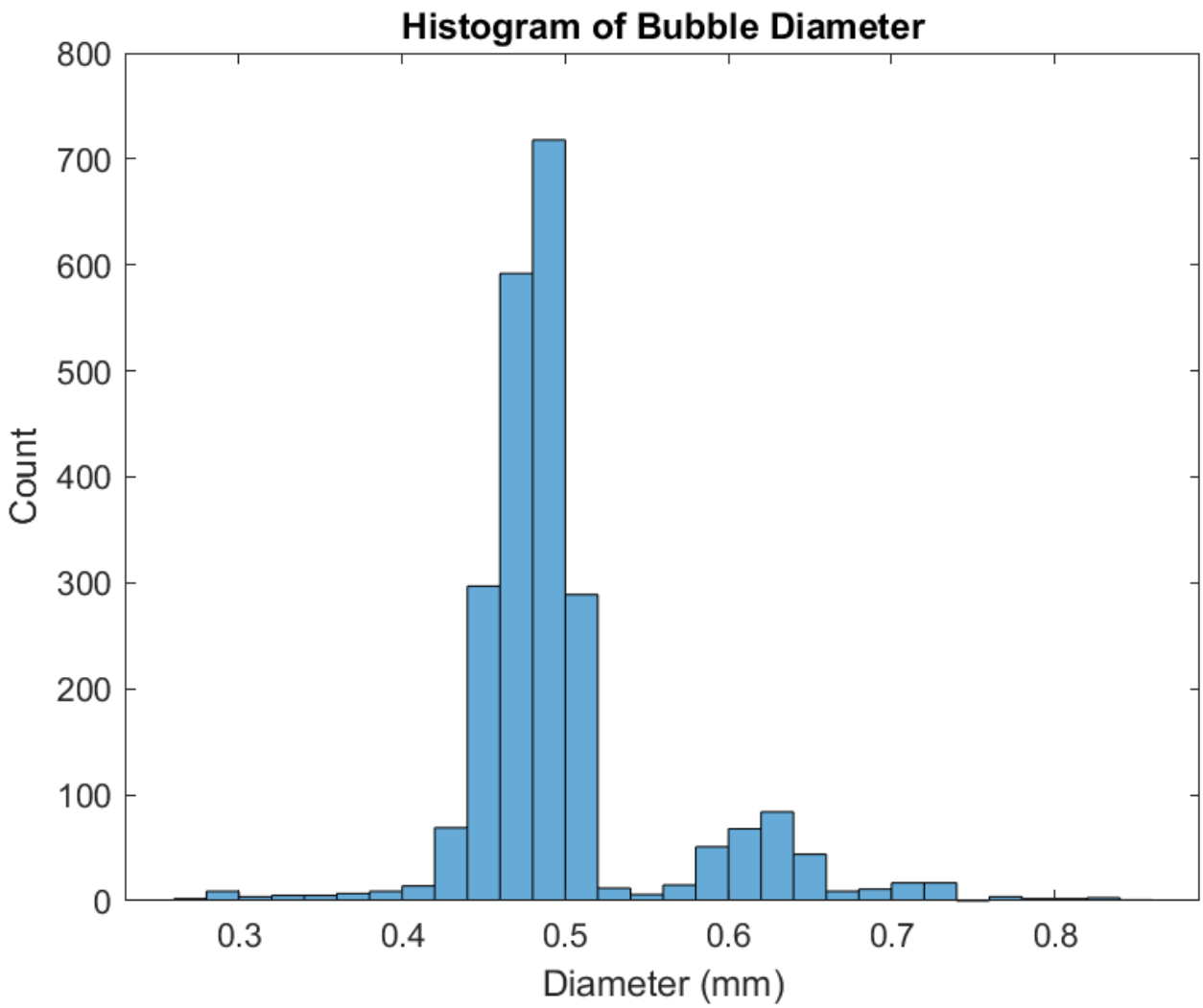

Figure 4.26: Histogram showing distribution of bubble volume

The histogram shows three distinct modes, suggesting that the coalescence assumption is valid. The peaks are evenly spaced at multiples of the first peak, indicating that the first peak represents the true equivalent diameter of the bubbles exiting the injector. To refine this measurement, MATLAB's "ksdensity" function is used to generate a smoothed distribution of the equivalent diameters, as shown in Figure 4.27. The diameter corresponding to the first peak

in this distribution is taken as the diameter of the bubbles injected into the test section.

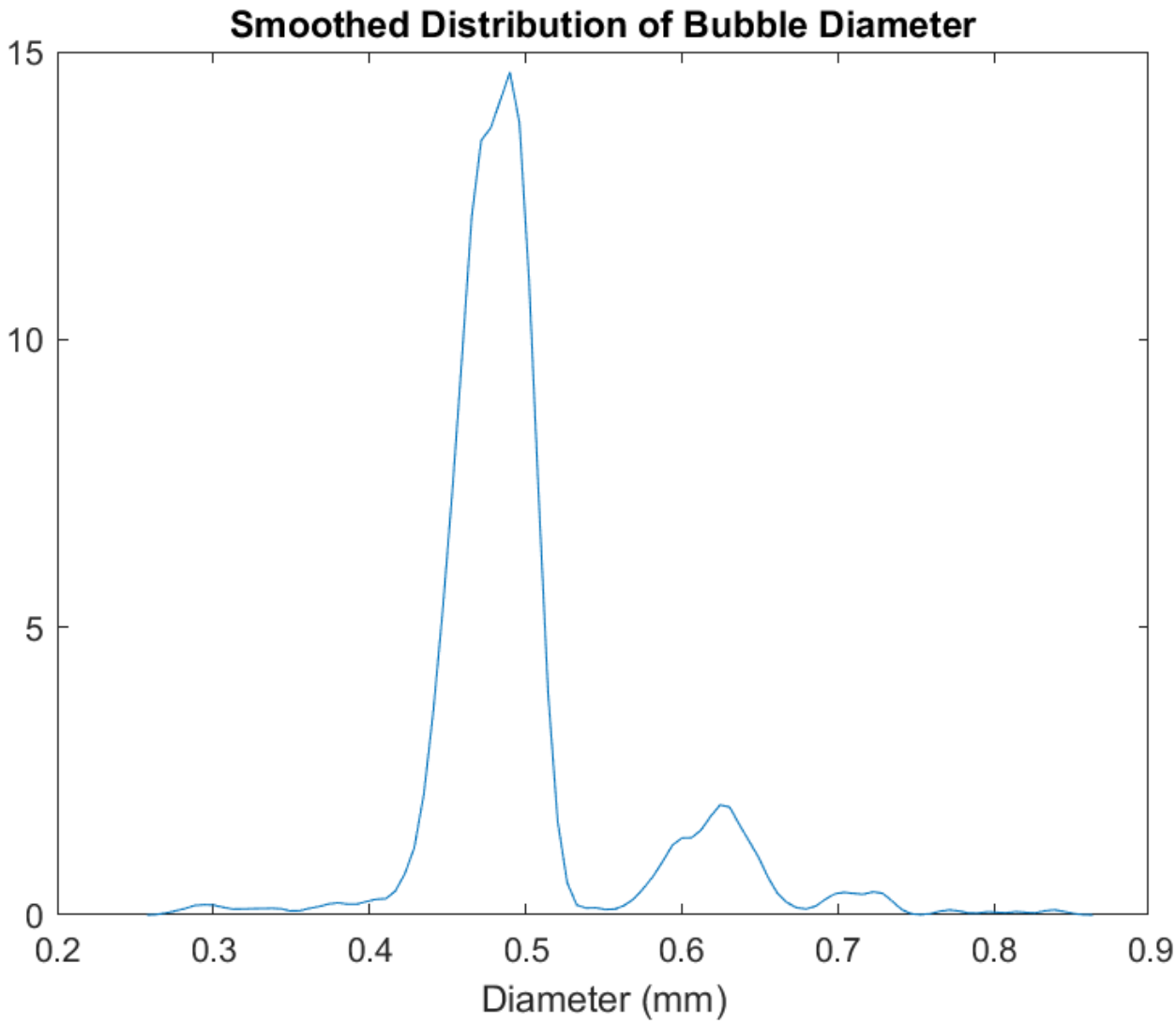

Figure 4.27: Smoothed distribution of bubble diameter

To further validate the accuracy of this method, the volumes corresponding to the equivalent diameters of the bubbles in the images are divided by the volume corresponding to the extracted diameter. A histogram of this data is shown in Figure 4.28.

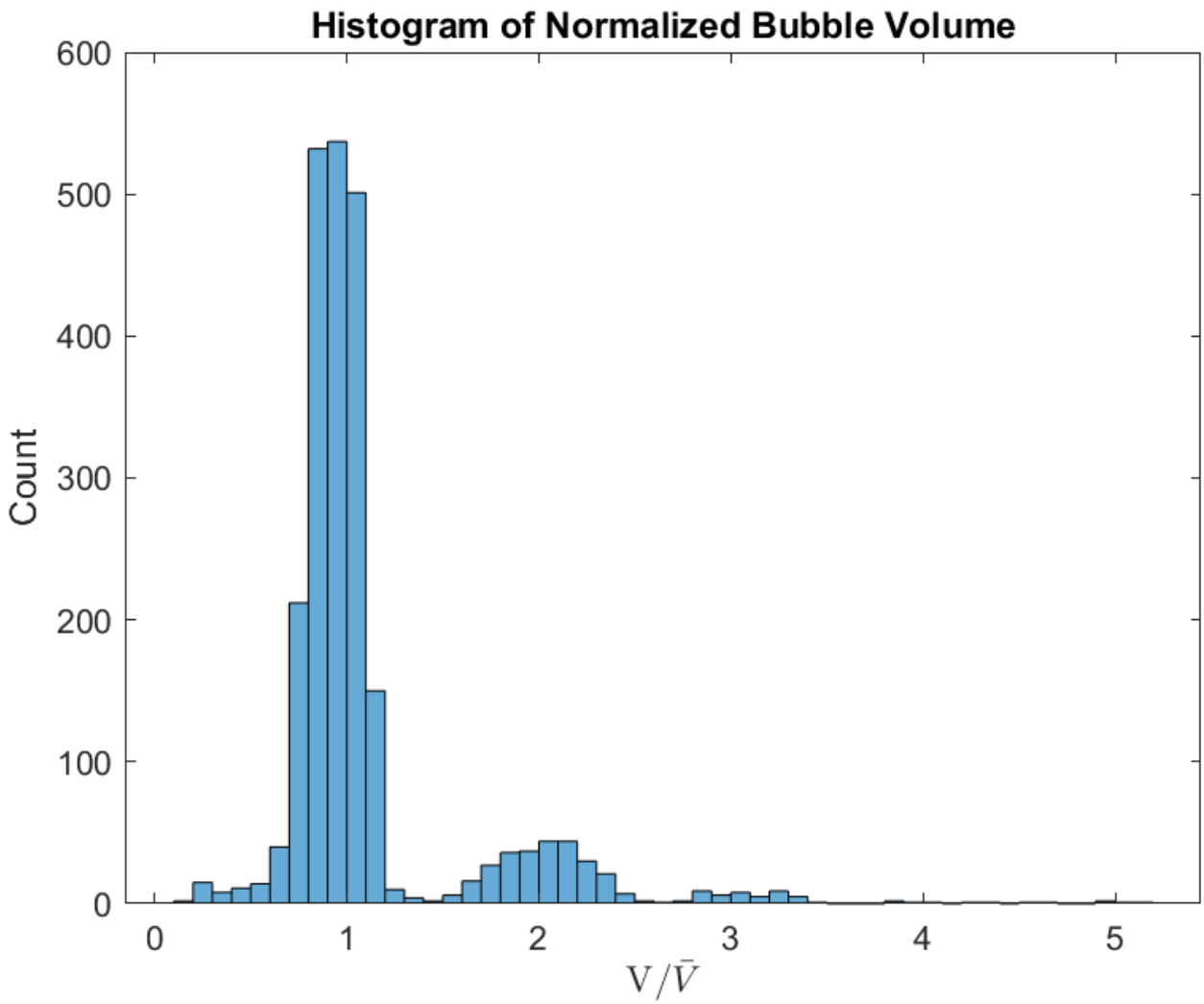

Figure 4.28: Histogram of normalized bubble volume

The histogram's peaks at values of 1, 2, and 3 provide additional evidence supporting the coalescence assumption and the validity of the method used to calculate the diameter of the bubbles exiting the injector.

Chapter 5

5. Results and Discussion

5.1. Injector Test Results Outside The Test Loop

Using the methods described in Chapter 4, the equivalent diameter of the bubbles produced by the injector was obtained. The results are displayed in the surface plot shown in Figure 5.1. While it is challenging to discern trends from the static plot alone, the expected general trend is evident: the equivalent diameter is positively proportional to the gas flow rate and negatively proportional to the liquid flow rate.

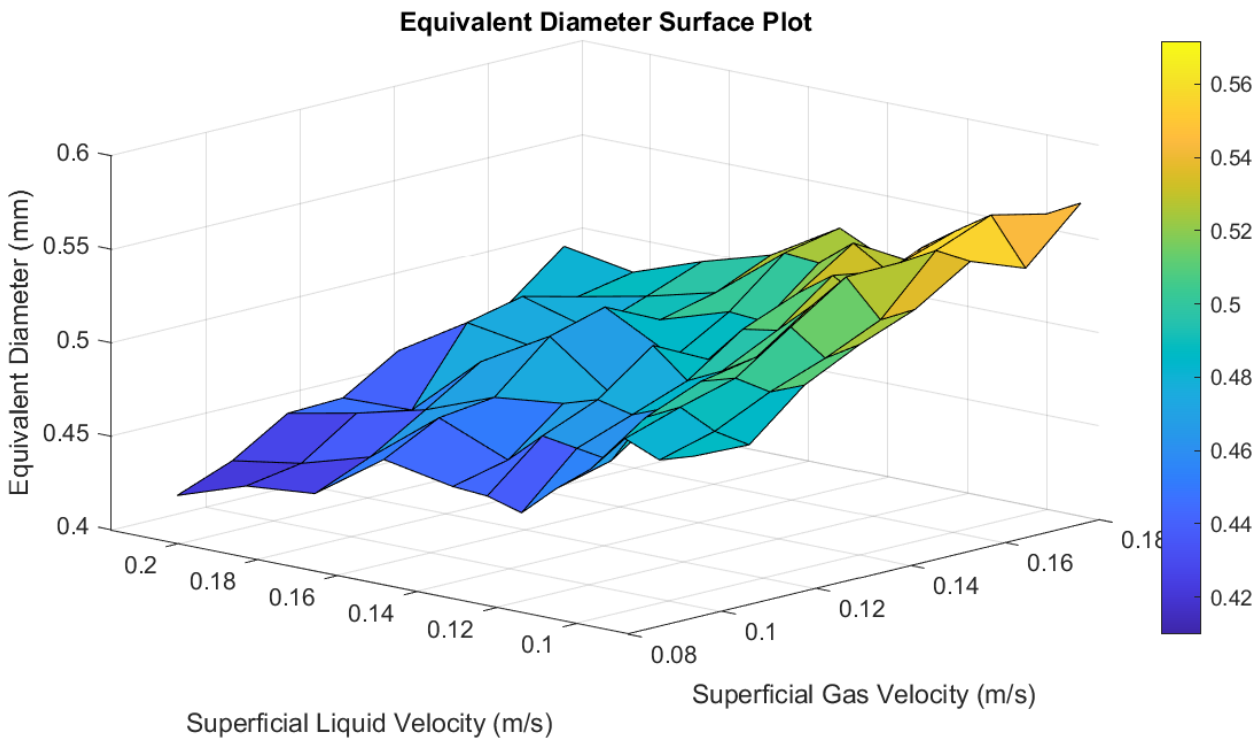

Figure 5.1: Surface plot showing the relation between the injection rates and equivalent diameter

To better visualize these trends, the data were split into subplots. Figure 5.2 shows the behavior of the equivalent diameter as a function of liquid flow rate for each constant gas flow rate. These plots clearly illustrate that the equivalent diameter decreases as the liquid flow rate increases.

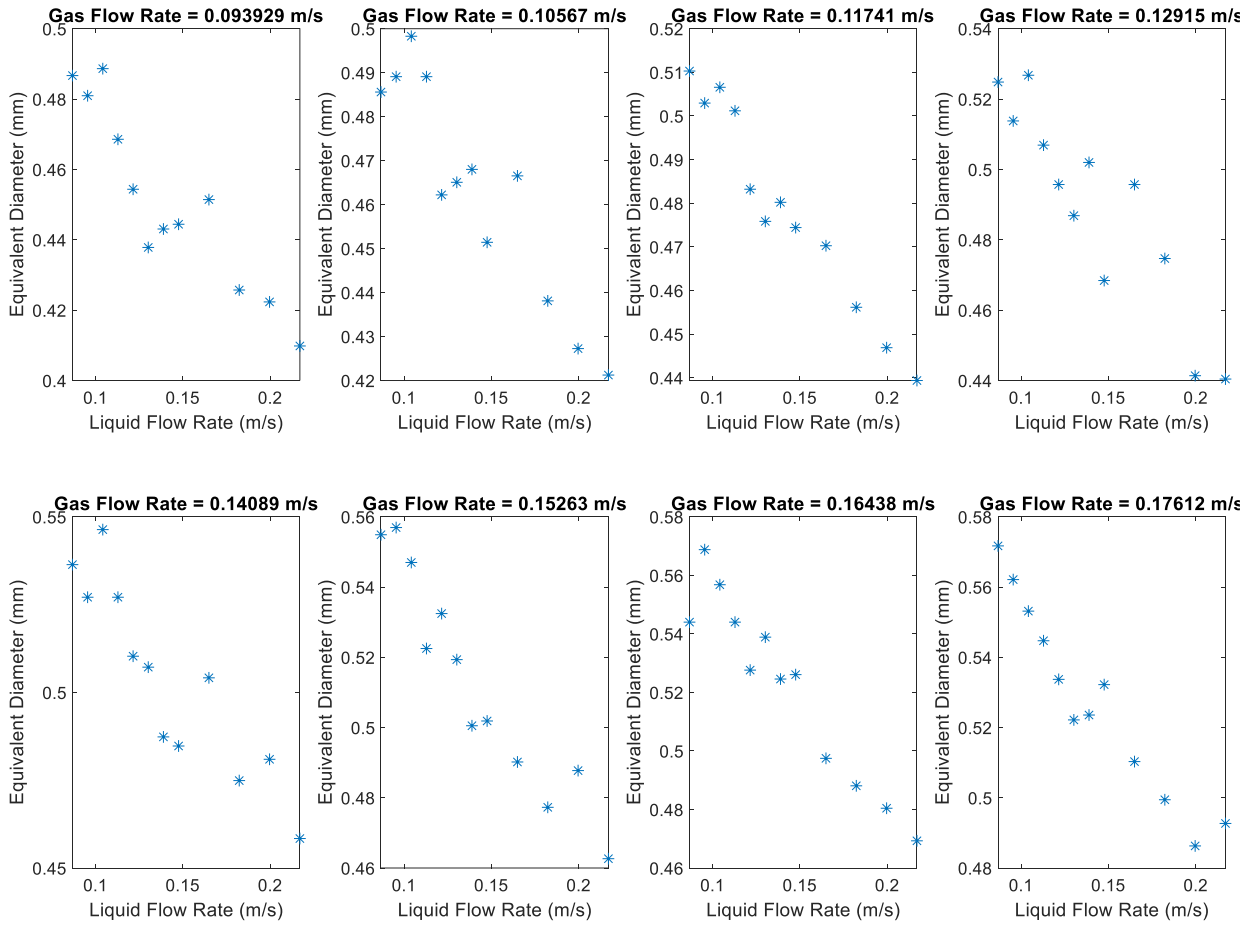

Figure 5.2: Grid plot displaying relationship between liquid flow rate and equivalent diameter

Similarly, Figure 5.3 was created by holding the liquid flow rate constant and plotting the equivalent diameter as a function of gas flow rate for each liquid flow rate. These plots clearly show that the equivalent diameter increases as the gas flow rate increases. This trend aligns with the observations of Lu et al. (2014) and is intuitive: larger bubbles are expected when a higher fraction of the total injected volume is air.

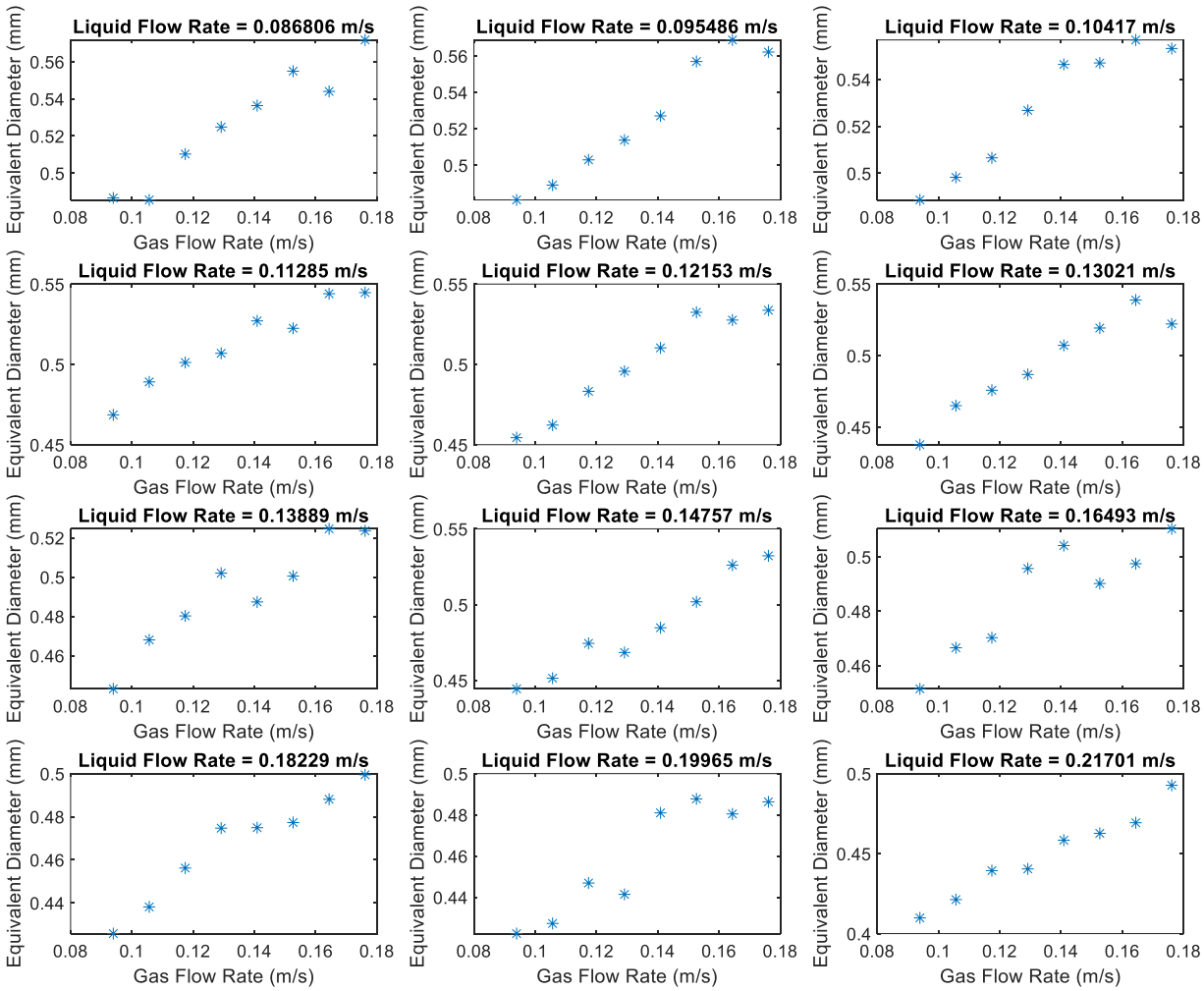

Figure 5.3: Grid plot displaying relationship between gas flow rate and equivalent diameter

While it is useful to see a clear trend in the average equivalent diameter of the bubbles as a function of liquid and gas flow rates, a second important function of the injector is that there is little variation of bubble size from bubble to bubble. The way this variation is quantified is the coefficient of variation:

$$CV = \frac{\sigma_{d_{eq}}}{\overline{d_{eq}}}, \tag{39}$$

where $\overline{d_{eq}}$represents the average equivalent diameter of the bubbles generated in a particular flow condition, and $\sigma_{d_{eq}}$is the standard deviation of the equivalent diameters of the bubbles produced in each flow condition. The distribution of the sizes of the bubbles is defined from the cylinder stacking process defined in Section 4.2. The complete cylinder stacking method gives a distribution of the masses of the bubbles, so to obtain the distribution of equivalent diameters, the following relationship is used:

$$\sigma_{d_{eq}} = \frac{d\, d_{eq}}{d\, m} \sigma_m, \tag{40}$$

where $\frac{d\, d_{eq}}{d\, m}$ represents the derivative of the equivalent diameter of the bubbles with respect to mass of the bubbles defined as:

$$\frac{d\, d_{eq}}{d\, m} = \frac{d\, d_{eq}}{d\, V} \frac{d\, V}{d\, m}, \tag{41}$$

where $\frac{d\, d_{eq}}{d\, V}$ represents the derivative of the equivalent diameter of the bubbles with respect to the volume of the bubbles and $\frac{d\, V}{d\, m}$ represents the derivative of the volume of the bubbles with respect to the mass of the bubbles. To obtain $\frac{d\, d_{eq}}{d\, V}$ and $\frac{d\, V}{d\, m}$ Equation (*10*) and (*28*) are differentiated with respect to V and m respectively. The result of this gives an average coefficient of variation of equivalent bubble diameter of bubbles within the microchannels of 6.98%.

It is also of interest to this study to analyze the frequency of bubble generation. Graphs to show the relationship between the liquid flow rate and frequency can be seen in Figure 5.4. Similarly, graphs to show the relationship between the gas flow rate and frequency can be seen in

Figure 5.5. From these figures it is clear to see there is a strong positive correlation between liquid flow rate and frequency; furthermore, there is a relatively weak positive relationship between gas flow rate and frequency.

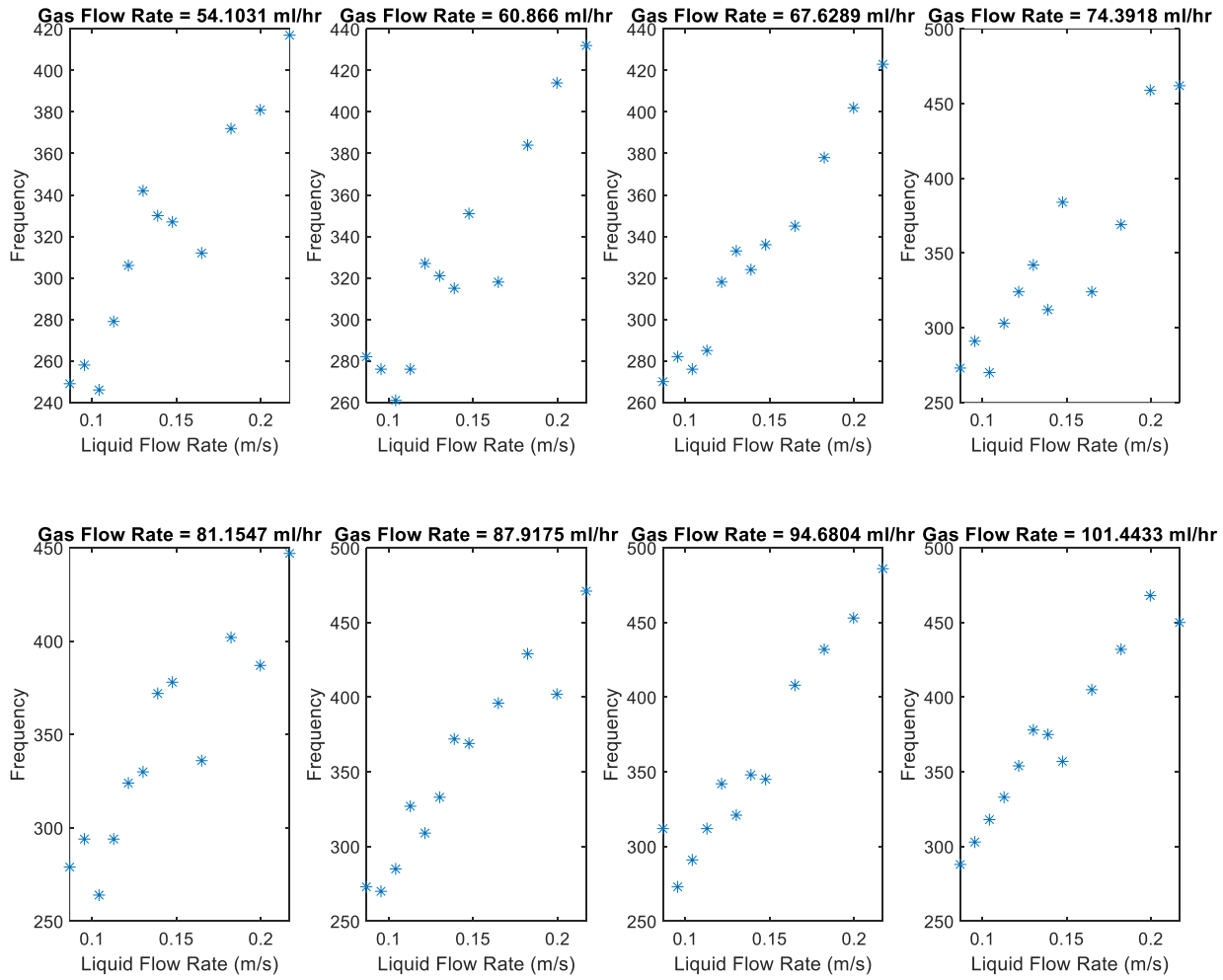

Figure 5.4: Grid plot displaying relationship between liquid flow rate and Bubble generation frequency

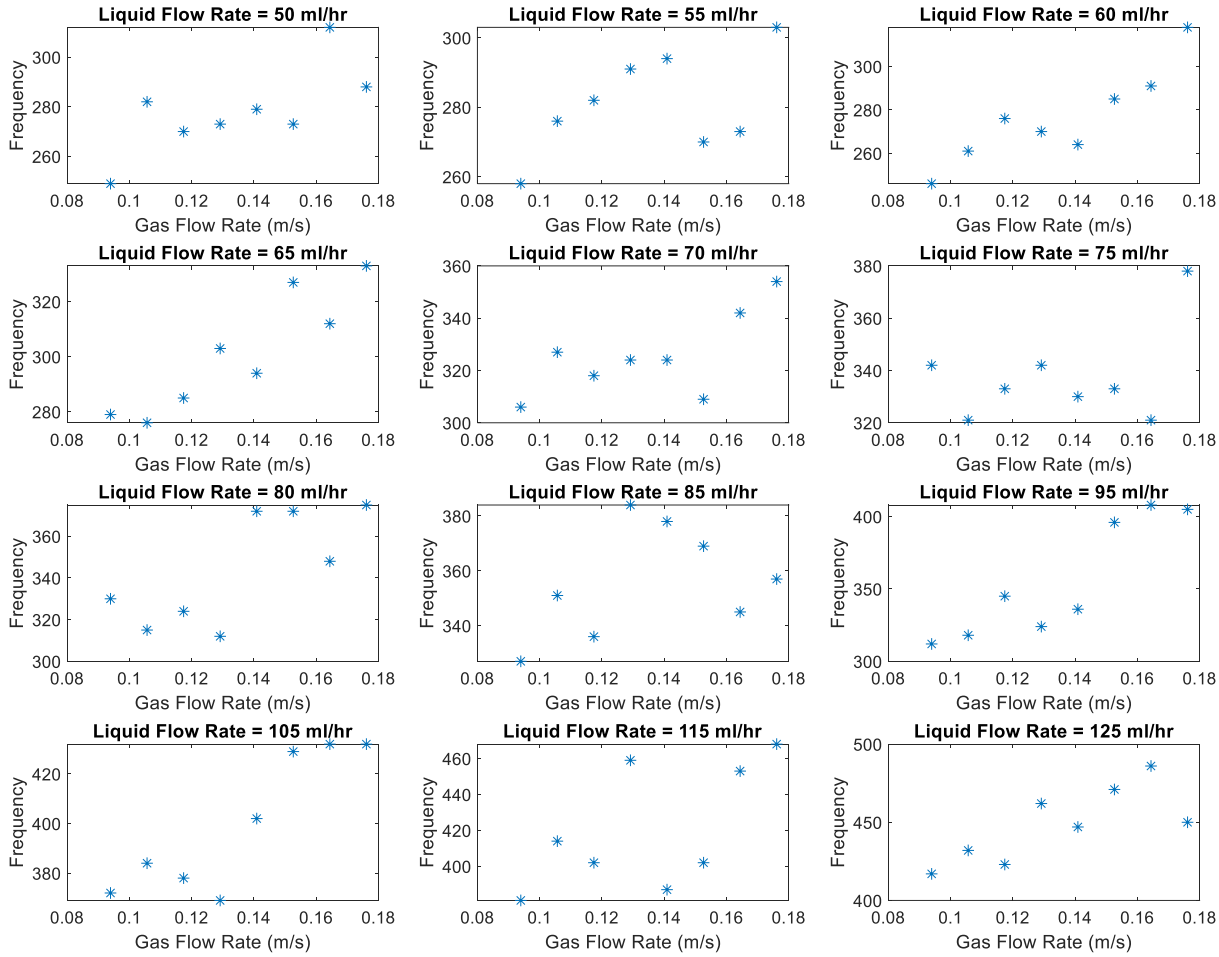

Figure 5.5: Grid plot displaying relationship between gas flow rate and Bubble generation frequency

An important observation is that the applicability and functionality of models found in the literature were not clearly defined. It is often unclear if a model performs well under certain conditions, even though they are typically reported with the Capillary and Reynolds number ranges under which they were developed. Operating within the range defined by Lu et al. (2014) but with

modified geometry, such as a reduced channel width, revealed that no bubbles formed under the prescribed conditions. Therefore, an additional condition for applicability should be established.

Since bubble formation heavily depends on slug flow within the microchannels, it is crucial to ensure that tested flow rates result in slug flow. This can be predicted using a flow pattern map originally developed by Mishima and Ishii (1984) shown in Figure 5.6. The vertical axis of this graph represents the superficial liquid velocity, while the horizontal axis represents the superficial gas velocity. The superficial velocity of the system can be defined as:

$$U_s = \frac{Q}{A}, \tag{42}$$

where Q is the volumetric flow rate and A is the cross-sectional area of the pipe. The red box in Figure 5.6 indicates the approximate range of flow conditions tested in this study within the microchannels. Initial design calculations aimed for the bubble size to fall within the Capillary number range Lu et al. (2014) tested; however, the flow conditions this model prescribes fall within the bubbly flow region on the flow regime map. It was observed that when the superficial velocities

were within this region, the injector did not function properly, producing bubbles periodically rather than at a constant rate. Further testing is needed to determine when slug flow transitions into churn flow and annular flow within microchannels.

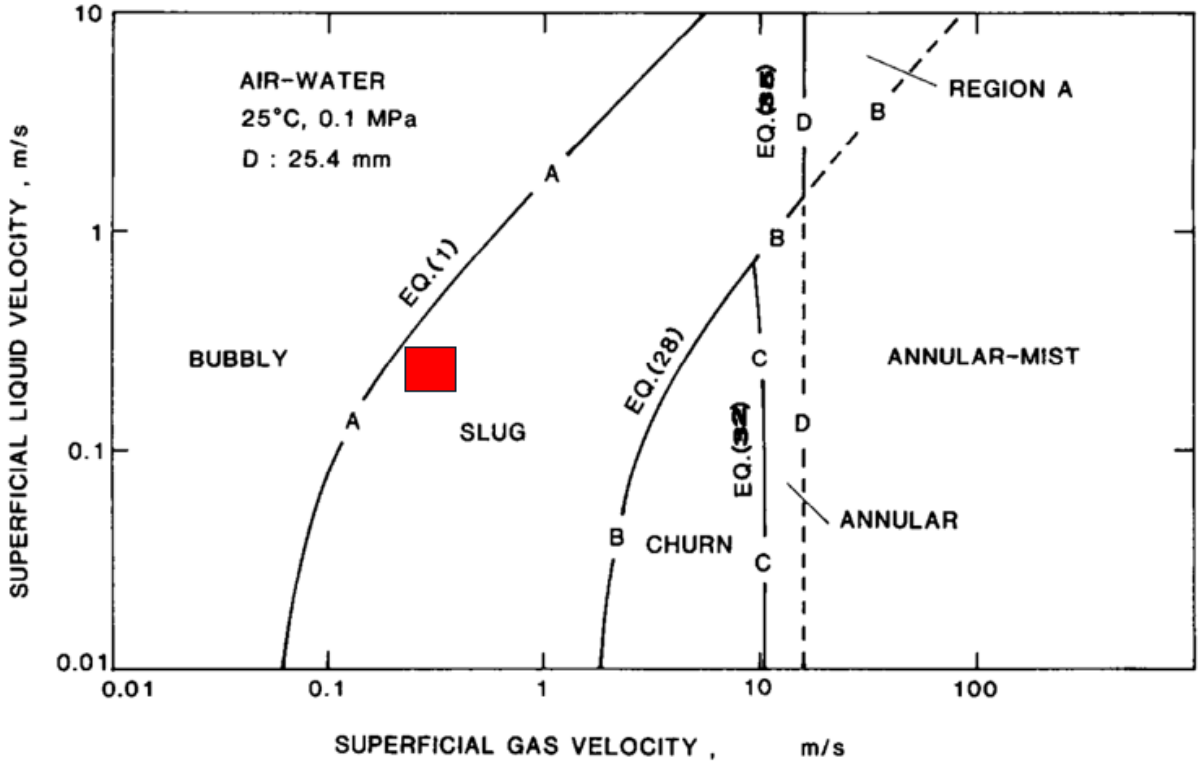

Figure 5.6: Flow regime map (Mishima and Ishii, 1984)

5.2. Injector Test Results Inside The Test Loop

The histograms resulting from the analysis outlined in Section 4.4 are shown in Figure 5.7, with the smoothed distribution shown in Figure 5.8. Identifying trends from these plots is challenging, but they are useful for highlighting anomalies in the data.

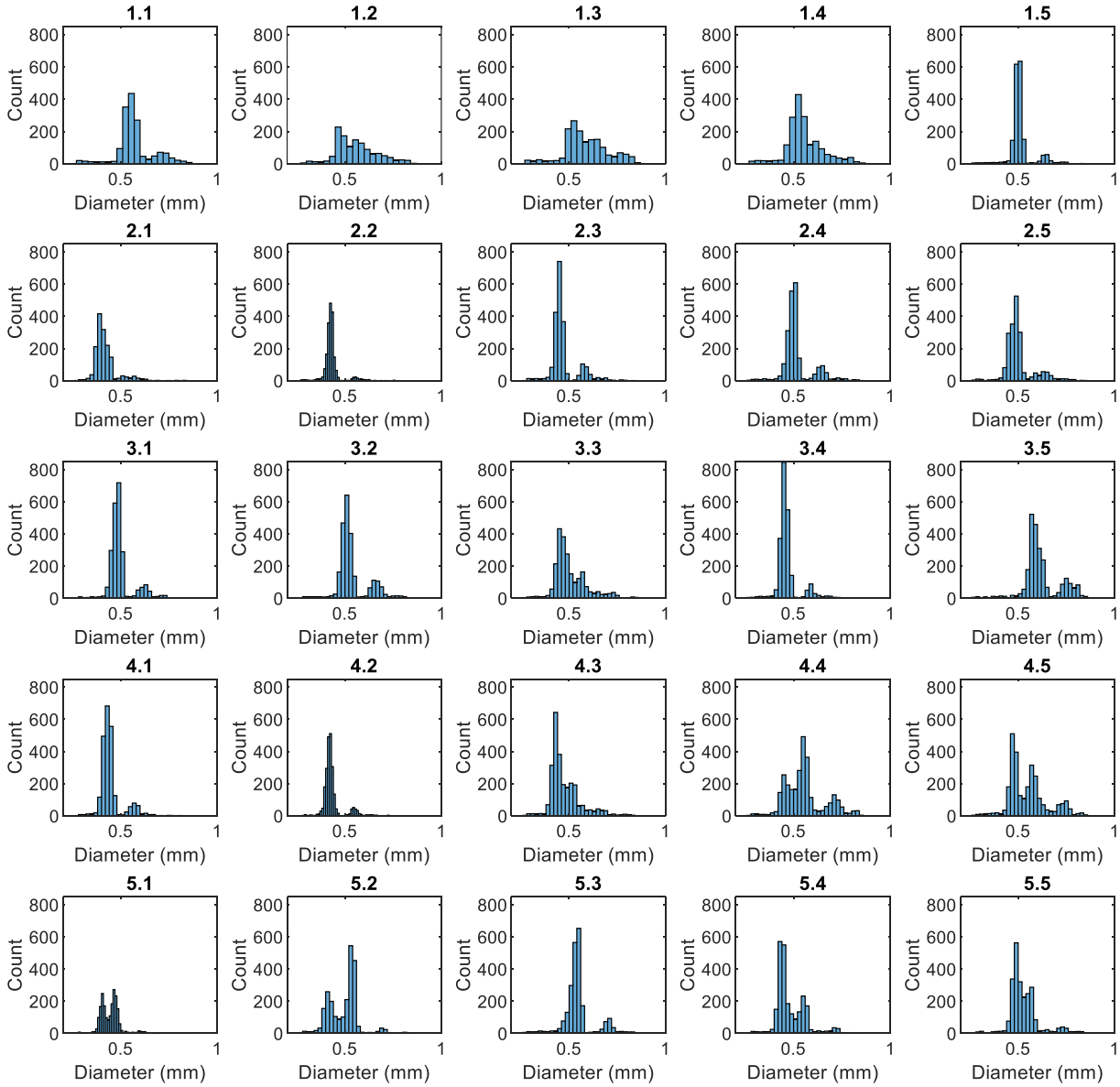

Figure 5.7: Histogram distribution of bubble diameter

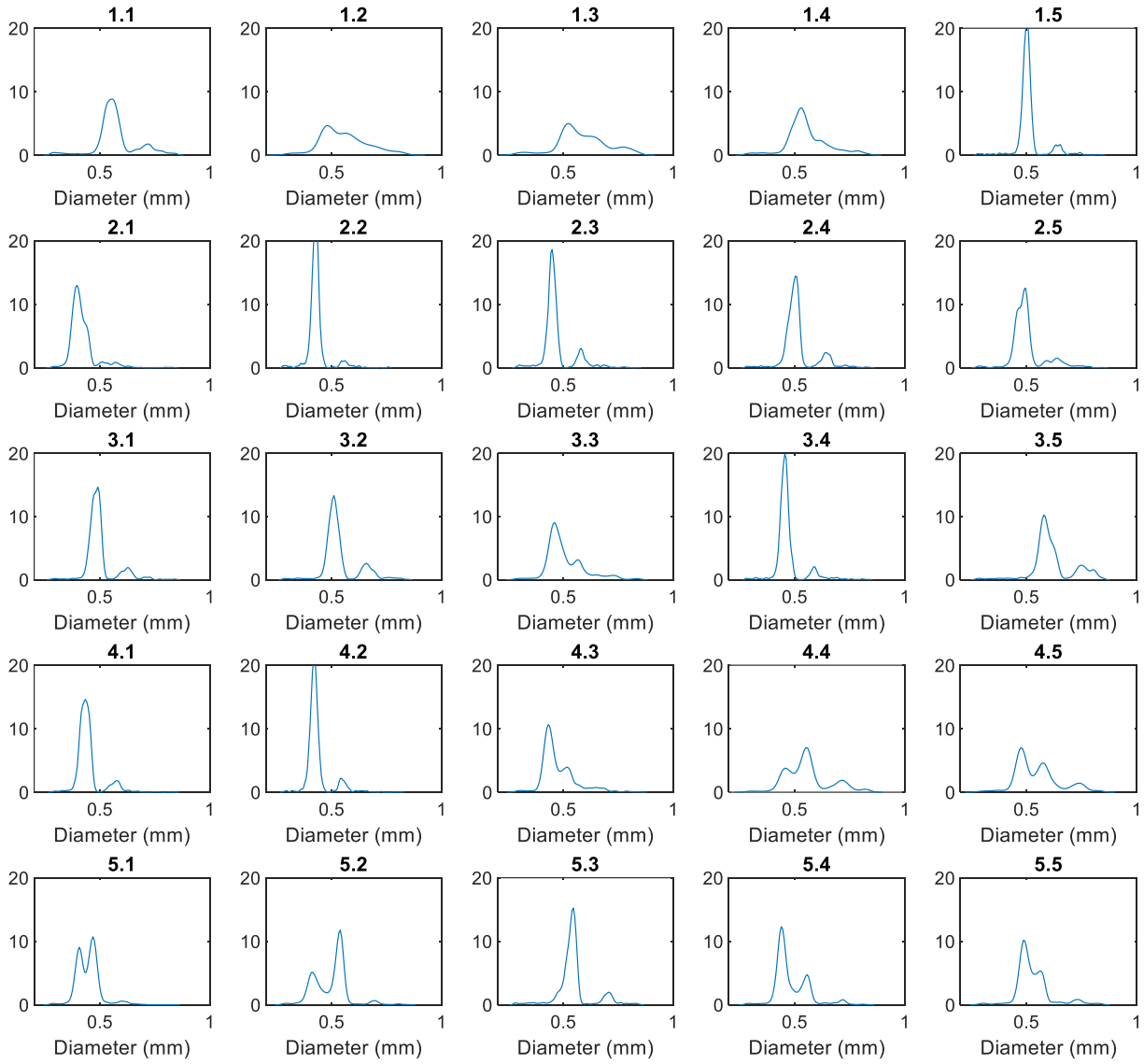

Figure 5.8: Smoothed distribution of bubble diameter.

The titles of the subplots are the names of the flow conditions in the inside of the loop tests. A summary of what these flow conditions are is summarized in Table 5.1. A way of interpreting this convention is that the first number encodes the liquid flow rate, and the second number

encodes the gas flow rate. Names of the flow conditions with greater values of the first number have greater liquid flow rates. Similarly, names of the flow conditions with greater values of the second number have greater gas flow rates

Table 5.1: Flow condition naming convention

	Qg=40.577 (ml/h)	**Qg=54.103 (ml/h)**	**Qg=67.629 (ml/h)**	**Qg=81.155 (ml/h)**	**Qg=94.680 (ml/h)**
Ql=100 (ml/h)	1.1	1.2	1.3	1.4	1.5
Ql=110 (ml/h)	2.1	2.2	2.3	2.4	2.5
Ql=120 (ml/h)	3.1	3.2	3.3	3.4	3.5
Ql=130 (ml/h)	4.1	4.2	4.3	4.4	4.5
Ql=140 (ml/h)	5.1	5.2	5.3	5.4	5.5

To better visualize potential trends, a surface plot of the results is shown in Figure 5.9. The first peak form the plots shown in Figure 5.8 was set as the equivalent diameter of each condition and used to construct the surface plot. This plot includes data points that deviate from the clear trend observed in the outside loop tests. Several factors may explain these discrepancies.

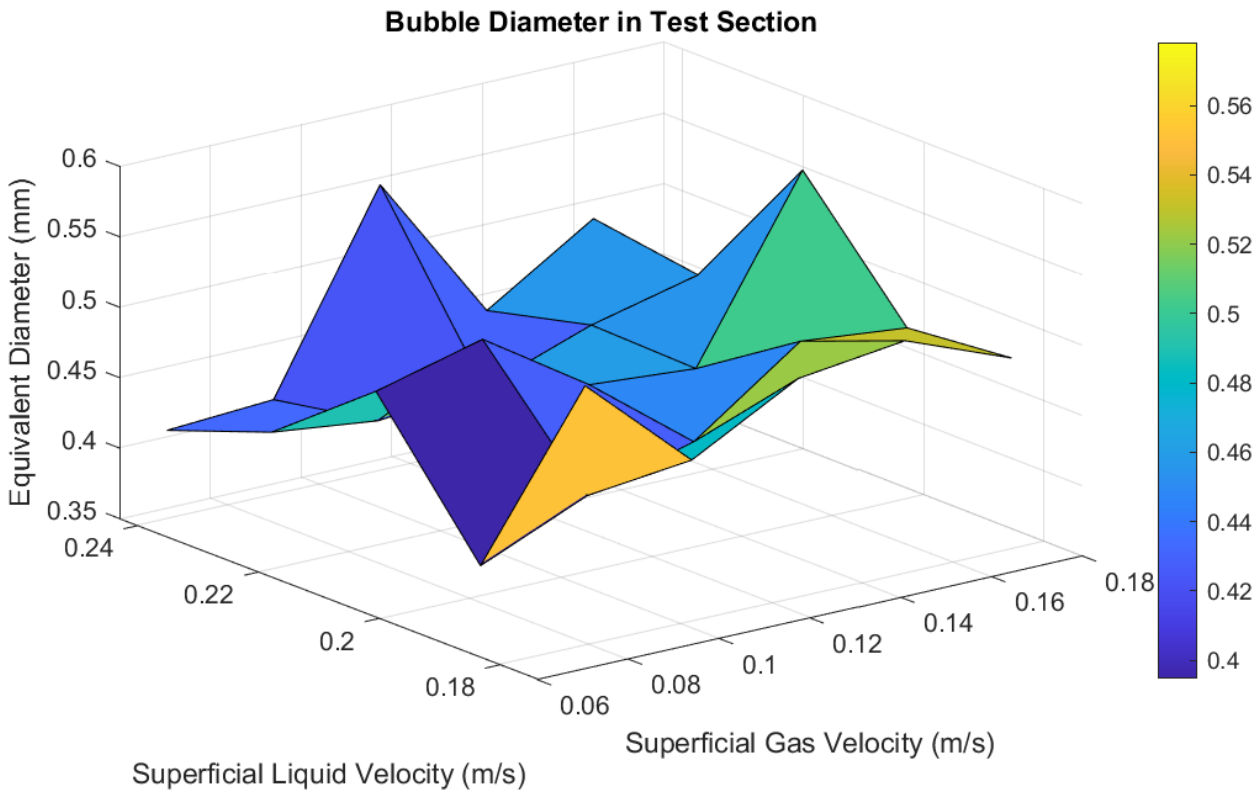

Figure 5.9: Surface plot showing the bubble diameter data from the inside loop tests

As mentioned in Section 4.1, connecting the injector to the test loop and measuring the size of the bubbles introduces many uncertainties, the first being whether the bubble observed originated from the injector. Bubbles can also coalesce, as described in Section 4.4, complicating the interpretation of the output. The outlet pressure of the injector, and thus the region of interest, is unknown, adding further uncertainty regarding the mass of the bubbles in this region. Additionally, imperfect fitting of the injector flange in its slot in the test section led to the formation of air pockets where there was a gap between the flange and test section that produced their own

bubbles.

5.3. Model Evaluation and Development

The model proposed by Lu et al. (2014) is considered in this study for the similarities in the geometries of the microchannels as well as the properties of the liquid used. Applying this model to the processed data from Section 4.2 resulted in a poor fit, as shown in Figure 5.10.

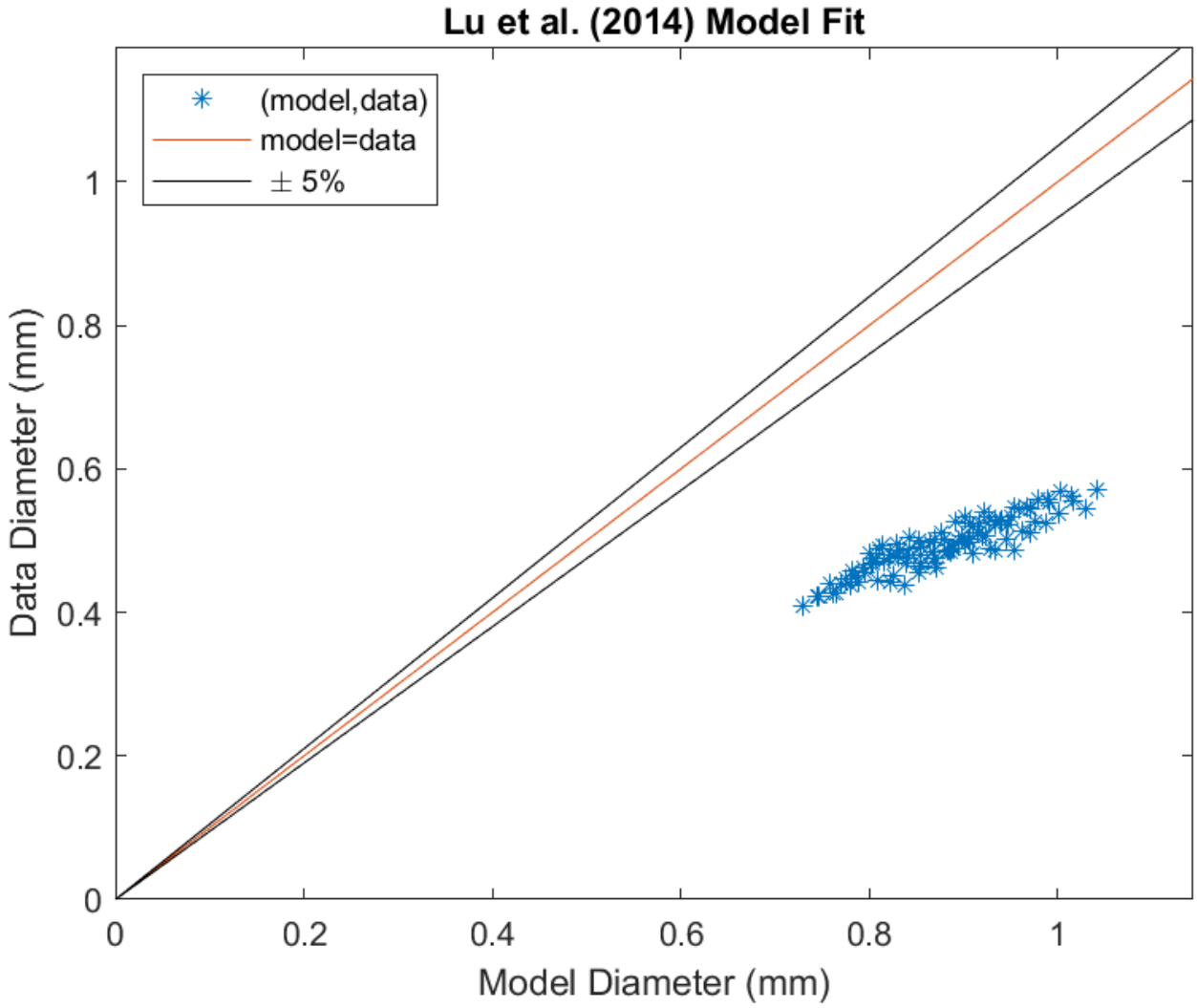

Figure 5.10: Diagonal plot comparing the predictions of Lu et al. (2014) model with experimental data.

The reason for the poor fit observed is likely a deviation of the as built channel geometry from the design channel geometry. There are a few indications from the data analysis that support this hypothesis. It was originally assumed that the channel cross section was square with a width of 0.4 mm. However, pixel counting showed the actual channel width to be 0.498 mm, significantly larger than the intended design. The mass correction factor, used to align the means of the two

mass calculation methods outlined in Section 4.2 (cylinder stacking and frequency analysis), exceeded 1 in nearly all tests, indicating that the channel is deformed, appearing wider and shallower than designed. Additionally, the pressure drop calculated using the Darcy friction factor relations in Equations (*30*) and (*31*) was, on average, underpredicted by a factor of 5 compared to the measured gauge pressure at the inlet. Finally, the average velocity of the slugs in the two-phase region was measured to be, on average, 67% faster than the combined superficial velocity of the gas and liquid.

To address this, it was assumed that the combined superficial velocity of the two-phase region:

$$U_s = \frac{Q_l + Q_g}{A} \tag{43}$$

is equivalent to the average slug velocity. The average slug velocity was calculated by tracking the centroid of the slugs as discussed in Section 4.2. This assumption allows the cross-sectional area of the channel to be determined. Using this area, the depth of the channel can be obtained by dividing the area by the channel width (0.498 mm). The newly calculated channel depth was found to be 0.192 mm. The hydraulic diameter was then derived using Equation (*9*)and used as the characteristic length of the channel.

It is important to note that this depth correction remains an unconfirmed hypothesis. It was introduced as an update to the earlier assumption of a square cross section which has significant evidence of being invalid. While this assumption will be used to develop the model, further testing is required to verify its validity and assess the applicability of the resulting model.

The newly assumed depth was applied to the Lu et al. (2014) model, and the updated fit is presented in Figure 5.11. This depth was also used in the pressure drop calculations, with the

comparison between the new predicted and measured pressure drops shown in Figure 5.12. Additionally, the mass calculation was revised using a modified cylinder stacking method. In this modification, if the diameter exceeded the depth, the cross section was modeled as an ellipse, with the major axis representing the original diameter and the minor axis representing the channel depth. This adjustment resulted in an average correction factor of 0.84. While the fits in Figure 5.11 and Figure 5.12 are not perfect, and the average correction factor is not 1, this is a major improvement and provides a much better assumed channel geometry. Many of the

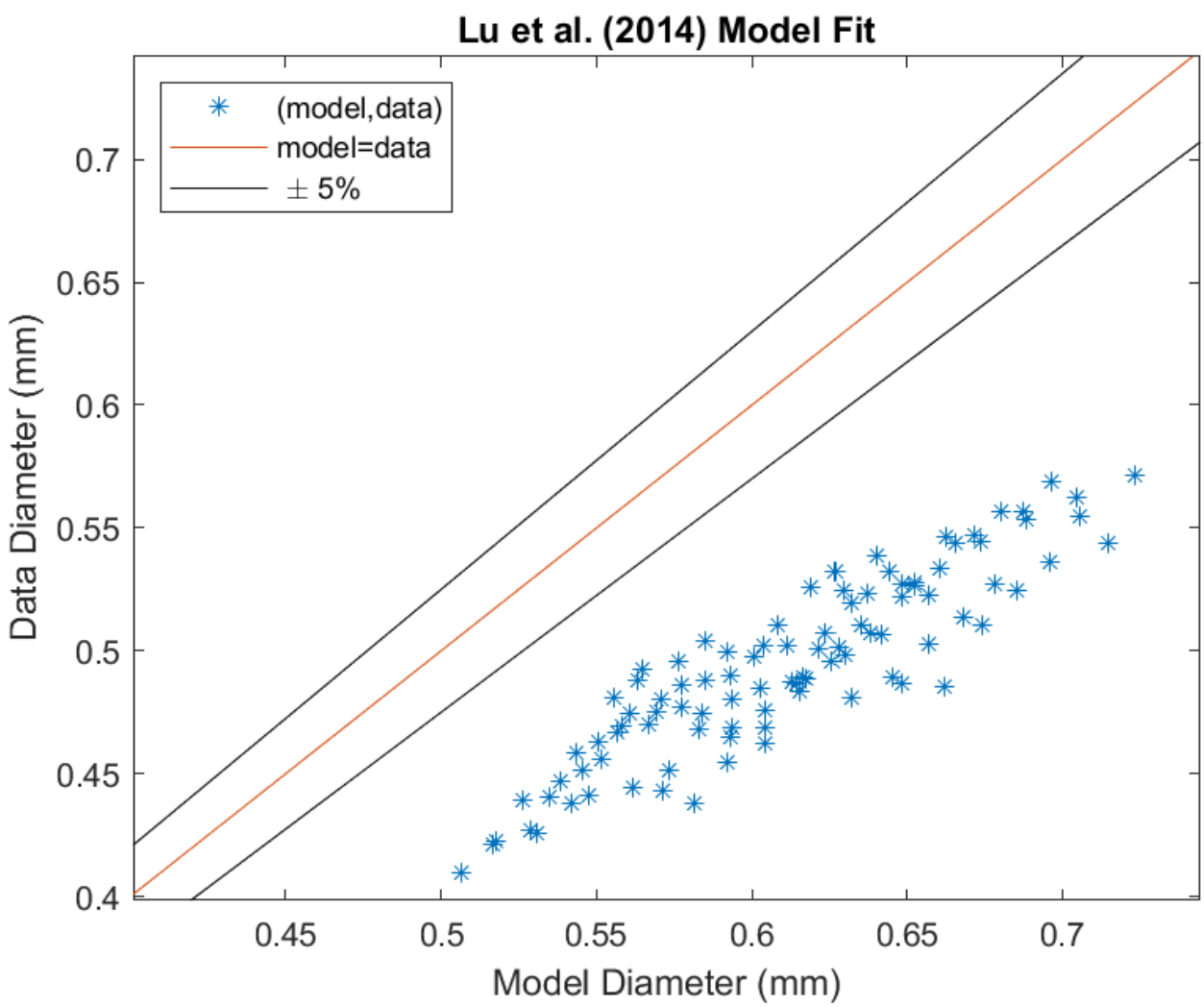

Figure 5.11: Diagonal plot showing the fit of the corrected Lu et al. (2014) model with the data

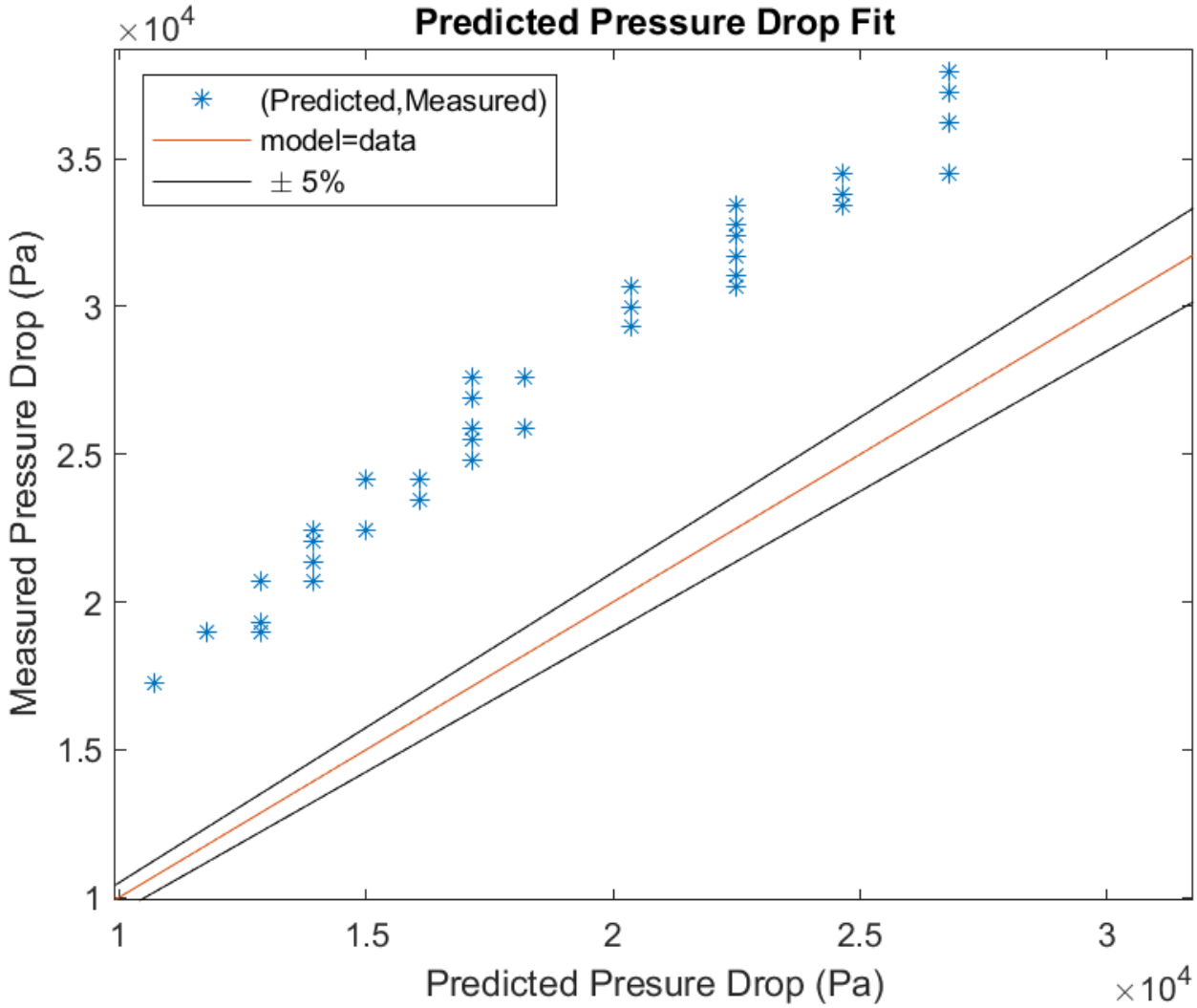

Figure 5.12: Diagonal plot showing the fit of predicted pressure drop to observed pressure drop

The lower predicted pressure drop compared to the measured pressure drop, along with the Lu et al. (2014) model's overestimation of the diameter, suggests that the depth should be reduced. However, reducing the depth would cause the mass correction factor to deviate further from 1.

The modeling approach in this study follows that of Lu et al. (2014). Their model is expressed as:

$$\frac{V_{b_m}}{w^3} = A\varphi^{\alpha} Ca^{\beta}. \tag{44}$$

To apply this model form to the rectangular geometry of the microchannels in this study, the width is substituted for hydraulic diameter:

$$\frac{V_{b_m}}{d_h^3} = A\varphi^{\alpha} Ca^{\beta}. \tag{45}$$

The exponents α and β were found by brute force testing 1000 values for each in a reasonable range resulting in 1,000,000 combinations. Each combination was evaluated by defining the model shape as:

$$V_{b_{m1}} = d_h^3 \varphi^{\alpha} Ca^{\beta}. \tag{46}$$

The scaling constant, A, was determined by:

$$A = \frac{\bar{V}_{b_{data}}}{\bar{V}_{b_{m1}}}, \tag{47}$$

where $\bar{V}_{b_{data}}$ represents the average bubble volume from the data calculated from the volumetric flow rate and the mean frequency, and $\bar{V}_{b_{m1}}$ represents the average of the shape model evaluated as the same conditions from the data. From here, the accuracy of each of the 1,000,000 models was evaluated by its root mean squared error:

$$RMSE = \sqrt{\sum_{i=1}^{n} \frac{\left(V_{b_{data\,i}} - V_{b_{m\,i}}\right)^2}{n}}, \tag{48}$$

where n represents the number of conditions tested and subscript i denotes the specific flow condition. The model with the lowest root mean squared error was then chosen as the final model.

The resulting model relationship is:

$$\frac{V_{b_m}}{d_h^3} = 11.11\varphi^{0.77}Ca^{0.24}. \tag{49}$$

This relation was used to predict the bubble volume at the point of formation, which was then converted to equivalent diameter. This model fits the data well with all the points laying within a 5% error as shown in Figure 5.13.

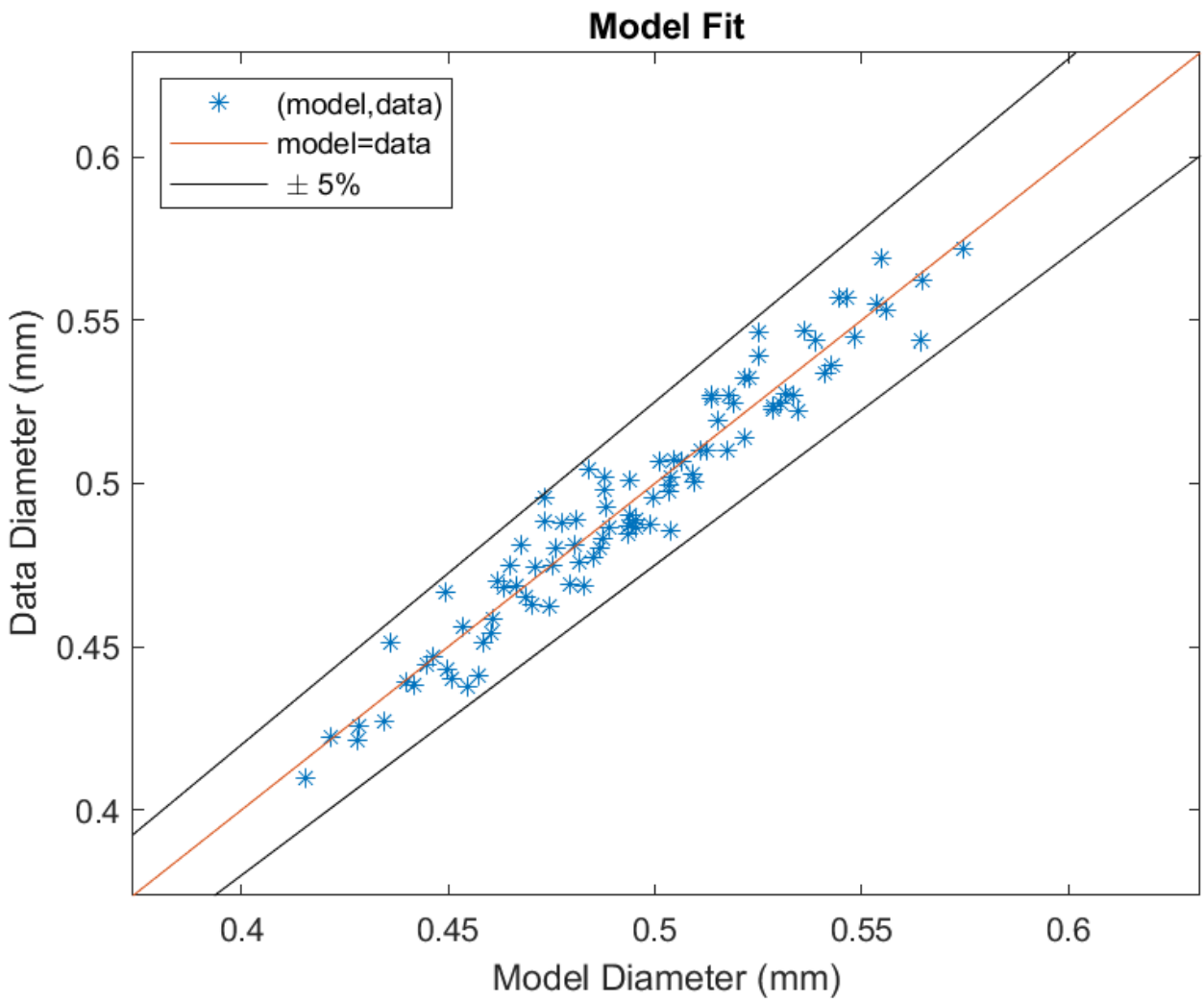

Figure 5.13: Diagonal plot showing the goodness of fit of the developed model

Further evaluation of the fit is presented by plotting the model alongside the data in Figure 5.2 and Figure 5.3. Combined plots are shown in Figure 5.14 and Figure 5.15. To visualize the model's shape, it is plotted in the surface plot in Figure 5.16.

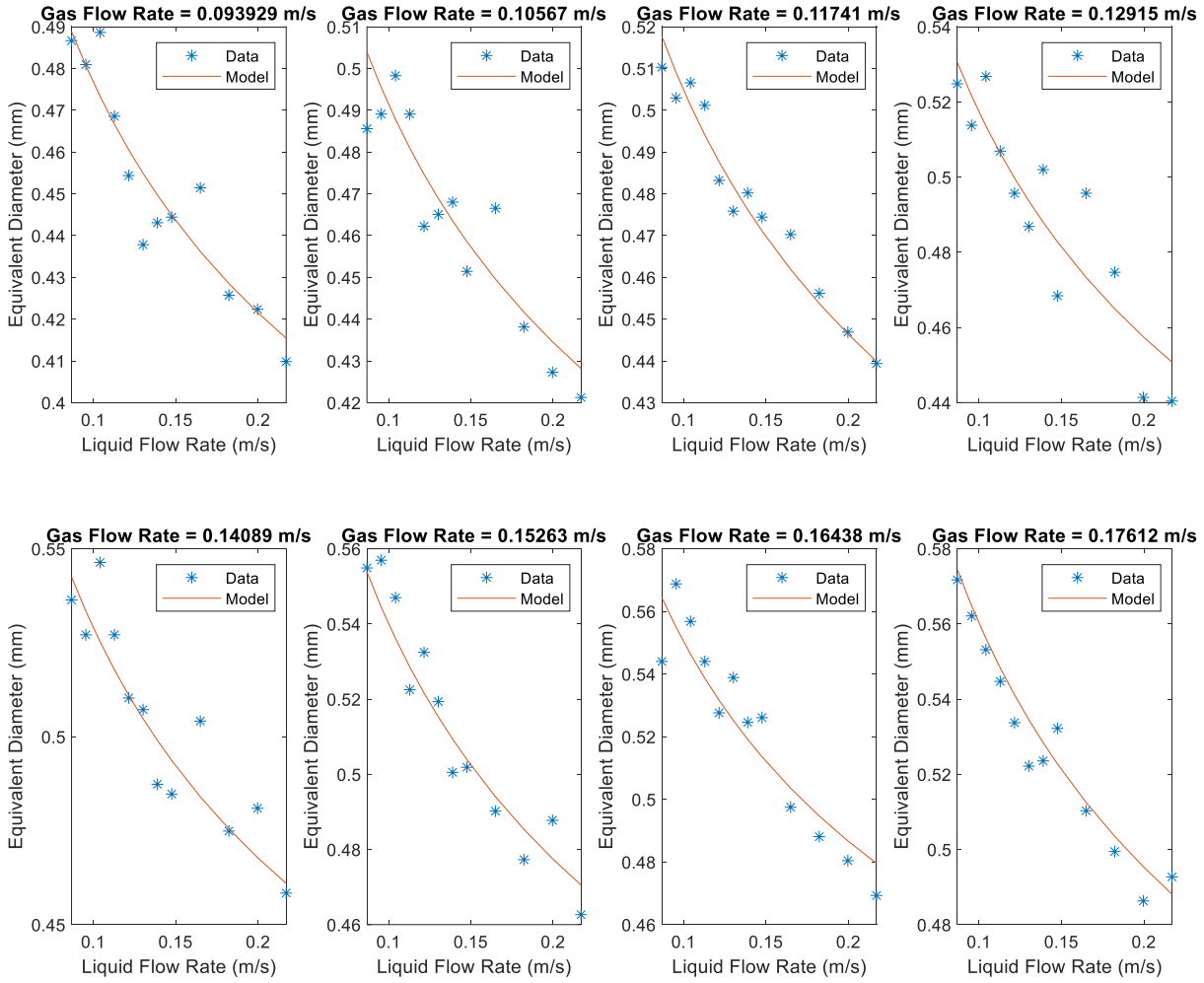

Figure 5.14: Grid plot showing the model's response accuracy to liquid flow rate fluctuations

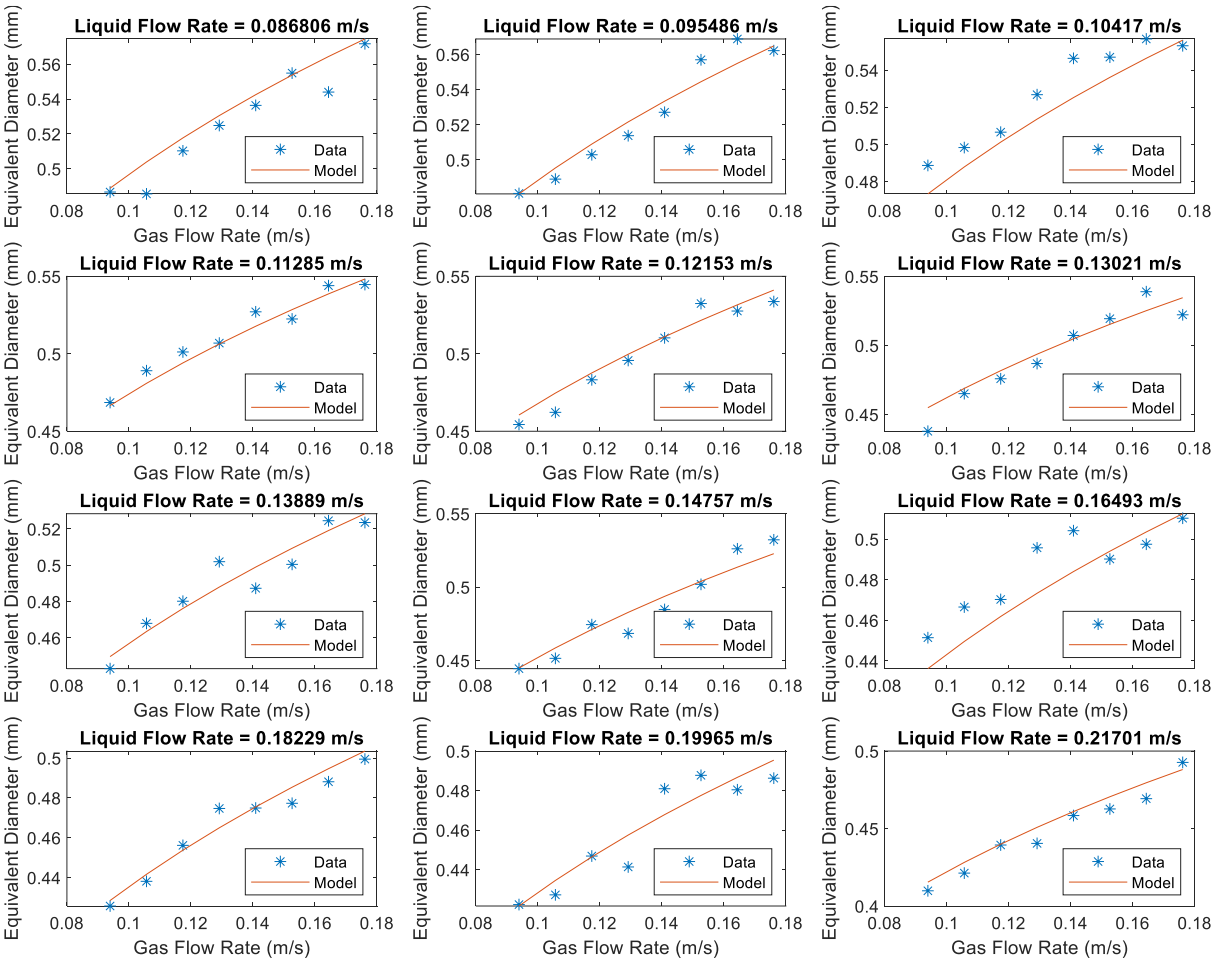

Figure 5.15: Grid plot showing the model's response accuracy to gas flow rate fluctuations

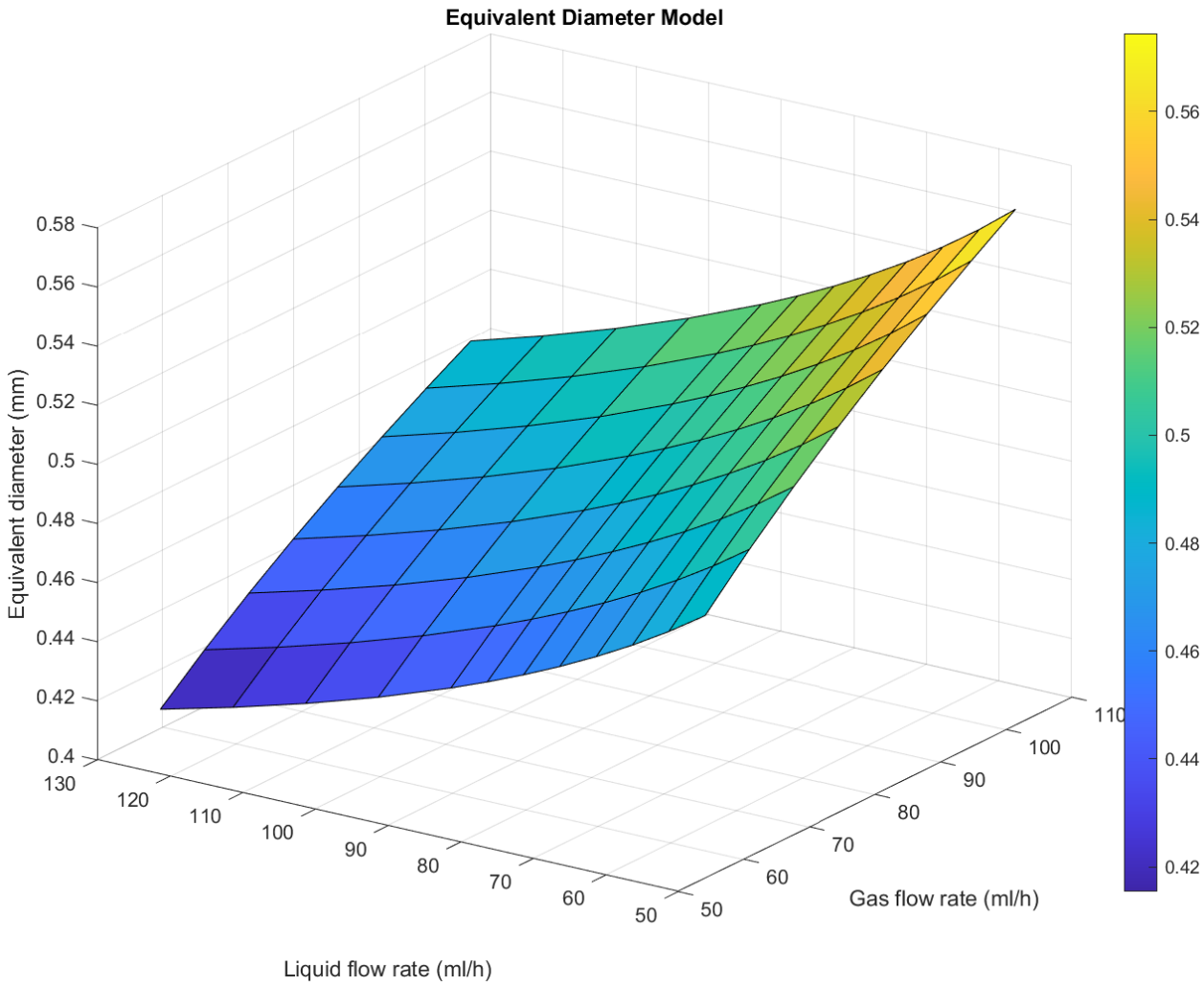

Figure 5.16: Surface plot showing the shape of the model

The model was then tested with the data from the inside test loop results to see if the relationship was consistent. The result can be seen in Figure 5.17. The model fits well in this case with 72% of the data being predicted by the model within an error margin of +/- 10%. The volume of the bubbles injected was predicted by multiplying the volume predicted by the ratio of the inlet pressure to the outlet pressure. The pressure at the outlet was assumed to be atmospheric as there

was no significant difference in the measured pressure for these cases from the outside loop tests.

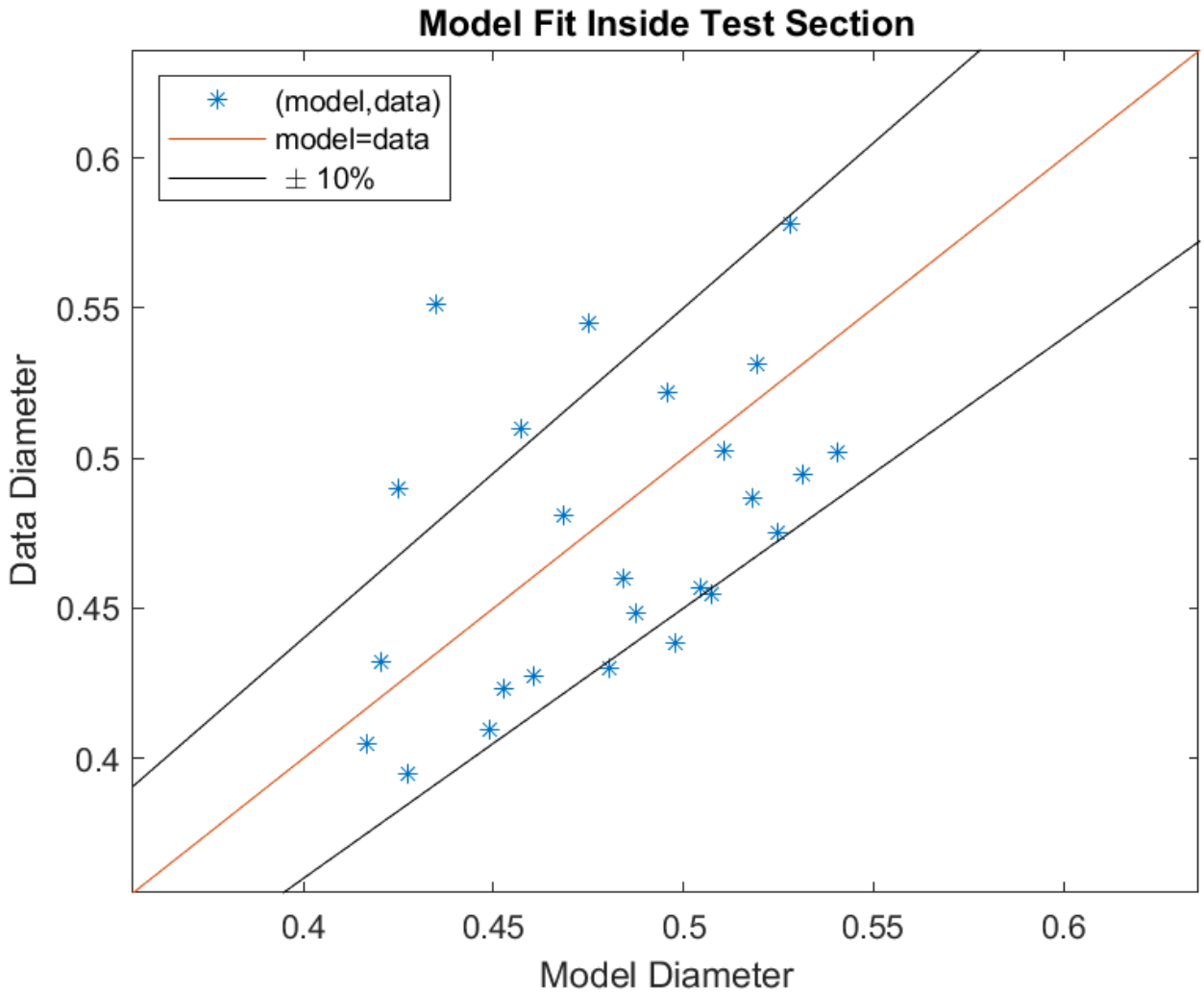

Figure 5.17: Diagonal plot showing the fit of the model with the data from the inside test loop tests

Chapter 6

6. Conclusion and Future Work

6.1. Conclusion

The injector designed and tested in this study precisely controls the size of bubbles well. The diameter of the bubbles produced in the injector had a coefficient of variation of around 6.98%. However, the bubble sizes produced were larger than the target values, preventing the injector's use for its intended research purpose. Nonetheless, this study provides a clear framework for applying microfluidics to bubble injection and presents a novel model for predicting bubble size within flow focusing microfluidic channels as a function of the volumetric flow weight ratio and capillary number.

The injector was designed for high bubble generation frequency, guided by insights from two-phase microfluidic studies in the literature. The injector used in this study consisted of a microfluidic chip, made from PDMS, sandwiched between two acrylic plates secured with fasteners. Initial testing was conducted outside the test loop, where bubble formation in the two-phase microchannels was captured through high-speed imaging. This was followed by in-loop tests, where a high-speed camera recorded bubbles produced by the injector within the test section. Data from these images were then used to develop a model predicting bubble size under various flow conditions. The model's accuracy was assessed by calculating the root mean squared error

(RMSE) between the predicted and observed data.

The process developed here can be applied to designing microfluidic bubble injectors for various systems. By matching the characteristic dimensionless numbers (Morton, Eötvös, and Reynolds numbers) of bubble dynamics from the target system to the experimental setup, a proper experimental design can be achieved if the medium properties and bubble sizes are known. A surrogate fluid and target bubble size can then be chosen, and an injector can be designed to produce bubbles of that size using the model developed in this study. The injector channel widths can be selected to ensure the model-predicted flow rates result in superficial gas and liquid velocities corresponding to slug flow on the flow regime map (Mishima and Ishii, 1984).

This study analyzes microfluidic channels beyond what has been previously reported. While other studies calculate bubble volumes based on frequency and volumetric gas flow rates, this study considers the dependence of bubble mass on inlet pressure and considers variations in bubble size by projecting 2D images into 3D using cylinder stacking. Additionally, the Fourier analysis for frequency calculation and validation is another novel approach presented. These approaches can be utilized in future studies to enhance understanding of microfluidic functionality.

6.2. Future Work

Future studies should consider several design improvements for the injector. The current injector design allows for easy modification of the microchannel geometry, which can be adjusted to produce bubbles closer to the target size of 0.355 mm. This would involve narrowing the channel width until the flow states resulting in an equivalent diameter, as predicted by the model in this

study, fall within the superficial velocity constraints for slug flow. The precision of the channel geometry is also crucial; for instance, using glass instead of acrylic for the plate that contacts the PDMS could improve adhesion, as glass adheres better to PDMS. This change could reduce the fastening pressure required to form a tight seal, potentially mitigating the channel flattening issue. Alternatively, the channels could be engraved in a more rigid material, using PDMS solely as a sealant rather than a moldable material. It is also advisable to validate that the as built geometry matches the design geometry before these dimensions are used for analysis.

Improvements to the experimental design could further reduce uncertainty. Since inlet pressure is critical to the experiment, future studies should employ a more sensitive and precise pressure gauge. Additionally, using camera lenses that provide a closer view of the test section and injector would enhance data precision. The composition of the air that was used for gas injection was not measured, so there are potential errors induced by making assumptions about the air like the gas constant, density, and interfacial tension with the surrogate fluid. This can be remedied by using bottled gas.

Once the injector is refined, a more comprehensive model for bubble size, potentially incorporating additional dependencies, can be developed. With a reliable injector, future studies could investigate bubble dynamics within the pump bowl of molten salt reactors, adjusting flow rates in the test section to simulate different pumping rates. Injection frequencies could also be varied by using different combinations of injection conditions that yield the same bubble size or by utilizing both injection channels, thereby altering the void fraction within the test section.

Once accurate models of bubble movement are established, future research can delve into the mass transfer properties of the bubbles. Such studies could design surrogate fluids that match

different dimensionless numbers relevant to mass transfer properties, like the Schmidt number and the mass transfer Biot number. Additionally, there is growing interest in applying machine learning algorithms to calculate key dimensionless numbers, such as the Nusselt and Sherwood numbers, based on bubble dynamics and the properties of the substances in the system. These algorithms could significantly enhance the optimization of fission product extraction from molten salt reactors, making them more efficient and safer providing a brighter energy future.

References

1. A. Alonso *et al.*, “Why nuclear energy is essential to reduce anthropogenic greenhouse gas emission rates,” *EPJ Nuclear Sciences & Technologies*, vol. 1, p. 3, 2015. doi:10.1051/epjn/e2015-50027-y
2. A. V. Nguyen and H. J. Schulze, *Colloidal Science of Flotation*. New York: Marcel Dekker, 2004.
3. B. Tyra *et al.*, EIA electric power monthly with data for July 2020, https://www.energy.gov/sites/prod/files/2020/11/f80/EIA-electric-power-monthly.pdf (accessed Jun. 10, 2024).
4. B. W. Brook *et al.*, “Why nuclear energy is sustainable and has to be part of the energy mix,” *Sustainable Materials and Technologies*, vol. 1–2, pp. 8–16, Sep. 2015. doi:10.1016/j.susmat.2014.11.001
5. B. Zohuri *et al.*, “Advancing Nuclear Energy: Generation-IV and small modular reactors in Nuclear Waste Management & Recycling Technology (a short review),” *Journal of Waste Management & Recycling Technology*, vol. 1, no. 3, pp. 1–4, Sep. 2023. doi:10.47363/jwmrt/2023(1)116
6. D. Liu *et al.*, “Single-cell droplet microfluidics for biomedical applications,” *The Analyst*, vol. 147, no. 11, pp. 2294–2316, 2022. doi:10.1039/d1an02321g
7. E. Compere, S. Kirslis, E. Bohlmann, F. Blankenship, and W. Grimes, *Fission product behavior in the Molten Salt Reactor Experiment*, Oct. 1975. doi:10.2172/4077644

8. H. Lund, *Renewable Energy Systems: A SMART Energy Systems Approach to the Choice and Modeling of 100% Renewable Solutions*, 2nd ed. San Diego, Waltham, MA: Academic Press : Elsevier Science & Technology Books, 2014.

9. H. Wang, S. Jiang, C. Zhu, Y. Ma, and T. Fu, "Bubble formation in T-junctions within parallelized microchannels: Effect of viscoelasticity," *Chemical Engineering Journal*, vol. 426, p. 131783, Dec. 2021. doi:10.1016/j.cej.2021.131783

10. J. Carter, *Spent nuclear fuel and reprocessing waste inventory*, Sep. 2020. doi:10.2172/1670405

11. J. Conca and J. Wright, The Cost of a Sustainable Energy Future, Apr. 2010

12. J. van Zalk and P. Behrens, "The spatial extent of renewable and non-renewable power generation: A review and meta-analysis of power densities and their application in the U.S.," *Energy Policy*, vol. 123, pp. 83–91, Dec. 2018. doi:10.1016/j.enpol.2018.08.023

13. K. Mishima and M. Ishii, "Flow regime transition criteria for upward two-phase flow in vertical tubes," *International Journal of Heat and Mass Transfer*, vol. 27, no. 5, pp. 723–737, May 1984. doi:10.1016/0017-9310(84)90142-x

14. K. Song and Y. Liu, "A compact X-ray system for two-phase flow measurement," *Measurement Science and Technology*, vol. 29, no. 2, p. 025305, Jan. 2018. doi:10.1088/1361-6501/aaa283

15. K. Takamura, H. Fischer, and N. R. Morrow, "Physical Properties of Aqueous Glycerol Solutions," *Journal of Petroleum Science and Engineering*, vol. 98–99, pp. 50–60, Nov. 2012. doi:10.1016/j.petrol.2012.09.003

16. Otsu, N., "A Threshold Selection Method from Gray-Level Histograms." *IEEE Transactions on Systems, Man, and Cybernetics*. Vol. 9, No. 1, 1979, pp. 62–66.

17. P. Garstecki, “Formation of droplets and bubbles in microfluidic systems,” *NATO Science for Peace and Security Series A: Chemistry and Biology*, pp. 163–181, 2010. doi:10.1007/978-90-481-9029-4_9

18. Petersen, H, *The properties of helium: Density, specific heats, viscosity, and thermal conductivity at pressures from 1 to 100 bar and from room temperature to about 1800 K*. Risø National Laboratory. Denmark. Forskningscenter Risoe. Risoe-R No. 224 . Sep 1970

19. R. Clift, J. R. Grace, and M. E. Weber, *Bubbles, Drops, and Particles.* Academic Press, 1978.

20. *World Energy Outlook 2006*, IEA, Paris, 2006. https://www.iea.org/reports/world-energy-outlook-2006

21. Y. Lu, T. Fu, C. Zhu, Y. Ma, and H. Z. Li, “Scaling of the bubble formation in a flow-focusing device: Role of the Liquid Viscosity,” *Chemical Engineering Science*, vol. 105, pp. 213–219, Feb. 2014. doi:10.1016/j.ces.2013.11.017

Appendix

A. Outside of The Loop Supplementary Material

The MATLAB code used to process the images for the outside of the loop tests:

```
clear
clc
close all

MatCond=readtable('MatrixCond.csv');
xy=MatCond.x_y;
P_c=MatCond.P;
Q_l=MatCond.Q_l_ml_hr_;
Q_g=MatCond.Q_g_ml_hr_;

FR=3000; %fps
T_in=20; %temperature (C)
FR=3000; %fps
T=1/FR; %time step


bitN=8;
sizeThMin=40;% remove blobs smaller than this [px]
sizeThMax=140000;% remove blobs larger than this [px]

% obtain the background image
nBackground = 100;
cropDir='E:\Data\Trial1\1.1';
cropFiles = dir(fullfile(cropDir, '*.tif')); % Assuming tif format
tempN = 0;
for iFr = 1:nBackground
    % Load two consecutive frames
    ImIn = imread(fullfile(cropDir, cropFiles(iFr).name));
    tempN = tempN +1;
    if exist('ImB')~=1 %Background image
        ImB = double(ImIn);
    else
        ImB = (ImB*(tempN-1)  + double(ImIn))/tempN;
    end
    if 1==0
        figure
        imshow(ImB)
    end

end
ImB1UC=mat2gray(ImB, [0 2^bitN-1]);

[ImB1,crop]=imcrop(ImB1UC);     %manually crop image
[roiB, ROIc]=imcrop(ImB1);

save('Background.mat', "ImB", 'ImB1')

[imgHeight, imgWidth] = size(ImB1);
```

```
maxImNo=NaN(64,5);

for trial=1:5

    for cond=1:96
        disp(['processing trial ' num2str(trial) ' of ' num2str(xy(cond))])
        imageDir=['E:\Data\Trial' num2str(trial) '\' num2str(xy(cond))];
        imageFiles = dir(fullfile(imageDir, '*.tif')); % Assuming tif format
        maxImNoM(cond,trial)=length(imageFiles);
        maxImNo=maxImNoM(cond,trial);
        if trial==1
            rmdir(['E:\Injector\Processed\',num2str(xy(cond))],'s')
        end
        mkdir(['E:\Injector\Processed\',num2str(xy(cond))])

        for iFr=1:maxImNo

            ImInRawUC = imread(fullfile(imageDir, imageFiles(iFr).name));
            ImInRaw=imcrop(ImInRawUC,crop);
            ImIn0 = mat2gray(ImInRaw, [0 2^bitN-1]);  %convert into grayscale image: intensity between 0~1
            ImIn01=1-ImIn0;

            ImIn002 = imadjust(ImIn01); %top 1% becomes 1, bottom 1% becomes 0
            ImIn02 = medfilt2(ImIn002,[6 6]);
            ImIn03 = (ImIn01-min(min(ImIn01)))/(max(max(ImIn01))-min(min(ImIn01)));
            ImIn04 = imadjust(ImIn03); %grayscale image between 0 and 1

            BWthresh1= graythresh(ImIn02);
            BWthresh2 = BWthresh1 + 0.5*(1-BWthresh1);
            tempBW = imbinarize(ImIn02,BWthresh1);

            tempA12 =xor(bwareaopen(tempBW,sizeThMin),  bwareaopen(tempBW,sizeThMax));  % retain blobs
inbetween [sizeThMin, sizeThMax]
            se = strel('disk',7);
            tempA12F = imfill(imclose(tempA12,se),'holes');

            imfile9=['E:\Injector\Processed\',num2str(xy(cond)),'\',
num2str(trial),'binary_',num2str(iFr),'.tif'];
            imwrite(tempA12F*(2^bitN-1),imfile9);
        end
    end

end
```

Table A.1:Outside of the loop condition naming convention

	Qg=54.10 (ml/h)	**Qg=60.87 (ml/h)**	**Qg=67.63 (ml/h)**	**Qg=74.39 (ml/h)**	**Qg=81.16 (ml/h)**	**Qg=87.92 (ml/h)**	**Qg=94.68 (ml/h)**	**Qg=101.44 (ml/h)**
Ql=50 (ml/h)	1.1	1.2	1.3	1.4	1.5	1.6	1.7	1.8
Ql=55 (ml/h)	2.1	2.2	2.3	2.4	2.5	2.6	2.7	2.8
Ql=60 (ml/h)	3.1	3.2	3.3	3.4	3.5	3.6	3.7	3.8
Ql=65 (ml/h)	4.1	4.2	4.3	4.4	4.5	4.6	4.7	4.8
Ql=70 (ml/h)	5.1	5.2	5.3	5.4	5.5	5.6	5.7	5.8
Ql=75 (ml/h)	6.1	6.2	6.3	6.4	6.5	6.6	6.7	6.8
Ql=80 (ml/h)	7.1	7.2	7.3	7.4	7.5	7.6	7.7	7.8
Ql=85 (ml/h)	8.1	8.2	8.3	8.4	8.5	8.6	8.7	8.8
Ql=95 (ml/h)	9.1	9.2	9.3	9.4	9.5	9.6	9.7	9.8
Ql=105 (ml/h)	10.1	10.2	10.3	10.4	10.5	10.6	10.7	10.8
Ql=115 (ml/h)	11.1	11.2	11.3	11.4	11.5	11.6	11.7	11.8
Ql=125 (ml/h)	12.1	12.2	12.3	12.4	12.5	12.6	12.7	12.8

Table A.2: Outside of the loop measured gauge pressure (psig)

	Qg=54.10 (ml/h)	**Qg=60.87 (ml/h)**	**Qg=67.63 (ml/h)**	**Qg=74.39 (ml/h)**	**Qg=81.16 (ml/h)**	**Qg=87.92 (ml/h)**	**Qg=94.68 (ml/h)**	**Qg=101.44 (ml/h)**
Ql=50 (ml/h)	2.5	2.5	2.5	2.5	2.5	2.5	2.5	2.5
Ql=55 (ml/h)	2.75	2.75	2.75	2.75	2.75	2.75	2.75	2.75
Ql=60 (ml/h)	2.75	2.8	3	3	3	3	3	3
Ql=65 (ml/h)	3	3	3	3	3.1	3.2	3.25	3.25
Ql=70 (ml/h)	3.25	3.25	3.5	3.5	3.5	3.5	3.5	3.5
Ql=75 (ml/h)	3.5	3.5	3.4	3.5	3.5	3.5	3.5	3.5
Ql=80 (ml/h)	3.6	3.6	3.6	3.7	3.7	3.75	3.9	4
Ql=85 (ml/h)	4	4	4	4	4	3.75	3.75	3.75
Ql=95 (ml/h)	4.25	4.25	4.25	4.25	4.25	4.25	4.35	4.45
Ql=105 (ml/h)	4.45	4.5	4.5	4.5	4.6	4.7	4.75	4.85
Ql=115 (ml/h)	4.85	4.85	4.9	4.9	5	4.9	5	5
Ql=125 (ml/h)	5	5	5	5.25	5.25	5.4	5.5	5.5

Table A.3: Outside of the loop measured bubble generation frequency (Hz)

	Qg=54.10 (ml/h)	**Qg=60.87 (ml/h)**	**Qg=67.63 (ml/h)**	**Qg=74.39 (ml/h)**	**Qg=81.16 (ml/h)**	**Qg=87.92 (ml/h)**	**Qg=94.68 (ml/h)**	**Qg=101.44 (ml/h)**
Ql=50 (ml/h)	249	282	270	273	279	273	312	288
Ql=55 (ml/h)	258	276	282	291	294	270	273	303
Ql=60 (ml/h)	246	261	276	270	264	285	291	318
Ql=65 (ml/h)	279	276	285	303	294	327	312	333
Ql=70 (ml/h)	306	327	318	324	324	309	342	354
Ql=75 (ml/h)	342	321	333	342	330	333	321	378
Ql=80 (ml/h)	330	315	324	312	372	372	348	375
Ql=85 (ml/h)	327	351	336	384	378	369	345	357
Ql=95 (ml/h)	312	318	345	324	336	396	408	405
Ql=105 (ml/h)	372	384	378	369	402	429	432	432
Ql=115 (ml/h)	381	414	402	459	387	402	453	468
Ql=125 (ml/h)	417	432	423	462	447	471	486	450

Table A.4: Outside of the loop measured bubble equivalent diameter (mm)

	Qg=54.10 (ml/h)	**Qg=60.87 (ml/h)**	**Qg=67.63 (ml/h)**	**Qg=74.39 (ml/h)**	**Qg=81.16 (ml/h)**	**Qg=87.92 (ml/h)**	**Qg=94.68 (ml/h)**	**Qg=101.44 (ml/h)**
Ql=50 (ml/h)	0.4867	0.4856	0.5103	0.5248	0.5364	0.5549	0.5440	0.5717
Ql=55 (ml/h)	0.4810	0.4891	0.5030	0.5138	0.5271	0.5569	0.5688	0.5621
Ql=60 (ml/h)	0.4886	0.4983	0.5066	0.5268	0.5463	0.5470	0.5568	0.5531
Ql=65 (ml/h)	0.4686	0.4891	0.5012	0.5069	0.5271	0.5225	0.5440	0.5447
Ql=70 (ml/h)	0.4544	0.4622	0.4832	0.4957	0.5103	0.5324	0.5276	0.5337
Ql=75 (ml/h)	0.4378	0.4651	0.4758	0.4869	0.5072	0.5193	0.5389	0.5222
Ql=80 (ml/h)	0.4431	0.4680	0.4802	0.5020	0.4873	0.5005	0.5246	0.5236
Ql=85 (ml/h)	0.4444	0.4514	0.4744	0.4684	0.4847	0.5019	0.5261	0.5322
Ql=95 (ml/h)	0.4514	0.4665	0.4703	0.4957	0.5041	0.4902	0.4975	0.5103
Ql=105 (ml/h)	0.4257	0.4381	0.4562	0.4747	0.4749	0.4773	0.4881	0.4994
Ql=115 (ml/h)	0.4223	0.4273	0.4469	0.4414	0.4810	0.4877	0.4804	0.4863
Ql=125 (ml/h)	0.4098	0.4212	0.4394	0.4404	0.4584	0.4626	0.4693	0.4927

Table A.5: Outside of the loop measured average slug velocity (m/s)

	Qg=54.10 (ml/h)	**Qg=60.87 (ml/h)**	**Qg=67.63 (ml/h)**	**Qg=74.39 (ml/h)**	**Qg=81.16 (ml/h)**	**Qg=87.92 (ml/h)**	**Qg=94.68 (ml/h)**	**Qg=101.44 (ml/h)**
Ql=50 (ml/h)	0.2627	0.3137	0.3012	0.3087	0.2904	0.3935	0.4484	0.4597
Ql=55 (ml/h)	0.3158	0.3631	0.3618	0.4233	0.4119	0.3962	0.4344	0.4430
Ql=60 (ml/h)	0.2844	0.3367	0.3394	0.3732	0.3857	0.4089	0.4034	0.4604
Ql=65 (ml/h)	0.3170	0.3507	0.3600	0.3799	0.4385	0.4691	0.4521	0.5574
Ql=70 (ml/h)	0.3580	0.3958	0.4222	0.4468	0.4544	0.4611	0.5060	0.4805
Ql=75 (ml/h)	0.3978	0.4028	0.4143	0.4365	0.4395	0.4826	0.5379	0.5074
Ql=80 (ml/h)	0.3991	0.4116	0.4584	0.4546	0.4985	0.5500	0.5111	0.5165
Ql=85 (ml/h)	0.4062	0.4212	0.4520	0.4958	0.4805	0.4660	0.6034	0.5824
Ql=95 (ml/h)	0.3806	0.4062	0.4109	0.4468	0.5007	0.4783	0.5899	0.5788
Ql=105 (ml/h)	0.4469	0.4890	0.4506	0.4516	0.5006	0.6216	0.5945	0.5986
Ql=115 (ml/h)	0.4797	0.5480	0.5087	0.6271	0.4949	0.5214	0.6646	0.6988
Ql=125 (ml/h)	0.5166	0.5341	0.5456	0.6202	0.5698	0.6084	0.6595	0.5656

Table A.6: Outside of the loop mass correction factor

	Qg=54.10 (ml/h)	**Qg=60.87 (ml/h)**	**Qg=67.63 (ml/h)**	**Qg=74.39 (ml/h)**	**Qg=81.16 (ml/h)**	**Qg=87.92 (ml/h)**	**Qg=94.68 (ml/h)**	**Qg=101.44 (ml/h)**
Ql=50 (ml/h)	0.9500	1.1129	1.1034	0.9440	0.9223	0.9724	1.2098	0.9644
Ql=55 (ml/h)	0.9874	1.0646	1.0411	1.1070	0.9625	0.8949	0.8338	0.9484
Ql=60 (ml/h)	0.7648	0.8478	0.7874	0.7921	0.7546	0.7691	0.7654	0.8425
Ql=65 (ml/h)	0.9002	0.8688	0.8994	0.8718	0.8694	0.9017	0.7958	0.8972
Ql=70 (ml/h)	0.9825	1.0122	0.9825	0.9508	0.9011	0.7573	0.8282	0.8028
Ql=75 (ml/h)	1.0724	0.8727	0.9722	0.8523	0.7648	0.9124	0.8242	0.8883
Ql=80 (ml/h)	0.9655	0.8847	0.8677	0.7716	0.9432	0.9274	0.7316	0.8152
Ql=85 (ml/h)	0.8771	0.8816	0.8378	0.9933	0.8556	0.8871	0.9536	0.8581
Ql=95 (ml/h)	0.6136	0.6539	0.6665	0.6382	0.6710	0.7203	0.8388	0.7655
Ql=105 (ml/h)	0.7890	0.8627	0.6106	0.5779	0.6526	0.8217	0.7265	0.6556
Ql=115 (ml/h)	0.6682	0.9201	0.6399	0.9453	0.5524	0.5595	0.7866	0.7798
Ql=125 (ml/h)	0.7331	0.7543	0.6957	0.8232	0.6108	0.6394	0.7007	0.5344

B. Inside of The Loop Supplementary Material

The MATLAB code used to process the images for the inside of the loop tests:

```
clear
clc
close all

MatCond=readtable('GlycerinWaterBWidthCond.csv');
xy=MatCond.x_y;
P_c=MatCond.P;
Q_l=MatCond.Q_l_ml_hr_;
Q_g=MatCond.Q_g_ml_hr_;

% input case specific parqmeters

FR=60; %fps
Qio=75; %volumetric flowrate of air out of syringe pump (ml/hr)
Pg=5; %pressure in psig indicated by the guage
```

```
T_in=20; %temperature (C)

% pixel calibration
if 1==0
    imageDirc='E:\GlycerinWater\Still\cal';
    imageFilesc = dir(fullfile(imageDirc, '*.tif'));
    sampleImagec = imread(fullfile(imageDirc, imageFilesc(1).name));
    [cals,calf]=imcrop(sampleImagec);
    widthf=calf(3);
    [cals,calc]=imcrop(sampleImagec);
    widthc=calc(3);
    pxtommc = 1/widthc;
    pxtommf = 1/widthf;
    pxtomm=(pxtommc+pxtommf)/2;
else
    pxtomm = .0257;
end

bitN=8;
sizeThMin=90;% remove blobs smaller than this [px]
sizeThMax=2*round(pi/4*(.6/pxtomm)^2);% remove blobs larger than this [px]
widthThMin = 0;
widthThMax = 500;
heightThMin = 0;
heightThMax = 500;
Cthresh=.98;

T=1/FR; %time step
Bguess=10;


xcmin=20; %cut-off for bubbles exiting/entering the frame
xsmin=10; %threshhold for jump to a new bubble to determine the number of bubbles that have exited the
frame


% Effective: mean intensity of the top fracPx pixels > minTh
fracPx = 0.1;
topN = 100;
minTh = 0.99; % threshold to remove ineffective streaks


% Preallocate for velocity data
imageDir1='E:\GlycerinWater\BWidth\1.1';
imageFiles1 = dir(fullfile(imageDir1, '*.tif')); % Assuming TIF format
sampleImage = imread(fullfile(imageDir1, imageFiles1(1).name));


% obtain the background image
nBackground = 100;

tempN = 0;
for iFr = 1:nBackground
    % Load two consecutive frames
    ImIn = imread(fullfile(imageDir1, imageFiles1(iFr).name));
    tempN = tempN +1;
    if exist('ImB')~=1 %Background image
        ImB = double(ImIn);
    else
        ImB = (ImB*(tempN-1)  + double(ImIn))/tempN;
    end
    if 1==0
        figure
        imshow(ImB)
    end
```

```
end
ImB1UC=mat2gray(ImB, [0 2^bitN-1]);


[ImB1,crop]=imcrop(ImB1UC);     %manually crop image

save('Background.mat', "ImB", 'ImB1')

[imgHeight, imgWidth] = size(ImB1);

MaxCond=25;
maxImNo=500;

for cond=1:MaxCond
    imageDir=['E:\GlycerinWater\BWidth\' num2str(xy(cond))];
    imageFiles = dir(fullfile(imageDir, '*.tif')); % Assuming TIF format

    rmdir(['E:\GlycerinWater\BWidth\FBWidth\',num2str(xy(cond))],'s')
    mkdir(['E:\GlycerinWater\BWidth\FBWidth\',num2str(xy(cond))])

    for iFr= 1:maxImNo
        disp(['processing frame ',num2str(iFr), ' out of ',num2str(maxImNo) ' in condition '
num2str(xy(cond))])
        ImInRawUC = imread(fullfile(imageDir, imageFiles(iFr).name));
        ImInRaw=imcrop(ImInRawUC,crop);
        ImIn0 = mat2gray(ImInRaw, [0 2^bitN-1]);  %convert into grayscale image: intensity between 0~1
        ImIn01=ImB1 -ImIn0;

        ImIn002 = imadjust(ImIn01,[.2 .8]); %top 1% becomes 1, bottom 1% becomes 0
        ImIn02 = medfilt2(ImIn002,[6 6]);

        BWthresh1= graythresh(ImIn02);
        tempBW = imbinarize(ImIn02,BWthresh1);


        tempA12F=imfill(tempA12F1,'holes');


            imfile9=['E:\GlycerinWater\BWidth\FBWidth\',num2str(xy(cond)),'\binary_',num2str(iFr),'.tif'];
            imwrite(tempA12F*(2^bitN-1),imfile9);
    end

end
```

Table B.1: Inside of the loop condition naming convention

	Qg=40.58 (ml/h)	**Qg=54.10 (ml/h)**	**Qg=67.63 (ml/h)**	**Qg=81.16 (ml/h)**	**Qg=94.68 (ml/h)**
Ql=100 (ml/h)	1.1	1.2	1.3	1.4	1.5
Ql=110 (ml/h)	2.1	2.2	2.3	2.4	2.5
Ql=120 (ml/h)	3.1	3.2	3.3	3.4	3.5
Ql=130 (ml/h)	4.1	4.2	4.3	4.4	4.5
Ql=140 (ml/h)	5.1	5.2	5.3	5.4	5.5

Table B.2: Inside of the loop measured gauge pressure (psig)

	Qg=40.58 (ml/h)	**Qg=54.10 (ml/h)**	**Qg=67.63 (ml/h)**	**Qg=81.16 (ml/h)**	**Qg=94.68 (ml/h)**
Ql=100 (ml/h)	4	4	4	4	4
Ql=110 (ml/h)	4	4	4	4	4
Ql=120 (ml/h)	4.5	4.5	4.5	4.5	4.5
Ql=130 (ml/h)	4.75	4.75	4.85	5	5
Ql=140 (ml/h)	5	5	5	5	5

Table B.3: Inside of the loop measured equivalent diameter (mm)

	Qg=40.58 (ml/h)	**Qg=54.10 (ml/h)**	**Qg=67.63 (ml/h)**	**Qg=81.16 (ml/h)**	**Qg=94.68 (ml/h)**
Ql=100 (ml/h)	0.5511	0.4811	0.5219	0.5315	0.5020
Ql=110 (ml/h)	0.3947	0.4272	0.4483	0.5025	0.4948
Ql=120 (ml/h)	0.4899	0.5096	0.4602	0.4544	0.5782
Ql=130 (ml/h)	0.4322	0.4232	0.4298	0.4567	0.4751
Ql=140 (ml/h)	0.4049	0.4095	0.5449	0.4384	0.4865